

2016

NDT and SHM Methods of Damage Detection in Welded Structures

Saad Mohammed
University of South Carolina

Follow this and additional works at: <https://scholarcommons.sc.edu/etd>

 Part of the [Mechanical Engineering Commons](#)

Recommended Citation

Mohammed, S.(2016). *NDT and SHM Methods of Damage Detection in Welded Structures*. (Master's thesis). Retrieved from <https://scholarcommons.sc.edu/etd/3945>

This Open Access Thesis is brought to you by Scholar Commons. It has been accepted for inclusion in Theses and Dissertations by an authorized administrator of Scholar Commons. For more information, please contact dillarda@mailbox.sc.edu.

NDT AND SHM METHODS OF DAMAGE DETECTION IN WELDED STRUCTURES

By

Saad Mohammed

Bachelor of Science
University of Al-Qadisiya, 2010

Submitted in Partial Fulfillment of the Requirements

For the Degree of Master of Science in

Mechanical Engineering

College of Engineering and Computing

University of South Carolina

2016

Accepted by:

Victor Giurgiutiu, Director of Thesis

Lingyu Yu, Reader

Cheryl L. Addy, Vice Provost and Dean of the Graduate School

© COPYRIGHT BY SAAD MOHAMMAD, 2016

ALL RIGHTS RESERVED.

DEDICATION

To my daughters:

ELIAN & ALLMA

ACKNOWLEDGMENTS

First foremost, I would like to thank all researchers who enriched the field of NDT and SHM. Also, my sincere thanks and appreciation go to my teachers from elementary school to the professors in my current stage of my life for their encouragement, inspiration, motivation and valuable efforts to build my life

I would like to express my gratitude to all persons who helped me realize this work.

I'm especially grateful to my supervisor, Professor Victor Giurgiutiu, for his mentorship, support and inspiration without which this work would not have been possible. It has been such a rewarding experience and tremendous honor to be his student. Also, great thanks and appreciation to Dr. Yu for her help and permission to do SLDV experiment into her laboratory and for her time and efforts to read my thesis.

I wish to sincerely thank Dr. Bin Lin, Asaad Migot, Hanfei Mei, Xiaoyi Sun, and William Roth for their valuable assistance given during the compilation of this thesis and big thank goes to all people at the Laboratory for Active Materials and Smart Structures (LAMSS) for sharing their works, ideas, organized academic style and efforts. Many thanks also go to my sponsor HCED-Iraq for financial support.

Finally, I would like to thank my understanding and supportive family for their love and encouragement.

ABSTRACT

There has been an increasing demand for Nondestructive Testing (NDT) and Structural Health Monitoring (SHM) techniques to continuously monitor during all processes of a structure to prevent catastrophic failure and reduce maintenance costs. NDT and SHM are inspection processes which form part of the quality assurance/quality control (QA/QC) scheme. Among NDT and SHM methods, ultrasonic and guided wave techniques are the most commonly and widely used in industry. Ultrasonic methods provide the advantage of accurately locating and dimensioning defects within structures. Most of these structures consist of welded joints because welding is an economical and efficient method for obtaining a permanent joint. However, austenitic stainless steels, especially the welding process zone, exhibit heterogeneous and anisotropic behavior which has a decisive influence on the ultrasonic beam making the interpretation of ultrasonic inspection results notoriously difficult. NDT and SHM methods aim to detect possible defects and characterize them (location and dimensions) so that their severity can be assessed, and the mechanical integrity of the welded components guaranteed.

Experimental investigations confirm the challenges and significant shortcomings in the inspection of future industrial components where such microstructures are desirable for their mechanical properties.

First, the methods of fabricating artificial weld defects are investigated. Because of the great variety of possible types of cracks and causes for their formation, the problem

of safeguarding against crack formation in welding operations is a highly complex one. The experimental set-up is fabricated to meet these challenges.

Austenitic stainless steel welds are inspected with X-ray radiography (RT) and advanced ultrasonic NDT such as phased array ultrasonic testing (PAUT).

Second, guided wave propagation in elastic structures is discussed. High frequency guided waves within thick structures and along weld geometries are discussed. Furthermore, the interaction of weld guided waves with defects is examined through Pitch-Catch and Scanning Laser Doppler Vibrometer (SLDV) methods.

The thesis finishes with a comparison between NDT and SHM followed by a summary, conclusions, and suggestions for future work.

TABLE OF CONTENTS

DEDICATION	iii
ACKNOWLEDGEMENTS	iv
ABSTRACT	v
LIST OF FIGURES	x
CHAPTER 1 Introduction.....	1
1.1 Motivation	1
1.2 Thesis Aim and Objectives	3
1.3 Thesis Organization.....	3
CHAPTER 2 Literature Review	5
2.1 Austenitic Stainless Steel	5
2.2 Fabrication of Welded Joints with Realistic Defects	8
2.3 Non-Destructive Testing of Welds.....	12
2.4 Structural Health Monitoring of Welds and Damage Detection	14
2.5 Connection to the Topic of this MS Research.....	17
CHAPTER 3 Austenitic Stainless Steel: Microstructure and Welding Characteristic	18
3.1 Introduction	18
3.2 Metallurgy and Microstructure Characteristics of Austenitic Stainless Steel.....	19

3.3	Welding Characteristics of Austenitic Stainless Steels	24
CHAPTER 4 NDT of Welded Structures: Ultrasonic Testing		31
4.1	Introduction	31
4.2	Ultrasonic Testing (UT)	32
4.3	Ultrasonic Beam Characteristics	34
4.4	Fundamental Properties of Sound Waves	37
4.5	Wave Scattering	43
CHAPTER 5 Fundamentals of Guided Waves and SHM with PWAS		45
5.1	Brief Review of Guided Waves Theory	45
5.2	Rayleigh Waves.....	47
5.3	Shear Horizontal Plate Waves.....	49
5.4	Lamb Waves.....	52
5.5	Straight Crested Lamb Waves.....	54
5.6	Circular Crested Lamb Waves	58
5.7	Structural Health Monitoring Using Guided Waves	61
5.8	Piezoelectric Wafer Active Sensors	65
5.9	Damage Detection Using Guided Waves.....	69
CHAPTER 6 Welded Joints with Realistic Defects		71
6.1	State-of-The-Art.....	73
6.2	Representativeness of Flaws	73

6.3	Methods of Fabrication of Realistic Welding Defects	74
6.4	Nondestructive Evaluation of Welding	76
6.5	Experiment Set-Up #1	79
6.6	Results and Discussion of Set-Up #1	83
6.7	Experiment Set-Up #2.....	86
6.8	Results and Discussion of Set-Up #2.....	89
CHAPTER 7 Damage Detection in Austenitic Stainless Steel Welded Plate		97
7.1	State-of-The-Art.....	98
7.2	Experiments with Pitch-Catch Method	101
7.3	Experiments with Scanning Laser Doppler Vibrometer	131
CHAPTER 8 NDT and SHM Comparison		141
8.1	The Difference between Structural Health Monitoring.....	141
CHAPTER 9 Conclusion and Future Works		145
9.1	Summary	145
9.2	Conclusion.....	145
9.3	Recommendation for Future Work	146
References.....		148

LIST OF FIGURES

FIGURE 1.1 BP OIL REFINERY IN TEXAS CITY, TX. MARCH 23RD, 2005 EXPLOSION & FIRE.	2
FIGURE 1.2 BP OIL DISASTER, APRIL 20, 2010, IN THE GULF OF MEXICO.	2
FIGURE 3.1 THE FE-CR BINARY PHASE DIAGRAM (AWS, 2011).....	20
FIGURE 3.2 MICROSTRUCTURE OF AUSTENITIC STAINLESS STEEL PLATE TYPE 304	21
FIGURE 3.3 3HIGHLY MAGNIFIED CRYSTALLINE STRUCTURE OF AUSTENITIC STAINLESS STEEL.	21
FIGURE 3.4 FACE-CENTERED CUBIC(FCC) UNIT CELL.....	22
FIGURE 3.5 SOLIDIFICATION OF A METAL. ADAPTED FROM (WWW.MTARR.CO.UK)	25
FIGURE 3.6 TYPICAL WELD MICROSTRUCTURE, SHOWING BOTH WELD PASS BOUNDARIES (BLACK LINES) AND GRAIN BOUNDARIES (ALTERNATING GREY AND WHITE BANDS). ORIGINAL IMAGE TAKEN FROM (MOYSAN ET AL., 2003).....	26
FIGURE 3.7 COLUMNAR GRAINS STRUCTURE OF AUSTENITIC WELD MATERIALS: (A) STANDARD PIPE TO PIPE WELD, (B) NARROW GAP WELD, (C) DISSIMILAR WELD (PUDOVIKOV ET AL., 2008)	26
FIGURE 3.8 VARIOUS FERRITE MORPHOLOGIES (AWS, 2011).....	27
FIGURE 3.9 DELONG DIAGRAM FOR ESTIMATING THE MICROSTRUCTURE OF STAINLESS STEEL WELD METAL (AWS, 2011)	28
FIGURE 3.10 MULTI-PASSES JOINT	29
FIGURE 3.11 SAMPLE FROM HAZ OF WELDED SS PLATE. KUMAR ET AL., (2006)	30
FIGURE 3.12 LAYOUT OF MST SAMPLE. KUMAR ET AL., (2006)	30
FIGURE 4.1 ULTRASOUND RANGE DIAGRAM(WIKIMEDIA.ORG)	32

FIGURE 4.2 COMMON FREQUENCY RANGES FOR VARIOUS ULTRASONIC PROCESSES (CHEEKE, 2002)	33
FIGURE 4.3 THE SOUND FIELD OF A TRANSDUCER. (OLYMPUS, 2010)	36
FIGURE 4.4 DECAY OF A PROPAGATING PULSE (LEMPRIERE, 2002).....	38
FIGURE 4.5 ATTENUATION OF A WAVE DUE TO GRAIN SCATTERING(LESTER 1998).....	38
FIGURE 4.6 SOUND WAVE REFRACTION AND MODE CONVERSION. (OLYMPUS, 2010).....	40
FIGURE 4.7 RELATIVE AMPLITUDE OF WAVE MODES	41
FIGURE 4.8 NDT-UT VARIABLES RELATIONSHIP. (ASNT, 2010)	43
FIGURE 4.9 A CROSS-SECTION THROUGH COLUMNAR GRAINS SHOWING(HUDGELL, 1994)	44
FIGURE 5.1 DIFFERENT WAVEGUIDES (KUNDU, 2004).	46
FIGURE 5.2: SCHEMATIC REPRESENTATION OF MOTIONS IN A RAYLEIGH SURFACE WAVE (LEMPRIERE, 2002).....	48
FIGURE 5.3: COORDINATE DEFINITION AND PARTICLE MOTION OF SH PLATE WAVES (GIURGIUTIU 2014).....	50
FIGURE 5.4: (A) SH PLATE WAVE-SPEED DISPERSION CURVES; (B) SYMMETRIC MODE SHAPES; (C) ANTISYMMETRIC MODE SHAPES (GIURGIUTIU 2014).....	51
FIGURE 5.5 SYMMETRICAL AND ASYMMETRICAL LAMB WAVES: MODE 1.	53
FIGURE 5.6 LAMB WAVES MODE 2 AND 3.	53
FIGURE 5.7: PARTICLE MOTION OF LAMB WAVE MODES: (A) SYMMETRIC MODE AND (B) ANTISYMMETRIC MODE (GIURGIUTIU, 2014).....	54
FIGURE 5.8 (A) WAVE SPEED DISPERSION CURVE; (B) WAVENUMBER DISPERSION CURVE..	56
FIGURE 5.9: MODE SHAPES OF S0 AND A0 LAMB WAVES IN A 2-MM THICK ALUMINUM PLATE (SHEN, 2014).....	58

FIGURE 5.10 (A) CYLINDRICAL COORDINATE FOR PROBLEM DERIVATION (GIURGIUTIU 2014);	59
FIGURE 5.11 HANKEL FUNCTION OF ORDER ZERO ($H_0^{(1)}(R)$) AND ORDER ONE ($H_1^{(1)}(R)$) (SHEN, 2014).	61
FIGURE 5.12 PITCH-CATCH ACTIVE SENSING: (A) BASELINE RESPONSE; (B) RESPONSE WITH DAMAGE; (C) SCATTERED RESPONSE. (IHN AND CHANG 2008).....	63
FIGURE 5.13 (A) PHASED ARRAY IMAGING USING EUSR (GIURGIUTIU AND BAO 2004); (B) SPARSE ARRAY IMAGING USING TIME-REVERSAL METHOD (WANG ET AL. 2004).....	64
FIGURE 5.14 (A) ELECTRO-MECHANICAL COUPLING BETWEEN THE PZT ACTIVE SENSOR AND THE STRUCTURE (GIURGIUTIU ET AL. 1999); (B) EMIS SPECTRUM (ZAGRAI AND GIURGIUTIU 2001).	65
FIGURE 5.15 COMPARISON BETWEEN CONVENTIONAL ULTRASONIC TRANSDUCER AND PWAS.	65
FIGURE 5.16 SCHEMATIC OF PWAS APPLICATION MODES (GIURGIUTIU 2010).....	67
FIGURE 5.17 LAMB WAVE GENERATION USING PWAS (GIURGIUTIU 2014).	68
FIGURE 5.18 (A) STRAIN LAMB WAVE TUNING RESULTS FROM ANALYTICAL SOLUTION; (B) EXPERIMENTAL RESULTS FROM PWAS RESPONSE (GIURGIUTIU 2003).	69
FIGURE 5.19 THE EFFECTS OF TWO TYPES OF DEFECT (LEMPROERE, 2002).....	70
FIGURE 6.1 REAL CRACK.....	72
FIGURE 6.2 NDT CALIBRATION BLOCKS. OLYMPUS-IMS.COM.....	72
FIGURE 6.3 REALISTIC DEFECTS KIT.....	72
FIGURE 6.4 FLOW CHART OF WELDING NDE.....	77
FIGURE 6.5 FLOW CHART OF REALISTIC WELDING DEFECTS	78

FIGURE 6.6 WELD TERMINOLOGY	78
FIGURE 6.7 SET-UP OF 0.50" THICK AUSTENITIC SS 304 PLATE.....	80
FIGURE 6.8 SPECIMEN #1 CONFIGURATION	80
FIGURE 6.9 COPPER PLATE IS USED TO GET LACK OF ROOT PENETRATION.....	81
FIGURE 6.10 BACK SIDE OF THE PLATE WHICH SHOWS LACK OF ROOT PENETRATION.....	81
FIGURE 6.11 WELDING POROSITIES	82
FIGURE 6.12 TUNGSTEN INCLUSION	83
FIGURE 6.13 SET-UP OF RADIOGRAPHIC TESTING METHOD (RT)	84
FIGURE 6.14 IMAGE QUALITY INDICATORS. ADOPTED FORM THE WELDING INSTITUTE (TWI)	85
FIGURE 6.15 RT OF 0.50" THICK AUSTENITIC SS 304 PLATE	85
FIGURE 6.16 WELD BEVEL DETAIL	86
FIGURE 6.17 SET-UP OF 0.25" THICK AUSTENITIC SS 304 PLATE.....	86
FIGURE 6.18 WELDING CRACKS. ADOPTED FROM WIKIMEDIA.ORG.....	88
FIGURE 6.19 NDT-RT-X-RAY SOURCE DETAILS	89
FIGURE 6.20 RT SET-UP FOR SPECIMEN#2.....	90
FIGURE 6.21 RT OF SS 304 PLATE #2 WITH CLOSE-UP VIEW OF TWO CRACKS	91
FIGURE 6.22 .OLYMPUS-OMNISCAN SX. ADOPTED FROM (OLYMPUS-IMS.COM).....	92
FIGURE 6.23 STANDARD PA PROBE. ADOPTED FROM (OLYMPUS-IMS.COM).....	92
FIGURE 6.24 STANDARD WEDGE FOR ANGLE PA PROBE. ADOPTED FROM (OLYMPUS- IMS.COM)	93
FIGURE 6.25 FLAW#1 (TRANSVERSE CRACK)-OLYMPUS PAUT.....	95
FIGURE 6.26 FLAW 2 (LONGITUDINAL CRACK)-OLYMPUS PAUT	95

FIGURE 7.1 PITCH-CATCH EXPERIMENT TO DETECT THE NOTCH (SHEN, 2014).....	99
FIGURE 7.2 COMPARISON BETWEEN WFR SIMULATIONS AND EXPERIMENTS FOR LAMB WAVES' INTERACTION WITH A NOTCH IN PITCH-CATCH METHOD (SHEN, 2014).....	99
FIGURE 7.3 THE INSTALLATION KIT FOR STRAIN GAGES (GIURGIUTIU, 2014)	100
FIGURE 7.4 INSTALLATION PROCEDURE FOR PIEZOELECTRIC ACTIVE SENSORS (GIURGIUTIU, 2014).....	101
FIGURE 7.5 A PITCH-CATCH CONFIGURATION BETWEEN A T-PWAS AND A R-PWAS (GIURGIUTIU, 2014).....	102
FIGURE 7.6 SETUP FOR PITCH-CATCH LAMB WAVE INTERACTION WITH DAMAGE.	103
FIGURE 7.7 HANNING WINDOW MODULATED TONE BURST 3-COUNT AND ITS FREQUENCY DOMAIN AT 90 KHZ.....	104
FIGURE 7.8 WAVEFORM AND WAVELET TRANSFORM OF 3-COUNTS TONE BURST EXCITED SIGNAL AT 135 KHZ ARE GENERATED BY AGU-VALLEN WAVELET SOFTWARE.....	104
FIGURE 7.9 (A) PLOTTING TUNING CURVE EXPERIMENTALLY, (B) PLOTTING TUNING CURVE THEORETICALLY(GIURGIUTIU, 2014).....	106
FIGURE 7.10 TUNING CURVE OF 1MM ALUMINUM PLATE (YU ET AL., 2010)	106
FIGURE 7.11 MAIN GUI OF WAVEFORMREVEALER (SHEN, 2014).....	107
FIGURE 7.12 SCHEMATIC OF THE PRISTINE PLATE AND PWAS CONFIGURATION.....	108
FIGURE 7.13 TUNING CURVE OF A PRISTINE PLATE (EXPERIMENTAL).....	109
FIGURE 7.14 TUNING CURVE OF A PRISTINE PLATE (THEORETICAL)	109
FIGURE 7.15 SUPERIMPOSED BETWEEN WT OF SIGNALS WITH ITS SLOWNESS CURVE AT FREQUENCY EXCITATION (A) 135 KHZ (B) 300 KHZ (C) 450 KHZ (D) 750 KHZ	112

FIGURE 7.16 GROUP VELOCITY DISPERSION CURVE IN PLATES: (A) SYMMETRIC LAMB WAVES; (B) ANTISYMMETRIC LAMB WAVES (GIURGIUTIU, 2014)	113
FIGURE 7.17 EXPERIMENTAL A GROUP VELOCITY DISPERSION CURVE (YU ET AL., 2010)	114
FIGURE 7.18 DISPERSION CURVE (THEORETICAL)	115
FIGURE 7.19 DISPERSION CURVE (EXPERIMENTAL).....	116
FIGURE 7.20 SYMMETRIC MOTION	117
FIGURE 7.21 MODES SHAPE OF S ₀ ACROSS 1 MM THICKNESS OF ALUMINUM PLATE CHANGES WITH FREQUENCIES (GIURGIUTIU 2014)	118
FIGURE 7.22 ANTISYMMETRIC MOTION.....	118
FIGURE 7.23 MODES SHAPE OF A ₀ ACROSS 1 MM THICKNESS ALUMINUM PLATE AT DIFFERENT FREQUENCIES (GIURGIUTIU, 2014).....	119
FIGURE 7.24 MODE SHAPES FOR 19-MM THICK STEEL AT FREQUENCY 450 KHZ (A) SYMMETRIC (B) ANTISYMMETRIC (KAMAS, 2014)	119
FIGURE 7.25 MODES SHAPE ACROSS THE 6.35 MM THICKNESS OF STEEL-304 PLATE FOR VARIOUS LAMB MODES AT VARIOUS FREQUENCIES	121
FIGURE 7.26 COMPARISON BETWEEN WFR AND EXPERIMENT FOR LAMB WAVE MODES PROPAGATION IN A PRISTINE 6.35-MM AUSTENITIC STAINLESS STEEL-304 PLATE	123
FIGURE 7.27 SCHEMATIC OF THE PRISTINE WELDED AREAS AND PWAS CONFIGURATION	124
FIGURE 7.28 PRISTINE SIGNAL BEFORE MODIFICATION	124
FIGURE 7.29 PRISTINE SIGNAL AFTER MODIFICATION	125
FIGURE 7.30 SIGNALS COMPARISON OF PRISTINE WELDED AREAS AT DIFFERENT FREQUENCIES	126
FIGURE 7.31 SCHEMATIC OF THE WELDED PLATE AND PWASs CONFIGURATION.....	127

FIGURE 7.32 A COMPARISON BETWEEN PRISTINE SIGNAL AND DAMAGED SIGNAL (TRANSVERS CRACK SIGNAL) AT 90 KHz, 135 KHz, AND 180 KHz, 240, 300, AND 360 EXCITED SIGNALS	128
FIGURE 7.33 A COMPARISON BETWEEN PRISTINE SIGNAL AND DAMAGED SIGNAL (LONGITUDINAL CRACK SIGNAL) AT 90 KHz, 135 KHz, AND 180 KHz, 240, 300, AND 360 EXCITED SIGNALS	129
FIGURE 7.34 WAVELET TRANSFORMS OF PRISTINE WELD, TRANSVERSE CRACK AND LONGITUDINAL CRACK SIGNALS AT EXCITATION FREQUENCY OF 180 KHz	131
FIGURE 7.35 SLDV EXPERIMENT SET-UP FOR WAVE PROPAGATION VISUALIZATION	132
FIGURE 7.36 SLDV POINTS POSITION	133
FIGURE 7.37 COMPRESSION BETWEEN SIGNALS OF LINE (2-7) AND (4-5) AT DIFFERENT POINTS	133
FIGURE 7.38 COMPRESSION BETWEEN SIGNALS OF LINE (2-7) AND (1-8) AT DIFFERENT POINTS	134
FIGURE 7.39 COMPRESSION BETWEEN SIGNALS OF LINE (2-7) AND (3-6) AT DIFFERENT POINTS	135
FIGURE 7.40 SIGNAL OF LINE 1-8 AT DIFFERENT POINTS	138
FIGURE 7.41 NORMALIZED DISPLACEMENT AMPLITUDE MEASURED AT DIFFERENT LOCATIONS ALONG LINE 2-7 AND LINE3-6 AND COMPARISON WITH THE THEORETICAL BEAM-SPREADING WAVE FROM A POINT SOURCE ON THE PLATE.....	139
FIGURE 7.42 NORMALIZED DISPLACEMENT AMPLITUDE MEASURED AT DIFFERENT LOCATIONS ALONG LINE 2-7 AND LINE1-8 AND COMPARISON WITH THE THEORETICAL BEAM-SPREADING WAVE FROM A POINT SOURCE ON THE PLATE.....	140
FIGURE 8.1 PAUT PROBE AND WEDGE(OLYMPUS-IMS.COM) LAST VISIT 10/18/2016.....	141
FIGURE 8.2 PWAS.....	142

FIGURE 8.3 NDT-RT FOR A PLANE. ADOPTED FROM NDT HANDBOOK, 3RD ED.: v 4, RT. 143

CHAPTER 1

INTRODUCTION

This chapter serves as the introduction to the entire thesis by addressing the motivation and importance of conducting the research, discussing research goal, and objectives will be discussed, and introducing the organization of the thesis.

1.1 MOTIVATION

The present work was motivated by related developments in petroleum and nuclear industries. Austenitic stainless steels are an important group of materials which are used extensively in such fields where resistance to corrosion, or high strength and creep resistance at elevated temperatures, are required. The use of such steels in welded structures can result in smaller critical defect sizes. NDT and SHM methods which forms part of the whole quality assurance/quality control (QA/QC) scheme are required for such welded structures to reduce maintenance cost and prevent catastrophic failure as shown in figures Figure 1.1 and Figure 1.2 for instance. Welded austenitic components can be difficult, or even impossible, to examine ultrasonically. Development of ultrasonic techniques is therefore in progress to provide improvements which are being sought on safety and economic grounds.



Figure 1.1 BP oil refinery in Texas city, TX. March 23rd, 2005 explosion & fire.
Photo, Brett Coomer/ Houston Chronicle



Figure 1.2 BP oil disaster, April 20, 2010, in the Gulf of Mexico.
Photo/Dave Martin/ Boston.com

1.2 THESIS AIM AND OBJECTIVES

The aim of this thesis is investigating the behavior of the propagation of ultrasonic waves through austenitic stainless steel weld. Also, to demonstrate the methods of fabrication realistic weld defects and detect these defects by NDT and SHM technologies. The objectives of the work presented in this thesis are as follows: To develop a new method of inspection austenitic stainless steel welds.

1. To demonstrate a method of fabrication realistic weld defects which are important to assess the performance and reliability of used NDT and SHM methods and their procedure.
2. To study the ultrasonic behavior in austenitic stainless steel
3. To investigate the Lamb wave propagation in austenitic stainless steel
4. To apply ultrasonic NDT techniques to detect a welding defect in welded austenitic stainless steel.
5. To apply SHM methods to detect a welding defect in welded austenitic stainless steel
6. To compare the UT NDT and SHM methods and results

1.3 THESIS ORGANIZATION

To achieve the objectives set forth in the preceding section, the thesis is organized in 9 chapters. The introduction and contents of each chapter are introduced in Chapter 1.

In Chapter 2, literature is reviewed with respect to austenitic stainless steel, the fabrication of welded joints with intentional defects that are needed to assess the performance, procedures, development, and reliability of used NDT and SHM methods.

Then, the literature of NDT and SHM methods to detect welded structures is introduced. Finally, SHM methods and techniques of damage detection are discussed. This chapter concludes by summarizing the current state of the art of NDT and SHM technologies and by identifying future research areas necessary to advance these fields.

In Chapter 3, microstructure, metallurgy and welding characteristics of austenitic stainless steel are introduced.

In Chapter 4, the importance of NDT-UT method, principles and problem of austenitic stainless steel are reviewed.

In Chapter 5, fundamentals of weld guided waves, SHM methods and techniques of damage detection are introduced.

In Chapter 6, after the state of the art reviewed with respect to the fabrication of intended welding defects, the most common welding processes and welding discontinuities are introduced. In addition, two sets of experiments are conducted and the NDT results are discussed.

In Chapter 7, in general, crack detection in thick welded plate by using SHM methods is discussed with different sets of experiments. In particular, the weld guided Lamb wave in austenitic stainless steel welded plate is introduced and accordingly the experimental results are presented.

In Chapter 8, introduce a comparison between NDT and SHM methods.

In Chapter 9, concluding remarks are presented along with the suggested future work.

CHAPTER 2

LITERATURE REVIEW

This chapter first review the literature of austenitic stainless steel, the fabrication of welded joints with intentional defects that are needed to assess the performance, procedures, development, and reliability of used NDT and SHM methods. Then, the literature of NDT and SHM methods to detect welded structures is introduced. Finally, SHM methods and techniques of damage detection are discussed

2.1 AUSTENITIC STAINLESS STEEL

Lai et al. (2012) briefly covered the history of stainless steels and classify them according to their microstructures. They discuss each of the classifications: ferritic, austenitic, martensitic, duplex, precipitation-hardening and high nitrogen stainless steels. The various problems that occur with particular classes of stainless steels such as embrittlement, sensitization intergranular corrosion are outlined. They state that stainless steel has excellent corrosion-resistant, does not discolor in a normal atmospheric environment, outperforms ordinary steels on high-temperature mechanical properties and it is much better in terms of fire resistance, retention of strength and stiffness at elevated temperatures compared with carbon steels. Three main types of microstructures exist in stainless steels, *i.e.*, ferrite, austenite and martensitic. These microstructures may be obtained by adjusting steel chemistry. Out of these three main microstructures, stainless

steels may be categorized into several main classes. The different classes of stainless steels possess different properties for variety applications.

Khatak and Raj (2002) produced a comprehensive review on the physical, mechanical and welding metallurgy of austenitic stainless steels along with discussions on their physical properties. They find that corrosion behavior of austenitic stainless steels is sensitive to the various metallurgical parameters such as cold work, sensitization and high temperature phase transformation besides environmental factors. The roles of these variables on localized corrosion such as pitting corrosion, crevice corrosion, intergranular corrosion and stress corrosion cracking in aqueous environments are detailed. Also, the various methods for online detection and monitoring of corrosion using non-destructive testing techniques, such as eddy current, ultrasonic, radiography, acoustic emission, thermography etc., that will be of use to the practicing engineers are reviewed.

Holmberg (2008) discussed the importance of stainless steel microstructure for its corrosion resistance, physical, and mechanical properties of the steels and provides information on their weldability, informs briefly on different filler metal forms, and provides practical advice for the welding of stainless steels. He states that the steels of type 304, 316, 304L and 316L have very good weldability and are very unsusceptible to hot cracking because they solidify with high ferrite content.

Cobb (1999) evolved a manual that covered the scientific and technical information of major steel products to meet the requirements of purchasers' specifications and standards. The author divided the stainless steel into five groups based upon crystalline structure:

1. Martensitic (4XX)
2. Ferritic (4XX)
3. Austenitic (2XX, 3XX)
4. Duplex (austenite and ferrite)
5. Precipitation hardened

Also, each one of these five groups are classified into types and series based on their chemical compositions, mechanical properties, manufacturing process, typical application, and standards. For instance, austenitic stainless steel is classified into two types, 200-series and 300-series. Austenitic stainless steels containing chromium, nickel and manganese are given a 200-series classification and austenitic stainless steels containing chromium and nickel are given a 300-series classification.

Folkhard et al. (1988) provided information on the metallurgical problems that may be encountered during stainless steel welding, since mechanical and corrosion resistance properties of stainless steel are greatly influenced by the metallurgical processes that occur during welding or during heat treatment of welded components. They aim to help overcome a certain degree of insecurity that is often encountered in welding shops engaged in the welding of stainless steels and is often the cause of welding problems which may, in some instances, lead to the premature failure of the welded

component. The authors focused in particular on the significance of constitution diagrams, on the processes occurring during the solidification of weld metal, and on the recrystallization and precipitation phenomena which take place in the area of the welds. Also, the hot cracking resistance during welding and the practical welding of a number of different stainless steel grades were covered. In addition, recommendations were given as to the most suitable procedures to be followed in order to obtain maximum corrosion resistance and mechanical properties from the weldments.

Yan et al. (2010) investigated the microstructure and mechanical properties of 304 stainless steel that welded by tungsten inert gas (TIG) welding, laser welding and laser-TIG hybrid welding. The X-ray diffraction and tensile tests showed that the joint by laser welding had the highest tensile strength and smallest dendrite size, while the joint by TIG welding had the lowest tensile strength and biggest dendrite size.

2.2 FABRICATION OF WELDED JOINTS WITH REALISTIC DEFECTS

Crutzen et al. (1996) stated that the use of very artificial discontinuities (e.g., side drilled holes, SDH or flat bottom holes, FBH) in materials to demonstrate that the capability of NDT methods often conduct to optimistic statements and hazardous use of the method (even if for trails only) on structures containing real defects. Crutzen et al. listed a comparison of responses between real and artificial defects and concluded that the NDT procedure has to be validated and tested for its reliability on structures containing defects that, not being necessarily real ones, induce the physical phenomena that the inspection techniques must be able to handle.

International Atomic Energy Agency (2001) reported that test specimens of NDT are a very important part of the training and certification of NDT personnel. There are specifications for the test specimens of every NDT method qualification, such as joint design, material, and minimum dimensions of the test specimen, location and types of the required flaws. The biggest challenge in the fabrication of NDT specimens is the manufacturing of a flaw, and this guidebook provided the procedure of manufacturing all welding flaws. In addition to this procedure, a welder with excellent experience is required because these flaws are obtained by weld modification.

Virkkunen et al. (2009) stated that an ENIQ working report, The European Network for Inspection and Qualification (ENIQ) is a utility driven network dealing with the reliability and effectiveness of non-destructive testing (NDT) for nuclear power plants (NPP), was proposed four methods to obtain weld flaws:

- 1 Implanted defects: where a pre-existing defect is attached to the test piece. The attachment usually takes the form of a weld in a machined recess.
- 2 Weld doping or weld modification: where for instance crack prone material is added to a weld to promote localized weld cracking. Other examples include introduction of porosity or slag.
- 3 Machined defects: where a defect can consist of a cut or machined void. Electro Discharge Machining (EDM) is perhaps the most relied upon technology in this area where a shaped electrode is used to erode the test piece. The process is most

suitable for production of surface defects, although it is possible to use it in combination with welding to produce buried defects.

- 4 Grown defects: where cracking is initiated and propagated into test pieces in much the same way as would occur in a plant, simply accelerated to make fabrication times practical. The main processes used for this class of defect are thermal fatigue and stress corrosion cracking.

That ENIQ document was never published in the form referred to in their paper.

Virkkunen et al. developed the forth method, grown defects, by using a thermal fatigue cracking mechanism which is called True flaw technology. Cyclic thermal fatigue loading is induced locally by alternating heating and water spray cooling. This way is restricted to simple component shapes and small components because crack growth requires stress to provide a driving force and for thicker material or complex geometry becomes hard to provide the required stress.

Consonni et al. (2012) quoted the four methods to obtain weld flaws from (Virkkunen et al., 2009) and state that the most of controlled defects produced by TWI (The Welding Institute) are obtained by weld modification, machining or by growing defects. Consonni et al. provide some examples of the techniques used to obtain the intentional weld defects and their application, for the different defect types.

Srivastava (2013) produced a specimen test suitable for, liquid penetrant test, magnetic particle testing, and radiographic testing during welding and heat treatment processes. For welding process, the concept of cooling rate of the welding materials, base

metal and the filler material, is considered; so, the bending load is applied at the required location to initiate a grown crack. While for heat treatment process austenitizing, quenching and tempering, processes are followed to create a crack for the tool steels.

Ngon and Toan (2015) produced longitudinal welding crack with residual stress using cast iron electrodes. This crack can be detected by radiographic testing and the phased array ultrasonic testing technique. The proposed technology is required a SMAW welding method for the front side and GTAW method for the back side of the specimen. Thus, it is suitable for skilled welders, who qualified according to AWS D1.1 and able to create welding defects for NDT training.

Moysan et al. (2003) presented a model for predicting the grain orientation in austenitic stainless steel welds to understand the propagation of ultrasound in anisotropic multi-pass welds to improve their ultrasonic testing. The micrographic observations of obtaining the resulting grain orientation are to develop a solidification model and to develop a model to predict the resulting grain orientations without using a complete solidification model. The model, which is called MINA, based on both micrographic observations supplemented by Electron Back Scattered Diffraction (EBSD), X-ray analyses, knowledge of crystalline growth mechanisms and information contained in the welding report or notebook. This model supplies realistic information on the anisotropy that is found in a multi-pass weld for ultrasonic wave propagation

Tseng and Hsu (2011) used a thin layer of an activated flux, MnO₂, TiO₂, MoO₃, SiO₂, and Al₂O₃, were packed in powdered form on the surface of the joint in TIG welding process to produce an activated TIG welding. The experiment results show that activated TIG welding achieves an increase in the joint penetration and weld depth-to-width ratio, significantly reducing the angular distortion of the weldment. Also, delta-ferrite content in weld metal is increased which increase the hardness of stainless steel welds.

2.3 NON-DESTRUCTIVE TESTING OF WELDS

The non-destructive testing of austenitic stainless steel welds is a significant problem for the nuclear industry. Ultrasonic techniques would be very helpful to detect, locate and size potential defects. Austenitic welds are coarse-grained, heterogeneous and anisotropic. This leads to aberration and scattering of the ultrasonic waves. Chassignolet al. (2010) presented several experimental results of ultrasonic testing of two austenitic welds exhibiting high anisotropy. In order to explain the observed display of wave propagation phenomena such as beam deviation; they used finite element modeling. The modeling is associated with a complete characterization of the inspected welds. Two essential characteristics of the welds are determined: the average elastic constants of the weld and the grain orientations. Their work associating structural characterization and modeling shows that a better understanding of the phenomena of ultrasonic propagation allow the interpretation and reliability of the industrial inspections of heterogeneous anisotropic welds to be improved

Harker et al. (1990) investigated the influence of austenitic weld structure on ultrasonic propagation. Metallurgical properties of the austenitic alloys produce a weld metal which is macroscopically anisotropic. The effect of this anisotropy on the propagation of ultrasonic waves through such material, high levels of scatter and attenuation. The results show that the apparent attenuation in an austenitic weld depends on the angle between the beam and the columnar grains.

Palanichamy et al. (1995) used ultrasonic velocity measurements to estimate average grain size in highly attenuating materials, austenitic stainless steel, using only the first back wall echo amplitudes. The grain size of a material is an important parameter which influences its mechanical properties. The results show that ultrasonic shear waves are more sensitive for grain size measurement than longitudinal waves.

Praveen et al. (2013) applied time of flight diffraction (TOFD) technique to detect and size a defect in austenitic stainless steel welds. Discrete wavelet transform based thresholding method is used as a signal processing tool to remove structural noise from ultrasonic TOFD A-scan signals acquired from austenitic stainless steel welds.

Pudovikov et al. (2008) demonstrated a new phase adjustment called reverse phase matching to consider ultrasonic wave propagation in anisotropic and dissimilar weld metals. This technique permits the acquisition of phase-corrected the acquisition of time signals (A-scans) that represent the actual sound propagation in the anisotropic

structure. Its application improves the reliability and sensitivity of ultrasonic inspection in austenitic welds.

Nath et al. (2009) performed detection and sizing of defects in complex geometry welded structures by using ultrasonic time of flight diffraction (TOFD). The TOFD models are developed to size and detected a vertical embedded or top surface crack in the complex geometry weld. While the results show that inclined welding defects in complex geometry weld, such as lack of sidewall fusion, are not suitable to detect by using this technique due to its current limitation.

The International Institute of Welding (IIW) (1986) stated recommendations for the ultrasonic examination of austenitic welds by manual scanning techniques which use the pulse echo method and A-Scan presentation, applications on butt welds with similar weld metals, problems involved in the examination of austenitic welds, the required conditions before examination the austenitic welds, ultrasonic wave propagation behavior, equipment description, calibration and characterization, development of an examination procedure, and evaluation report.

2.4 STRUCTURAL HEALTH MONITORING OF WELDS AND DAMAGE DETECTION

A significant amount of research has been carried out aimed at developing SHM techniques for crack detection using ultrasonic waves. Giurgiutiu (2002) detected a crack with PWAS that generate Lamb wave through aluminum plate, Poddar and Giurgiutiu (2015) detected and characterized a crack with Lamb wave, Yu and Giurgiutiu (2007)

used PWAS phased array for guided wave damage detection. Also Yu and Giurgiutiu (2007) produced in situ optimized phased array for Lamb wave, Yu (2006) discussed damage detection using guided wave with PWAS array. Moreover, Kijanka et al. (2015) used ultrasonic Lamb waves and piezoelectric rosettes for damage location.

Giurgiutiu and Cuc (2005) provided a significant review for the state of the art in an embedded ultrasonic non-destructive evaluation (NDE). This technology is enabled by the use of embeddable ultrasonic transducers that can be permanently attached to a structure. Giurgiutiu called these embeddable transducers “PWAS”, which is an acronym for piezoelectric wafer active sensor. The embedded ultrasonic technology enables active SHM to determine its current state of structural health. The authors show analytically and verified experimentally that Lamb wave mode tuning can be achieved by the judicious combination of PWAS dimensions, frequency value, and Lamb mode characteristics. The use of pitch-catch, pulse-echo, and phased array ultrasonic methods for Lamb wave damage detection is addressed. In each case, the conventional ultrasonic NDE results are contrasted with embedded NDE results. Other techniques, such as the time reversal method and the migration technique are also discussed.

Dhayalan et al. (2016) developed an ultrasonic high-frequency guided wave (HFGW) for the defect detection in shell weld of core support structure of fast breeder reactor. numerical modeling and FE simulation details are developed using explicit scheme. Based on the FE simulation studies, optimization of ultrasonic transducer location is explained to understand the generation and propagation characteristics of

HFGWs. The results show that in the high frequency–thickness product region, many of the higher-order modes that are propagating at similar group velocities form nondispersive high-frequency modes which are called HFGW modes. This type of waves allows for the inspection of structures over long distances and can be used to inspect inaccessible part.

Fan and Lowe (2009) studied the elastic waves guided by a welded joint in a plate experimentally and theoretically by time-step FE simulations. They apply a two-dimensional semi-analytical finite-element (SAFE) method to provide a modal study of the elastic guided waves. During the modal study a shear weld-guided mode, which is non-leaky and almost non-dispersive, has been discovered. The experimental work results show the existence of the shear weld-guided mode and the accuracy of the FE model. The authors are focused on the propagation of guided waves in a weld geometry. rather than inspection of a weld defects.

Fan and Lowe (2012) investigated the interaction of weld-guided waves with defects located in welded plate by using ultrasonic guided waves. The steel plate is welded by submerged arc welding technique with double V- grooves and has three weld defects located close to the heat affected zone (HAZ). Two types of shear transducer were used in the experiment for different frequency ranges to produce pulse echo signal which reflected from defects in the heat affected zone on a welded plate. The monitoring of the incident signal and the detection of the reflected signal was achieved using a laser interferometer with dual differential fiber optic lines (Polytec OFV 2700). The results of

experimental work indicate good matching with the trend of the reflection coefficient spectrum predicted by FE simulations. Since, the mode shape of the weld guided mode is not consistent along the weld due to the variation of the cross-section of the geometry. It is difficult to apply the weld guided mode to size the defects.

Kamas et al (2014) discussed theoretical and experimental analyses of Rayleigh waves

in thick steel plate with butt weld. A pitch-catch experiment with PWAS is done for the welded area and the plate itself. Both experimental and FEA results verified the fact that the quasi-Rayleigh wave is guided and tuned by the weld. Also, quasi-Rayleigh wave damage interaction by simulated damage is theoretically investigated.

Connolly (2009) developed a forward model to simulate the propagation of ultrasonic waves through austenitic stainless steel V-welds. This model can trace the rays through an anisotropic and inhomogeneous weld. The ray-tracing model is validated against the results of finite element simulations.

2.5 CONNECTION TO THE TOPIC OF THIS MS RESEARCH

This chapter reviewed the studies about austenitic stainless steel, fabrication of artificial welding defects methods, Ultrasonic NDT method for welding inspection, and SHM methods for damage detection. These studies provided a good knowledge to deal with austenitic stainless steel weld and methods of its inspection. These researches will support of this MS work.

CHAPTER 3

AUSTENITIC STAINLESS STEEL:

MICROSTRUCTURE AND WELDING CHARACTERISTIC

3.1 INTRODUCTION

Austenitic steels are an important group of materials which are generally used for applications where resistance to corrosion, or high strength and creep resistance, are required at elevated temperatures applications such as household and community equipment, transport, food industry, industrial equipment, nuclear structural materials, chemical and power engineering, cryogenics, and building industry. The optimum choice of the grades would depend on service needs and this would require a clear understanding of the metallurgical parameters, which control the microstructure and thus the mechanical properties, formability and corrosion resistance. Austenitic steels may also be used where ductility at very low temperatures is essential, such as in cryogenic vessels. The word 'steel' means that the material is iron-based, while the adjective 'stainless' implies absence of staining, rusting or corroding in environments where normal steels are susceptible. Austenitic stainless steels are the largest group in the stainless steel family. The most widely used are those in the AISI300 series, a system of Fe-Cr-Ni alloys. They are excellent corrosion resistance, paramagnetic, easily fabricated and formed with good cold formability, excellent weldability in all thickness, suitable for both high and low

temperature (Cryogenics at -190 C° to 870 C°). They are normally supplied in the quench-annealed state, which means that they are soft and highly formable. Their hardness and strength are increased by cold working but not by heat treatment (Lai et al., 2012; Khatak & Raj, 2002; Hudgell & Gray, 1985).

3.2 METALLURGY AND MICROSTRUCTURE CHARACTERISTICS OF AUSTENITIC STAINLESS STEEL

The physical metallurgy of stainless steels can be understood with the aid of the iron-chromium (Fe-Cr) phase diagram, shown in Figure 3.1. All alloys in this binary system solidify as delta (δ) ferrite. The austenite gamma (γ) phase exists in a region referred to as the γ loop. The addition of chromium to pure iron promotes constriction of the temperature range over which the austenite phase exists until it disappears at 13% chromium. Hence, alloys with chromium content less than 13% transform from ferrite to austenite during heating into the γ loop and then back to ferrite on cooling. The minimum point in the loop occurs at about 850°C (1562°F) and 6.5% chromium. Rapid cooling of an alloy from the austenite phase field promotes the formation of the non-equilibrium martensite phase. At chromium levels around 45% to 50%, the brittle sigma (σ) phase precipitates from the ferrite phase during cooling at temperatures below about 830°C (1526°F). Sigma is an intermetallic phase with a composition near Fe Cr. The formation of sigma normally results in loss of toughness and can lower corrosion resistance because it removes chromium from the surrounding matrix as it forms. At temperatures below approximately 475°C (885°F), the ferrite phase separates into a low-chromium ferromagnetic alpha (α) phase and a high-chromium paramagnetic α' phase via a spinodal

decomposition reaction. This separation leads to the so-called embrittlement phenomenon that strongly influences mechanical properties.

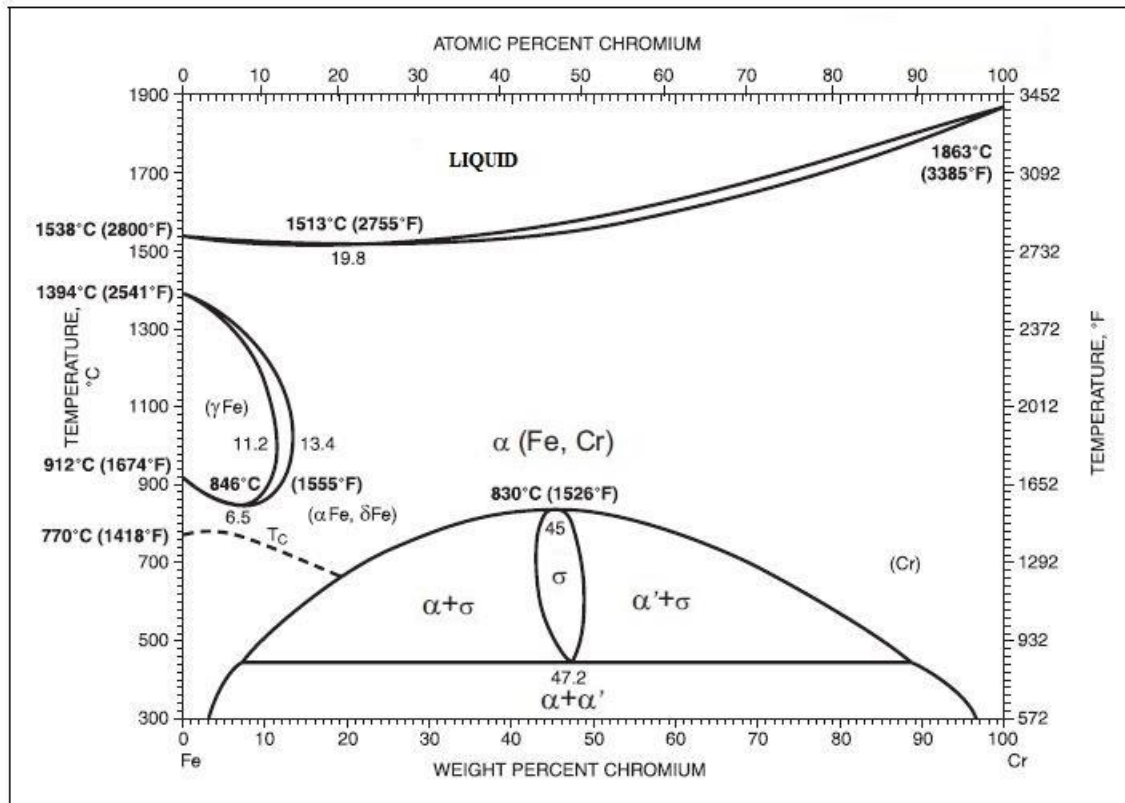


Figure 3.1 The Fe-Cr Binary Phase Diagram (AWS, 2011)

The term microstructure is used because virtually all of the geometric features of the phases and other structures that determine the properties of steels are observable only with the aid of microscopy. The microstructure of a type of steel is dependent on the amount of the various alloying elements that it contains and on both its present temperature and thermal history.

Austenitic stainless steels are formulated and thermo-mechanically processes such that the microstructure is primarily austenite, either fully austenitic or a mixture of austenite

and ferrite as shown in Figure 3.2 Microstructure of austenitic stainless steel plate type 304 and Figure 3.3 Highly magnified crystalline structure of austenitic stainless steel..

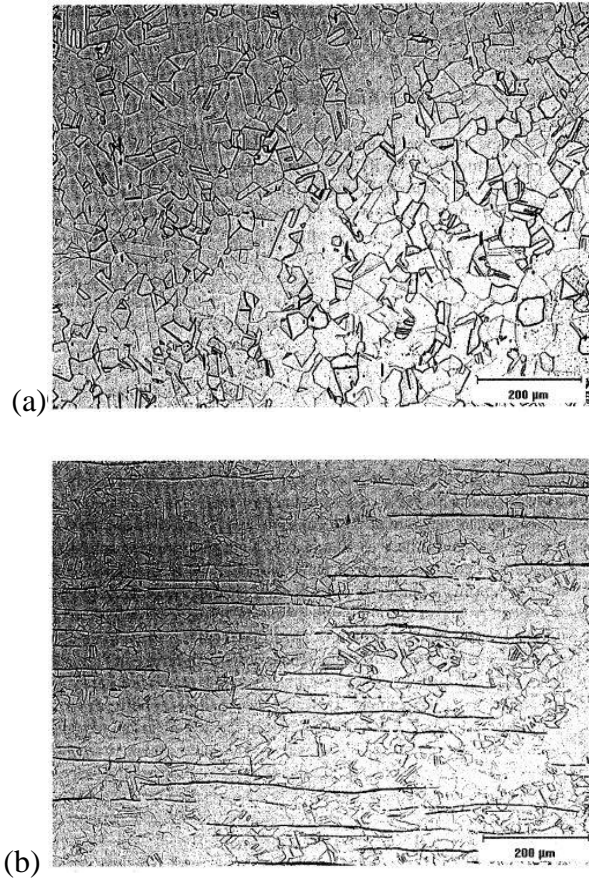


Figure 3.2 Microstructure of austenitic stainless steel plate type 304

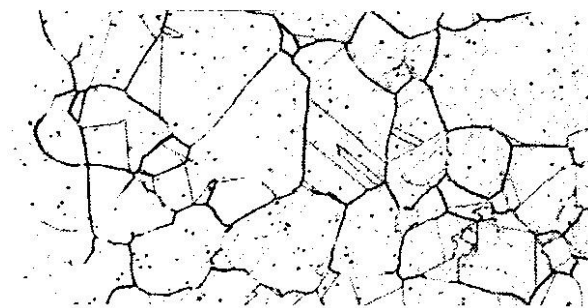


Figure 3.3 Highly magnified crystalline structure of austenitic stainless steel.

Since the Cr contents of austenitic stainless steel exceed 16 weight%, their equilibrium microstructure at room temperature would be fully ferritic (delta), if no other austenitizing alloying elements were added to the material. Elements that are most often used to obtain an austenitic microstructure are Ni, Mn, C and N. It should be noted the leaner steels in the 300 series (Fe-Cr-Ni alloys) may contain ferrite at elevated temperatures. On the other hand, those in this series that are highly alloyed are usually fully austenitic (gamma). However, inhomogeneity in the original casting may result in ferrite being present in some regions. The presence of ferritizing elements like Mo, Ti may also lead to ferrite in the final microstructure. Hence, when these ferritizers are present, the Ni content should be increased accordingly.

Austenitic stainless steels have better ductility and toughness than carbon steels and alloy steels because of their face-centered-cubic crystal structure, Figure 3.4

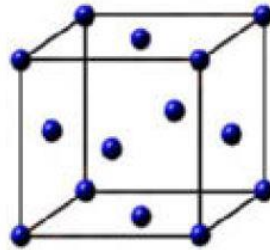


Figure 3.4 Face-Centered Cubic(FCC) unit cell

Steels of the austenitic group exhibit good resistance to corrosion and oxidation at temperatures up to 650°C (1200°F) or higher. These steels also exhibit excellent ductility and toughness in this temperature range. Corrosion and oxidation resistance is imparted primarily by a high chromium content, generally greater than 16 weight %. The addition

of the austenite-stabilizing elements carbon, nickel, and nitrogen in various combinations and content, promotes an austenitic structure in the service temperature range. In some alloys, austenite is stable from room temperature to the melting-temperature range. The austenitic (gamma [γ]) phase has a face centered-cubic crystal structure, is paramagnetic, and consists of a solid solution of carbon, chromium, nickel, and other alloying elements in iron. The predominance of an austenitic crystal structure in these steels is responsible for their excellent ductility and toughness.

The basic composition of austenitic stainless steel 304 includes 18% chromium and 8% nickel alloy often called 18/8 stainless. The Cr and Ni equivalent numbers suggested by Schaeffler and are as follows.

$$Cr_{eq} = \%Cr + \%Mn + 1.5\%Si + 0.5\%Cb^n$$

$$Ni_{eq} = Ni + 30\%C + 30\%N + 0.5\%Mn$$

The austenitic stainless steels contain other intentionally added alloying elements, including manganese and silicon, and may contain molybdenum, niobium, titanium, and nitrogen. Manganese is effective in combining with sulfur to form relatively stable manganese sulfides. Manganese increases solubility of nitrogen, which in turn, helps stabilize austenite.

Silicon is generally added for deoxidizing purposes in concentrations up to 1 wt %. At higher levels, silicon is effective in improving high-temperature oxidation and scaling resistance. Silicon also enhances the fluidity of the molten metal, which has important implications for both welding and casting behavior. However, silicon in weld metal that has very low or no ferrite promotes solidification cracking.

Molybdenum, a ferrite-forming element, is added to improve resistance to pitting corrosion and to provide solid-solution strengthening.

Niobium and titanium are both potent carbide-forming elements; they are also ferrite formers and are added to improve resistance to intergranular corrosion.

Nitrogen is a potent austenite-forming element that increases both the strength and pitting, localized areas of corrosion are created by solution ions spread beneath protective chromium barriers to compromise internal structures, resistance of the steel when added in concentrations in the range from 0.1 to 0.25 wt %.

Austenitic stainless steels are often used in industrial plants, chemical processing, food production, marine hardware, furnaces, heat exchangers, gas turbines, and cryogenic vessels because of their excellent corrosion resistance, better creep rupture strength at high temperature, and impact resistance at low temperatures. (Lai et al., 2012; AWS, 2011; Tseng & Hsu, 2011).

3.3 WELDING CHARACTERISTICS OF AUSTENITIC STAINLESS STEELS

The metallurgical features of the common-grade stainless steels generally determine the weldability characteristics of the steel alloys. The weldability of austenitic stainless steels is governed by their susceptibility to solidification and liquation cracking. Thermal expansion, thermal conductivity, and electrical resistivity have significant effects on the weldability of stainless steels. The relatively high coefficient of thermal expansion and the low thermal conductivity of austenitic stainless steels require more complex techniques to minimize distortion during welding than are needed for the other stainless steels. The common grades of stainless steel are readily joined by arc, electron

beam, laser beam, resistance, and friction welding processes. Gas metal arc (GMAW), gas tungsten arc (GTAW), flux cored arc (FCAW), and shielded metal arc (SMAW) welding are commonly used.

In general, when a metal is cooled from the liquid state to the solid state, because cooling cannot be exactly the same for every atom, certain atoms will be attracted to each other to form a unit cell ahead of others. This unit cell becomes the nucleus for crystal formation. As the cooling continues other atoms will take up their positions alongside this nucleus and the crystals, or as it is usually referred to for metals, the grain, will grow in size. This orderly growth of the grain continues in all directions until it runs into interference from other grains that are forming simultaneously about other nuclei. Figure 3.5 illustrates the process of the formation of grains and grain boundaries.

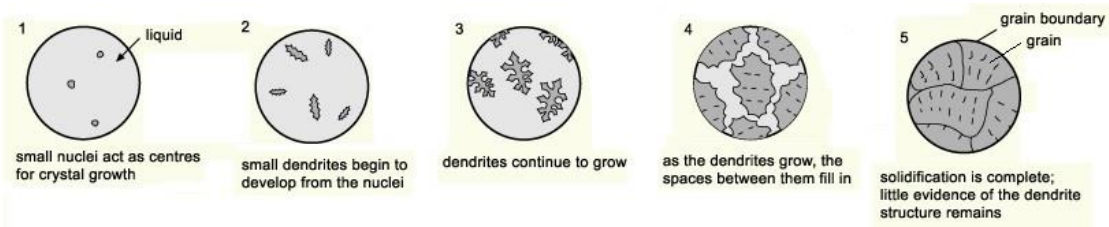


Figure 3.5 Solidification of a metal. Adapted from (www.mtarr.co.uk)

Austenitic stainless steel weld metals can vary significantly from the base metals with respect to both microstructure and mechanical properties. Alloys that are fully austenitic in the wrought form often exhibit a two phase austenitic/ferritic microstructure in the weld metal after cooling to room temperature as illustrated in Figure 3.6 and Figure 3.7.

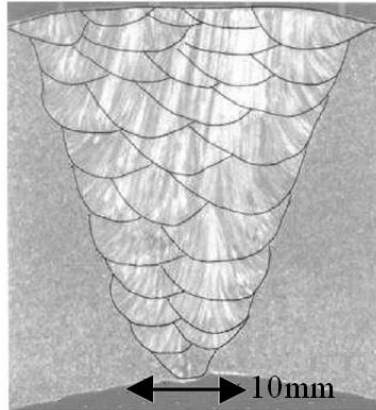
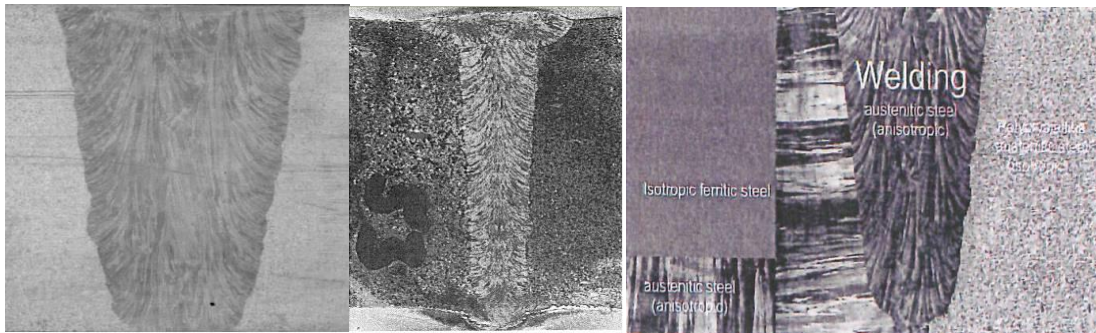


Figure 3.6 Typical weld microstructure, showing both weld pass boundaries (black lines) and grain boundaries (alternating grey and white bands). Original image taken from (Moysan et al., 2003)



(a)

(b)

(c)

Figure 3.7 Columnar grains structure of austenitic weld materials: (a) standard pipe to pipe weld, (b) narrow gap weld, (c) dissimilar weld (Pudovikov et al., 2008)

In general, the nominally austenitic microstructure of as-deposited stainless steel weld metal at room temperature consists primarily of austenite, with a ferrite content. For arc welding processes, this phase balance depends primarily on the weld metal composition, and to a lesser extent, on process conditions as they influence base metal dilution, weld solidification, and cooling rates.

Austenitic stainless steel weld metals can solidify with either austenite or ferrite as the primary phase. When austenite is the primary solidification phase, the as-deposited weld metal will either be fully austenitic or may contain ferrite in a small fraction by volume. This type of ferrite, called *eutectic ferrite*, is found at solidification sub-grain (cellular or dendritic) boundaries, Figure 3.8.

When ferrite is the primary solidification phase, the final ferrite content of the as-deposited weld metal is determined by the nature of the ferrite-to-austenite transformation that occurs in the solid state on cooling.

The primary phase of solidification may be either austenite or delta ferrite, depending on the composition of the specific heat.

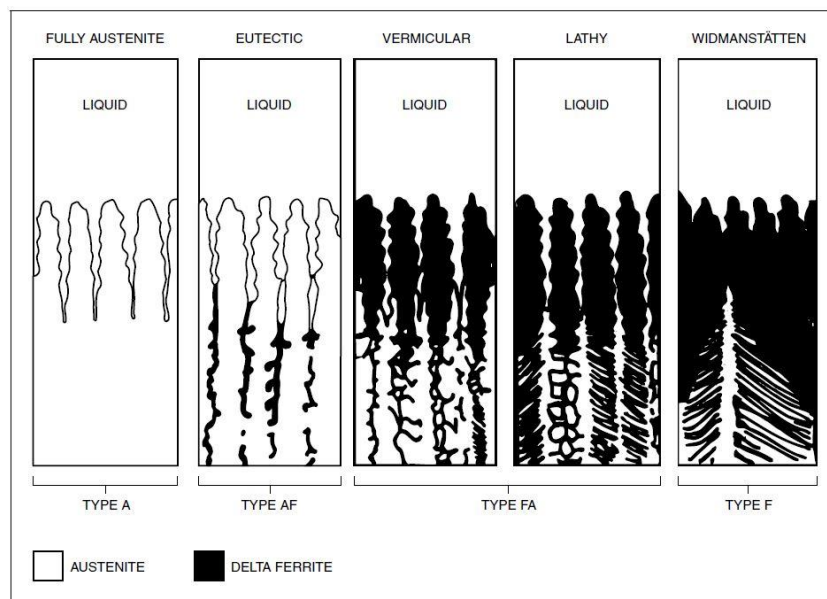


Figure 3.8 Various ferrite morphologies (AWS, 2011)

The phase fractions in austenitic stainless steel welds can be estimated from the chemical composition of the deposited weld metal with the aid of many of constitution

diagrams and empirical relationships. Foremost among these diagrams are those developed by Schaeffler, DeLong, and the Welding Research Council, Figure 3.9.

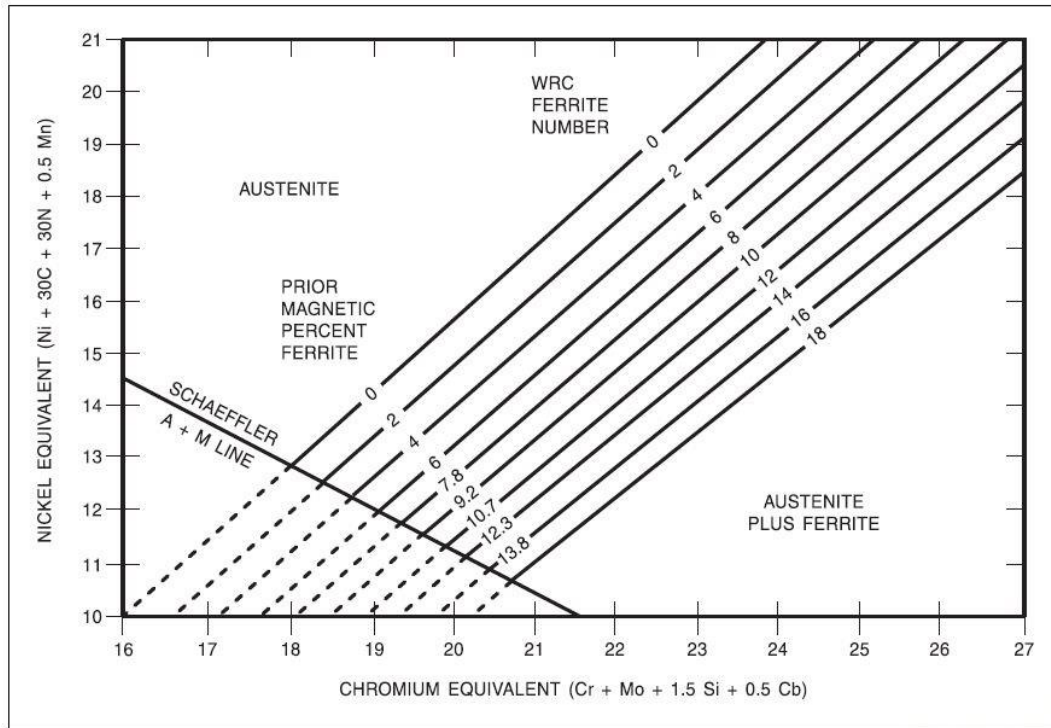


Figure 3.9 DeLong diagram for estimating the microstructure of stainless steel weld metal (AWS, 2011)

In a welding process of multi-pass join (Figure 3.10), there are two processes take place simultaneously: Continuous steel melting and continuous solidification of molten steel. During welding, the crystallization process is almost completely controlled by the dissipation of heat into the solid metal, with only a small amount of heat being dissipated into the surrounding atmosphere. This process has a decisive influence on the type, size and orientation of the crystals being formed. The formation of different crystal configurations (dendrites, globular crystals, cellular crystals) is determined by the temperature situation at the liquid-solid interface. High cooling rates promote a cellular

solidification; medium cooling rates a dendritic solidification. In stainless weld metals, we can often find a cellular solidification structure at the bottom of a bead and dendritic structures in the middle of the same bead. In the case of very high cooling rates, there is the possibility of the formation of globular structures. In stainless steel weld metals, however, the latter are rather rare because the base metal on which the weld metal is being deposited will often predetermine a preferred crystal orientation for newly formed weld metal crystals. Direction of growth is strongly determined by the direction of greatest dissipation of heat. At normal cooling rates, zones with varying crystal configurations will be formed during the solidification of a welding pass from stainless steel weld deposits(Folkhard et al., 1988).

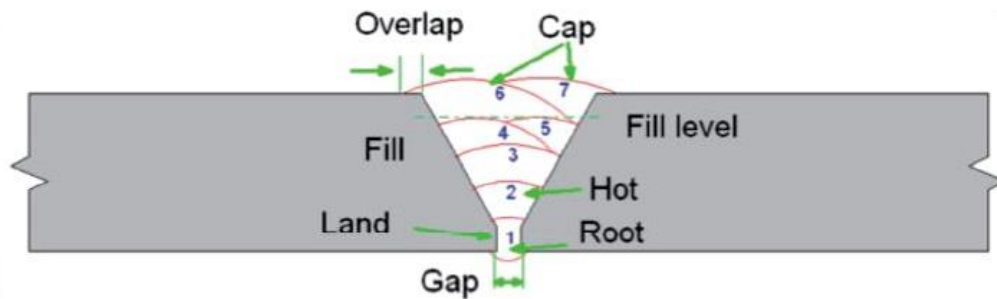


Figure 3.10 Multi-passes joint

Kumar et al., (2006); Rodríguez et al., (2009); Rabenberg (2012); Malpally, (2014) studied the characteristics of HAZ and mechanical properties of the welded areas by using Miniature Specimen Technique (MST) as an NDT tool. MST sample, Figure 3.11, is taken from the welded specimen to estimate the properties, Figure 3.12

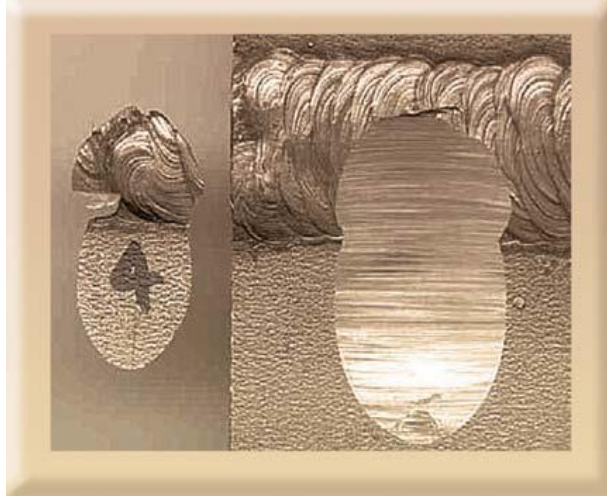


Figure 3.11 Sample from HAZ of welded SS plate. Kumar et al., (2006)

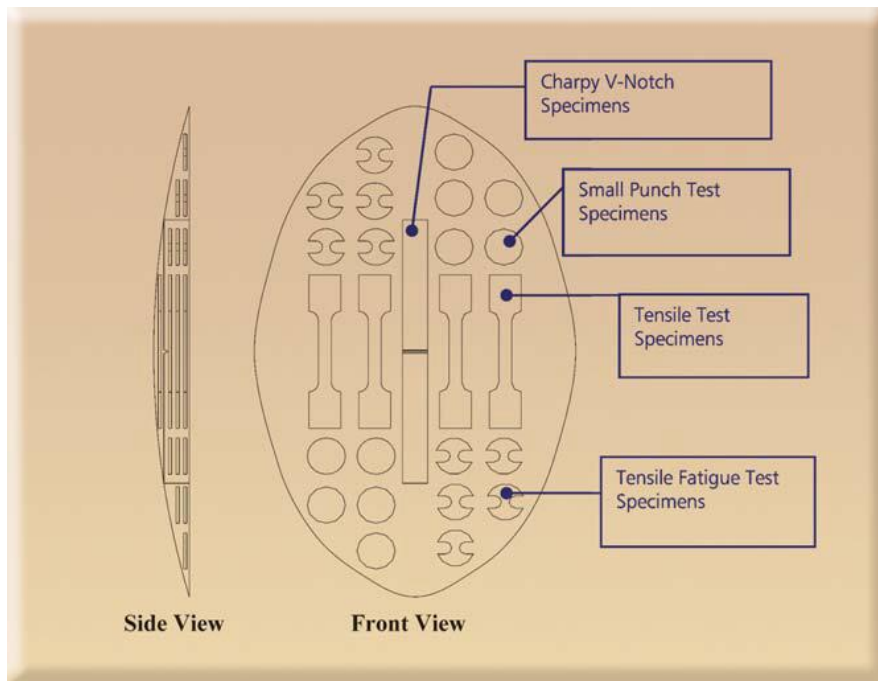


Figure 3.12 Layout of MST sample. Kumar et al., (2006)

CHAPTER 4

NDT OF WELDED STRUCTURES: ULTRASONIC TESTING

4.1 INTRODUCTION

Nondestructive examination (NDE), nondestructive evaluation (NDE), nondestructive inspection (NDI), or nondestructive testing (NDT) is an examination, test, or evaluation performed on any type of test object without changing or altering that object in any way, in order to determine the absence or presence of conditions or discontinuities that may have an effect on the usefulness or serviceability of that object. Nondestructive tests may also be conducted to measure other test object characteristics, such as size; dimension; configuration; or structure, including alloy content, hardness, grain size, etc.

Today, there is a new emphasis on in-service inspection of fabricated structures and on structure monitoring. Non-destructive testing is an inspection process which forms part of the whole quality assurance/quality control (QA/QC) scheme. Nondestructive testing (NDT) of deep foundations has become an essential component of deep foundation construction quality assurance. Its very existence has improved the front end of the process, that being quality control. Although NDT cannot guarantee that buildings will not collapse, planes will not crash, and products will not fail, it plays a significant role in minimizing the possibilities of failure. Other variables, such as inadequate design and improper application of the object, may contribute to failure even when NDT is

appropriately applied (Hellier, 2003; Halmshaw, 1996; Hertlein & Davis, 2006). NDT is carried out using a wide range of techniques including X-ray, γ -ray and neutron radiography, optical and infra-red radiation imaging, eddy currents, magnetic flux leakage and various modalities of ultrasound. Ultrasonic testing (UT) is the most important of these approaches, with more than half of all inspection done with one or other form of ultrasonic (Every, 2014).

4.2 ULTRASONIC TESTING (UT)

Among several NDT methods, ultrasonic testing (UT) is the most commonly and widely used one in the industry (Praveen et al., 2013) for two reasons:

1. Acoustic waves at ultrasonic frequencies have a lot of fundamentally new knowledge to be investigated to get a better understanding of how ultrasonic waves occur in nature.
2. Ultrasonic has many applications occur in a very broad range of disciplines such as covering chemistry, physics, engineering, biology, food industry, medicine, oceanography, seismology (Cheeke, 2012).

Ultrasonic is defined as that band above 20 kHz as shown in Figure 4.1. It continues up into the MHz range and finally, at around 1 GHz, goes over into what is conventionally called the hypersonic regime. The full spectrum is shown in Figure 4.2 where typical ranges for the phenomena of interest are indicated

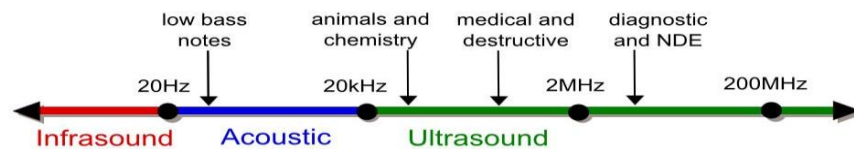


Figure 4.1 Ultrasound range diagram (wikimedia.org)

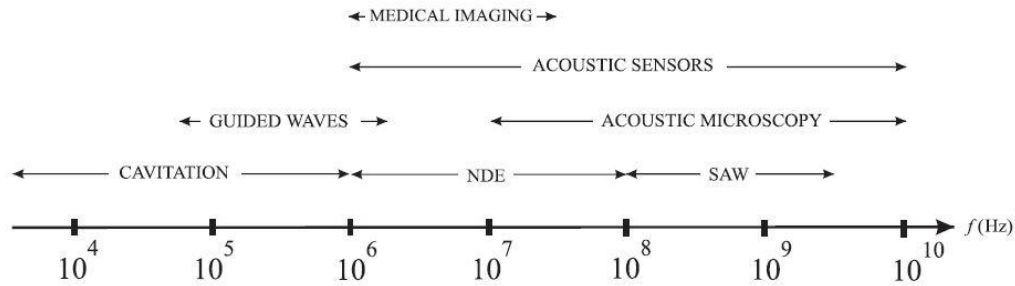


Figure 4.2 Common frequency ranges for various ultrasonic processes (Cheeke, 2002)

There are four general approaches to ultrasonic NDT:

1. Classical NDT

The field has two separate but related paths. In the first, defect detection, we are looking at *in situ*, field inspection techniques for the detection of various defects such as cracks in rails of railway lines, stress corrosion cracks in pipelines. Detection and characterization of these defects may include determining their existence, making an acoustic image of them, and obtaining quantitative information on them. A second avenue of NDT involves determination of the intrinsic material properties themselves, such as ultrasonic attenuation measurements to determine grain size distribution in alloys, determination of the elastic constants of an anisotropic ceramic coating.

2. NDT for material processing

This is a more modern approach, in many cases an ideal yet to be attained. In the so-called intelligent processing or manufacturing operation, sensors are placed at strategic points in the process technology diagram so that the physical and chemical properties are monitored during production. Thus, the appropriate preventive steps are taken during the manufacturing process to eliminate or reduce the probability of failure of the material during its working life.

3. Intelligent materials

Many large and complex industrial structures such as aircraft fuselages and bridges. incorporate networks of embedded sensors. This is particularly feasible in composite materials where the sensor probes can be incorporated during fabrication. Such sensors give continuous monitoring of the state of the material during service, and by detecting signs of incipient failure by the detection of small cracks, stress, etc. they perform a valuable NDT function.

4. Modern signal processing

Ultrasonic inspection has evolved considerably from the original direct pulse echo approaches. Techniques have been developed to recover signals buried in the noise. New approaches, such as neural network signal processing, can be used to help in flaw identification and determination of the ultrasonic propagation path in complex geometries (Cheeke, 2002).

4.3 ULTRASONIC BEAM CHARACTERISTICS

All transducers of the kind most commonly used for ultrasonic NDT have the following fundamental functional properties:

- 1 Type: The transducer is identified according to function as a contact, delay line, angle beam, or immersion type. Inspected material characteristics (such as surface roughness, temperature, accessibility as well as the position of a defect within the material, and the inspection speed) all influence the selection of transducer type.
- 2 Size. The diameter or length and width of the active transducer element, which is normally housed in a somewhat larger case.

- 3 Frequency. The number of wave cycles completed in one second, normally expressed in kilohertz (kHz) or megahertz (MHz). Most industrial ultrasonic testing is done in the 500 kHz to 20 MHz frequency range, so most transducers fall within that range, although commercial transducers are available from below 50 kHz to greater than 200 MHz. Penetration increases with a lower frequency, while resolution and focal sharpness increase with a higher frequency.
- 4 Bandwidth. The portion of the frequency response that falls within specified amplitude limits. In this context, it should be noted that typical NDT transducers do not generate sound waves at a single pure frequency, but rather over a range of frequencies centered at the nominal frequency designation. The industry standard is to specify this bandwidth at the -6 dB (or half amplitude) point.
- 5 Waveform duration. The number of wave cycles generated by the transducer each time it is pulsed. A narrow bandwidth transducer has more cycles than a broader bandwidth transducer. Element diameter, backing material, electrical tuning, and transducer excitation method all impact waveform duration.
- 6 Sensitivity. The relationship between the amplitude of the excitation pulse and that of the echo received from a designated target.
- 7 Beam profile. As a working approximation, the beam from a typical unfocused disk transducer is often thought of as a column of energy originating from the active element area that expands in diameter and eventually dissipates

The sound field of a transducer is divided into two zones: the near field and the far field (see Figure 4.3). The *near field* is the region close to the transducer where the sound pressure goes through a series of maximums and minimums, and it ends at the last on-

axis maximum at distance N from the face. Near field distance N represents the natural focus of the transducer.

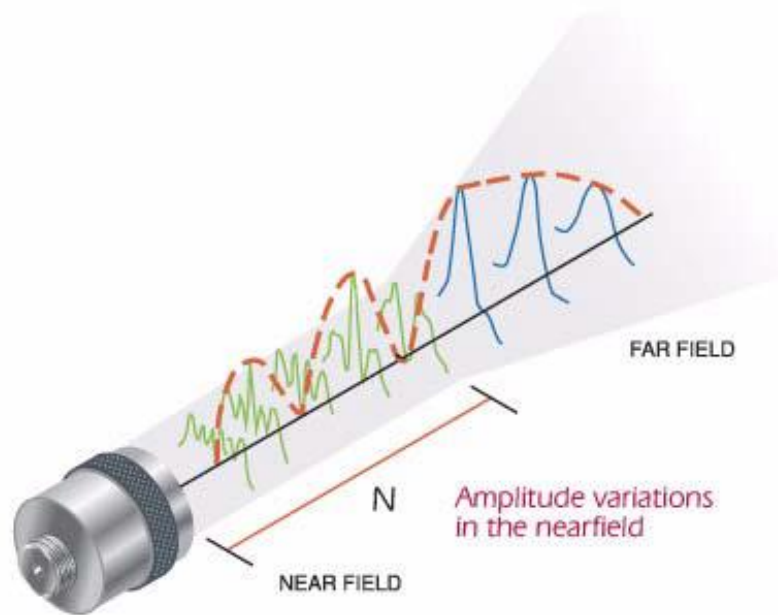


Figure 4.3 The sound field of a transducer. (Olympus, 2010)

The far field is the region beyond N where the sound pressure gradually drops to zero as the beam diameter expands and its energy dissipates. The near field distance is a function of the transducer's frequency and element size, and the sound velocity in the test medium, and it can be calculated for the square or rectangular elements commonly found in phased array testing as follows:

$$N = \frac{k L^2 f}{4 c} \quad \text{or} \quad N = \frac{k L^2}{4 \lambda}$$

Where:

N=near-field length

k=aspect ratio constant (see below)

L=length of element or aperture

Z =frequency

c =sound velocity in test material

λ =wavelength $\text{wavelength} = \frac{c}{f}$

In the case of circular elements, k is not used and the diameter of the element (D) is used instead of the length term:

$$N = \frac{D^2 f}{4 c} \quad \text{or} \quad N = \frac{D^2}{4 \lambda}$$

4.4 FUNDAMENTAL PROPERTIES OF SOUND WAVES

Beam spreading. In principle, the sound wave generated by a transducer travels in a straight line until it encounters a material path length is longer than the near-field distance, the beam also increases in diameter, diverging like the beam of a spotlight.

4.4.1 ATTENUATION.

As it travels through a medium, the organized wave front generated by an ultrasonic transducer begins to break down due to an imperfect transmission of energy through the microstructure of any material. Organized mechanical vibrations (sound waves) turn into random mechanical vibrations (heat) until the wave front is no longer detectable. This process is known as *sound attenuation*

A wave with reducing amplitude is illustrated in Figure 4.4. The reduction (or increase) in the amplitude of a waveform is expressed as attenuation (or gain), by the logarithm of the ratio of the magnitudes of the original to the attenuated amplitudes, a and a_0 . This is commonly measured in decibels (Lempriere, 2002; Olympus, 2010).

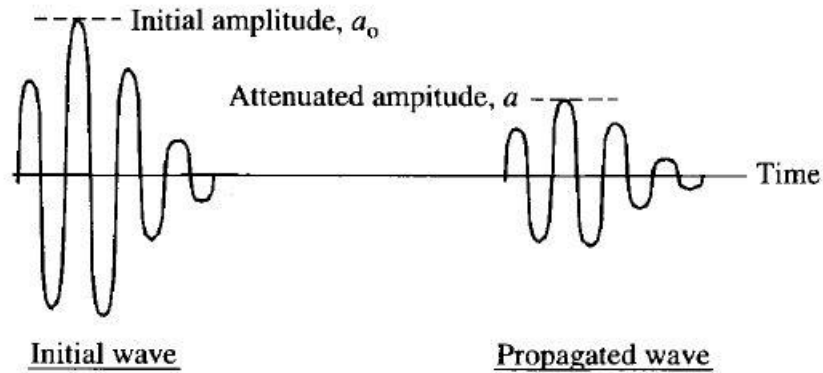


Figure 4.4 Decay of a propagating pulse (Lempriere, 2002)

Figure 4.5 shows the attenuation of a wave due to grain scattering such as in austenitic stainless steel.

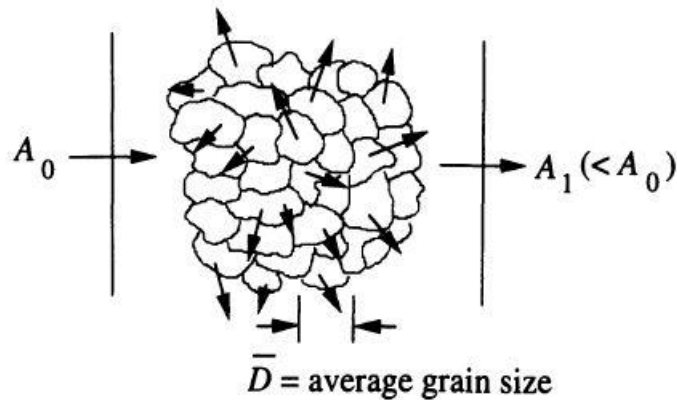


Figure 4.5 Attenuation of a wave due to grain scattering (Lester 1998).

4.4.2 REFLECTION AND TRANSMISSION AT A PERPENDICULAR PLANE BOUNDARY.

When a sound wave traveling through a medium encounters a boundary with a dissimilar medium that lies perpendicular to the direction of the wave, a portion of the wave energy is reflected straight back and a portion continues straight ahead. The percentage of reflection versus transmission is related to the relative acoustic impedances

of the two materials, with acoustic impedance in turn being defined as material density multiplied by speed of sound. The reflection coefficient at a planar boundary (the percentage of sound energy that is reflected to the source) can be calculated as follows:

$$R = \frac{Z_2 - Z_1}{Z_2 + Z_1}$$

Where:

R= reflection coefficient in percent

Z1= acoustic impedance of first medium

Z2= acoustic impedance of second medium

4.4.3 REFRACTION AND MODE CONVERSION AT NON-PERPENDICULAR BOUNDARIES.

When a sound wave traveling through a material encounters a boundary with a different material at an angle other than zero degrees, a portion of the wave energy is reflected forward at an angle equal to the angle of incidence. At the same time, the portion of the wave energy that is transmitted into the second material is refracted in accordance with Snell's Law, which was independently derived by at least two seventeenth-century mathematicians. Snell's law relates the sines of the incident and refracted angle to the wave velocity in each material as diagramed in Figure 4.6.

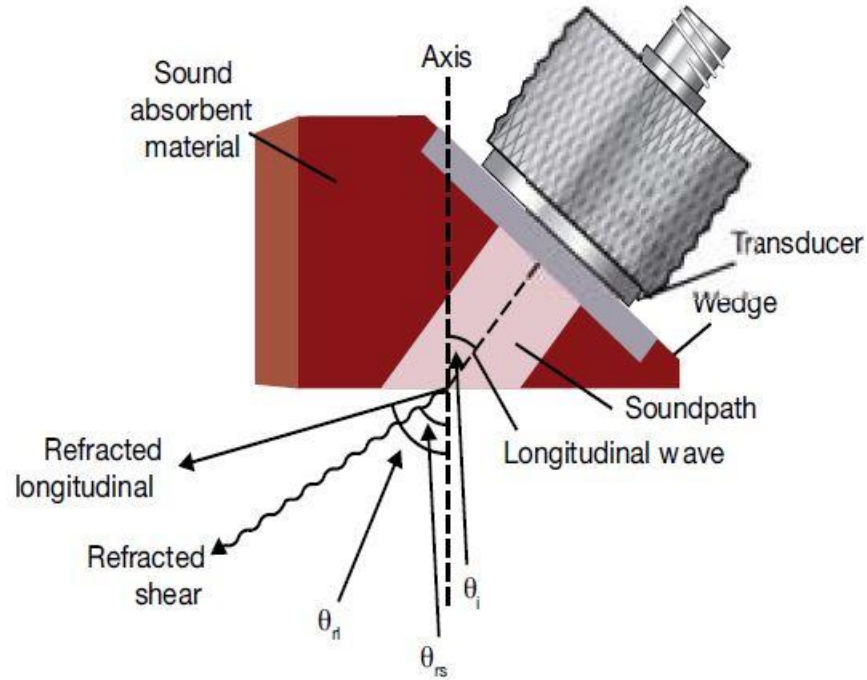


Figure 4.6 Sound wave refraction and mode conversion. (Olympus, 2010)

$$\frac{\sin \theta_i}{c_i} = \frac{\sin \theta_{rl}}{c_{rl}} = \frac{\sin \theta_{rs}}{c_{rs}}$$

where:

θ_i = incident angle of the wedge

θ_{rl} = angle of the refracted longitudinal wave

θ_{rs} = angle of the refracted shear wave

c_i = velocity of the incident material (longitudinal)

c_{rl} = material sound velocity (longitudinal)

c_{rs} = velocity of the test material (shear)

Figure 4.7 shows the amplitude of different wave modes.

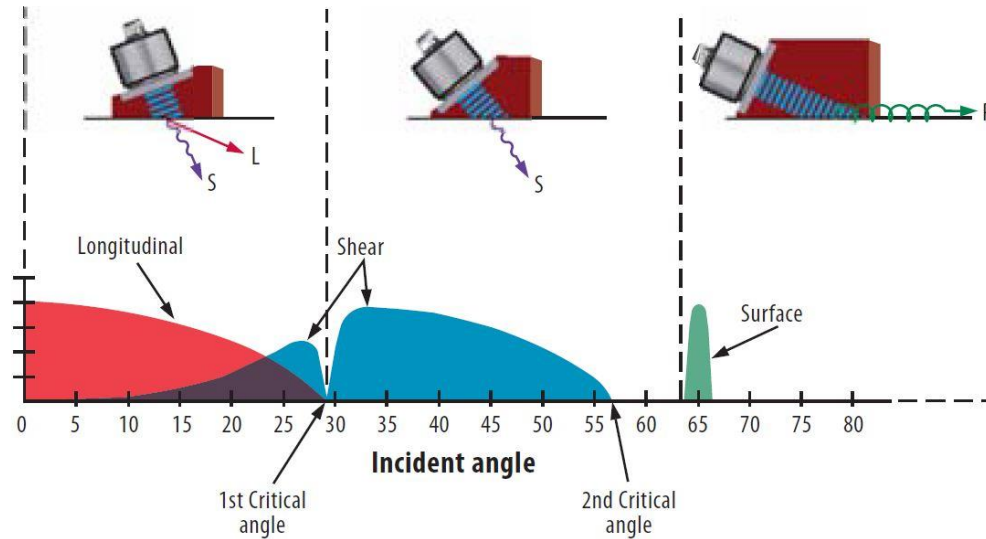


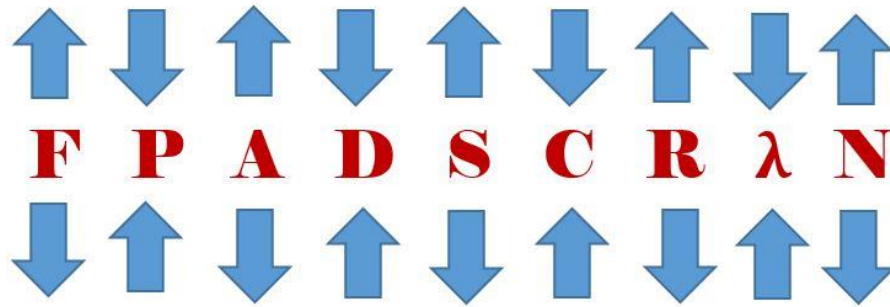
Figure 4.7 Relative amplitude of wave modes

There are two classes of measurable features: Time and Amplitude. The propagation time for a wave can be used to measure wave speed when the path length is known or the path length when the wave speed is known. Wave speed can be used to calculate density if elasticity and wave type are known, or elastic properties if density is known. The path length allows accurate measurement of distances (e.g., thickness and internal dimensions). The amplitude of a wave can be used to determine the damping (energy absorption) characteristics of the medium, thereby indicating the nature of the material. Energy is an important quantity that can be determined by the amplitude integrated over time. (Lempriere, 2002).

Ultrasonic Characteristics of Austenitic Stainless Steel Welds Austenitic Stainless steel has structural importance in nuclear industry due to its excellent mechanical and chemical properties. The weld region of austenitic stainless steel is highly anisotropic because of the columnar grain structure. Ultrasonic waves interacting with these grains result in high level scattering noise that may mask the defect signals (Praveen et al, 2013).

Certain operating conditions may cause a range of changes in the integrity of the component, and therefore require nondestructive testing at reasonable intervals. These in-service inspections are often performed using ultrasonic techniques, in particular when cracking is of specific concern. However, the coarse, dendritic grain structure of the weld material, formed during the welding process, is extreme and unpredictably anisotropic. Such structure is no longer direction-independent to the ultrasonic wave propagation; therefore, the ultrasonic beam deflects and redirects and the wave front becomes distorted. Thus, the use of conventional ultrasonic testing techniques using fixed beam angles is very limited and the application of ultrasonic Phased Array techniques becomes desirable(Pudovikov, 2008).

The relation between ultrasonic variables is showed clearly in the Figure 4.8. When the frequency increases, penetration decreases, attenuation increases, divergence decreases, sensitivity increases, crystal thickness decreases, resolution increases, wave length decreases, near field increases and vice versa.



- **F**requency
- **P**enetration
- **A**ttenuation
- **D**ivergence (Beam Spread)
- **S**ensitivity
- **C**rystal Thickness
- **R**esolution
- **λ**: Wavelength
- **N**ear Field
- **D**iameter of Crystal Thickness

Figure 4.8 NDT-UT variables relationship. (ASNT, 2010)

4.5 WAVE SCATTERING

The interaction of a wave with a non-uniformity produces reflections and transmissions in multiple directions, called scattered waves, in a pattern called the scattering pattern. After scattering, constructive interference creates a wave which propagates in the same direction as the incident wave, called the forward scattered wave. The wave pattern propagating backward toward the source is called the backscatter. The response of a scatterer to an incident wave can arise through deformation producing an omnidirectional scatter, or by motion as a whole producing a directed scatter. These effects can be regarded as created by sources of motion which are proportional to the differences in elastic properties and density between the scatterer and the unperturbed medium (Lempriere, 2002).

Figure 4.9 shows the wave scattering from the grain boundary due to the size of the grain and the anisotropic structure.

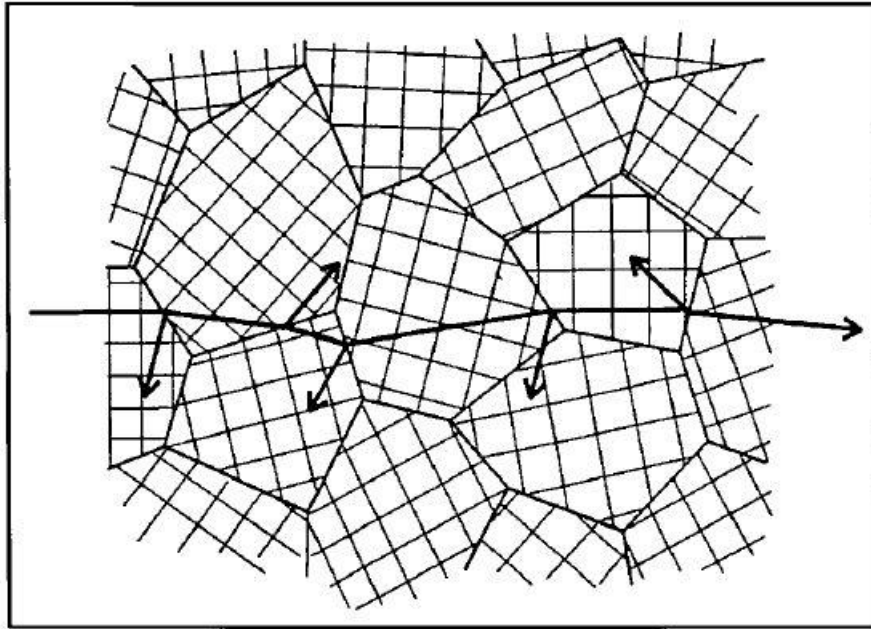


Figure 4.9 A cross-section through columnar grains showing (Hudgell, 1994)

CHAPTER 5

FUNDAMENTALS OF GUIDED WAVES AND SHM WITH PWAS

This chapter introduces fundamentals of guided wave theory, basic concepts of Structural Health Monitoring (SHM), and piezoelectric wafer active sensors (PWAS) for generating and receiving guided waves. It will also serve as the theoretical prerequisite for the wave modeling and simulation tasks. First, the guided wave theory is briefly reviewed by types, including Rayleigh waves, shear horizontal (SH) plate waves, straight crested Lamb waves, circular crested Lamb waves, and guided waves in rods, pipes, and waveguides with arbitrary cross sections. Next, guided waves based SHM concepts and techniques are introduced. The key points of modeling guided wave based SHM are discussed. Finally, the PWAS transducers are introduced, including their working principle, their coupling with guided waves and tuning effect, and their operation modes.

5.1 BRIEF REVIEW OF GUIDED WAVES THEORY

Ultrasonic guided waves are revolutionizing the approach to nondestructive testing (NDT) and structural health monitoring (SHM) (Rose, 2014). An elastic wave that propagates through a waveguide is called a guided wave. A waveguide is a structure with boundaries that help elastic waves to propagate from one point to another. Waveguides can be of any shape or size. Common types of waveguides are plates, pipes, cylindrical rods (solid or hollow), and bars (of rectangular cross sections or other geometric shapes)

Figure 5.1. In some of these waveguides the elastic wave can easily propagate, while in other cases the propagating guided waves decay fast (Kundu, 2004).

Ultrasonic guided waves are used in nondestructive testing (NDT) and structural health monitoring (SHM), and in many other engineering fields (Rose 2014). Guided waves can travel over considerable distances in structures with little attenuation and remain confined inside the walls of a thin-wall or a curved wall structures (Giurgiutiu 2014).

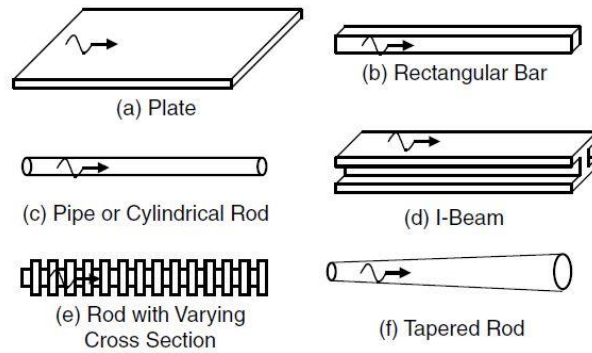


Figure 5.1 Different waveguides (Kundu, 2004).

The use of guided waves increased tremendously after 1990 for various reasons, especially because of improved analytic techniques. The principal benefits of guided waves can be summarized as follows.

1. Inspection over long distances from a single probe position is possible, giving complete volumetric coverage of the test object.
2. There is no need for scanning: all the data are acquired from a single probe position. Often, greater sensitivity than that obtained in conventional normal beam ultrasonic testing or other nondestructive techniques can be obtained, even with low frequency ultrasonic guided wave test techniques.

3. There is also an ability to inspect hidden structures, structures under water, coating, insulations and concrete because of the ability to test from a single probe position via wave structure change and controlled mode sensitivity along with an ability to propagate over long distances
4. There is also a tremendous cost effectiveness of the test simplicity and speed (ASNT, 2007).

5.2 RAYLEIGH WAVES

Elastic waves propagating along the surface were first predicted by John William Strutt (Lord Rayleigh) in 1885 because of his research on earthquakes and his identification of the rolling wave as the principal component of the energy waves that travel along the surface of the Earth. These waves are now being employed in a number of areas of science and technology, including ultrasonic NDE and SHM. Rayleigh waves, a.k.a. surface acoustic waves (SAW), propagate close to the body surface, with the motion amplitude decreasing rapidly with depth. The polarization of Rayleigh wave lies in a plane perpendicular to the surface. The effective depth of penetration is less than a wavelength. Rayleigh waves are found in solids that contain a free surface. The Rayleigh waves travel close to the free surface with very little penetration in the depth of the solid. For this reason, Rayleigh waves are also known as surface-guided waves (Rose 2014; Giurgiutiu 2014).

A Rayleigh wave propagates parallel to a free surface of an object at a unique speed, usually slightly slower than the shear wavespeed. The wavefront extends inward perpendicularly to the surface and can be planar, if excited by a line of force, or cylindrical, if excited by a point force. The motions combine compression and shear and

follow elliptical paths, decreasing exponentially with distance into the object, as illustrated in Fig. 31. The Rayleigh wave cannot exist on a liquid surface where there is no shear stiffness or Poisson effect (Lempriere, 2002).

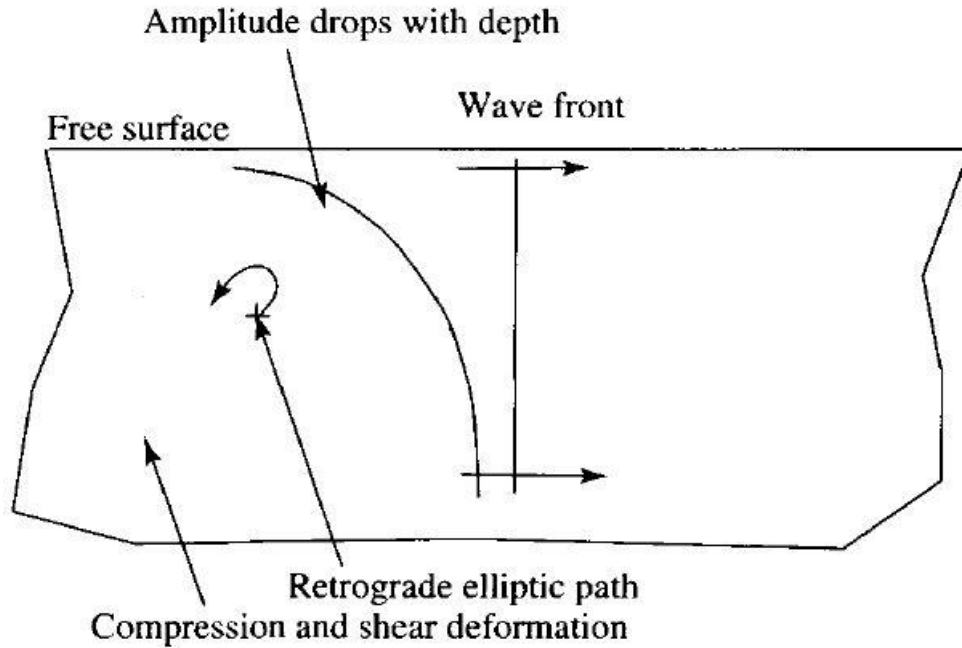


Figure 5.2: Schematic representation of motions in a Rayleigh surface wave (Lempriere, 2002).

Rayleigh waves are used for structural health monitoring because they are not dispersive, i.e. the wave speed is constant. It is found that the Rayleigh wave speed, c_R , depends on the shear wave speed, c_S , and the Poisson ratio, ν . A common approximation of the wave speed of Rayleigh wave is given as

$$c_R(\nu) = c_S \left(\frac{0.87 + 1.12\nu}{1 + \nu} \right) \quad (5.1)$$

For common Poisson ratio values, the Rayleigh wave speed takes values close to and just below the shear wave speed (Giurgiutiu 2014). The particle motion or the mode shape of the Rayleigh waves across the thickness direction, y , is given by

$$\begin{aligned}\hat{u}_x(y) &= Ai \left(\xi e^{-\alpha y} - \frac{\beta^2 + \xi^2}{2\xi} e^{-\beta y} \right) \\ \hat{u}_y(y) &= A \left(-\alpha e^{-\alpha y} + \frac{\beta^2 + \xi^2}{2\beta} e^{-\beta y} \right)\end{aligned}\quad (5.2)$$

where A is the wave amplitude factor, $\xi = \omega/c_R$ is the wavenumber of Rayleigh surface waves, α and β are coefficients given in Eq. (5.3) shows the Rayleigh wave in a semi-infinite medium.

$$\alpha^2 = \xi^2 \left(1 - \frac{c^2}{c_P^2} \right); \quad \beta^2 = \xi^2 \left(1 - \frac{c^2}{c_S^2} \right) \quad (5.3)$$

Rayleigh waves travel at a velocity of 117200 in. (297688 cm) per second in steel compared to the shear wave velocity of 128000 in. (325120 cm) per second. Thus, Rayleigh waves travel in steel at 91.6% the velocity of shear waves, or 8.4% less (UT classroom training book, ASNT 2007).

5.3 SHEAR HORIZONTAL PLATE WAVES

Shear horizontal (SH) plate waves have a shear-type particle motion contained in the horizontal plane. Figure 5.3 shows the coordinate definition and particle motion of SH plate waves. According to the coordinate defined, an SH wave has the particle motion along the z axis, whereas the wave propagation takes place along the x axis. The particle motion has only the u_z component. Unlike Rayleigh wave which is non-dispersive, SH plate waves are dispersive and may travel with different modes.

The phase velocity dispersion curve of the SH plate wave can be calculated as

$$c(\omega) = \frac{c_S}{\sqrt{1 - (\eta d)^2 \left(\frac{c_S}{\omega d} \right)^2}} \quad (5.4)$$

Where η is given in Eq. (5.5) and d is the half plate thickness.

$$\eta^2 = \frac{\omega^2}{c_s^2} - \frac{\omega^2}{c^2} \quad (5.5)$$

By substituting the appropriate eigenvalue, one gets an analytical expression for the wave-speed dispersion curve of each SH wave mode. For detailed expressions, the readers are referred to Giurgiutiu (2007).

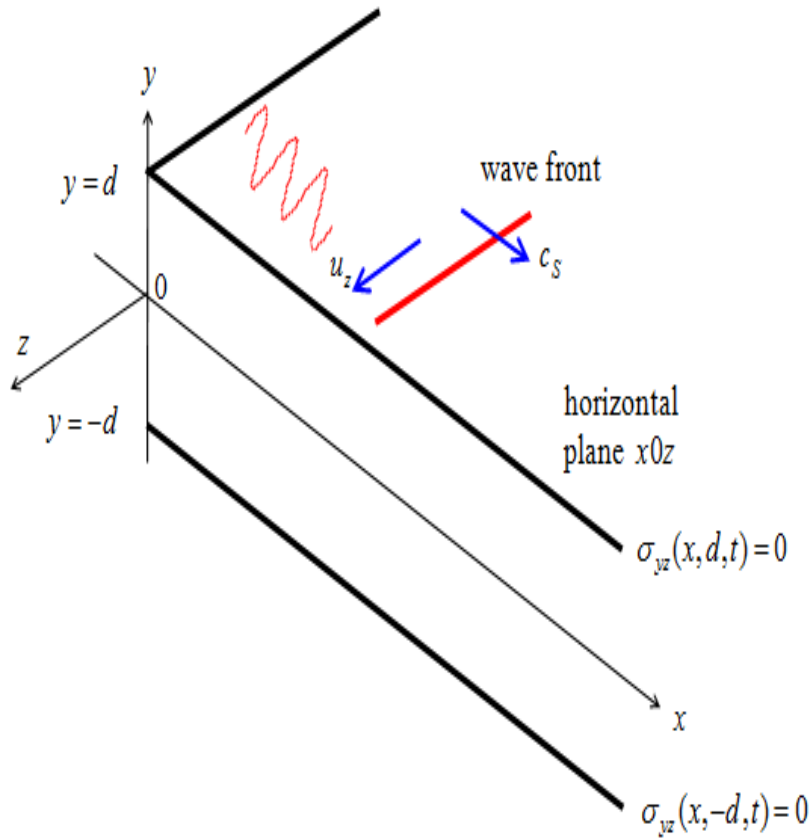


Figure 5.3: Coordinate definition and particle motion of SH plate waves (Giurgiutiu 2014).

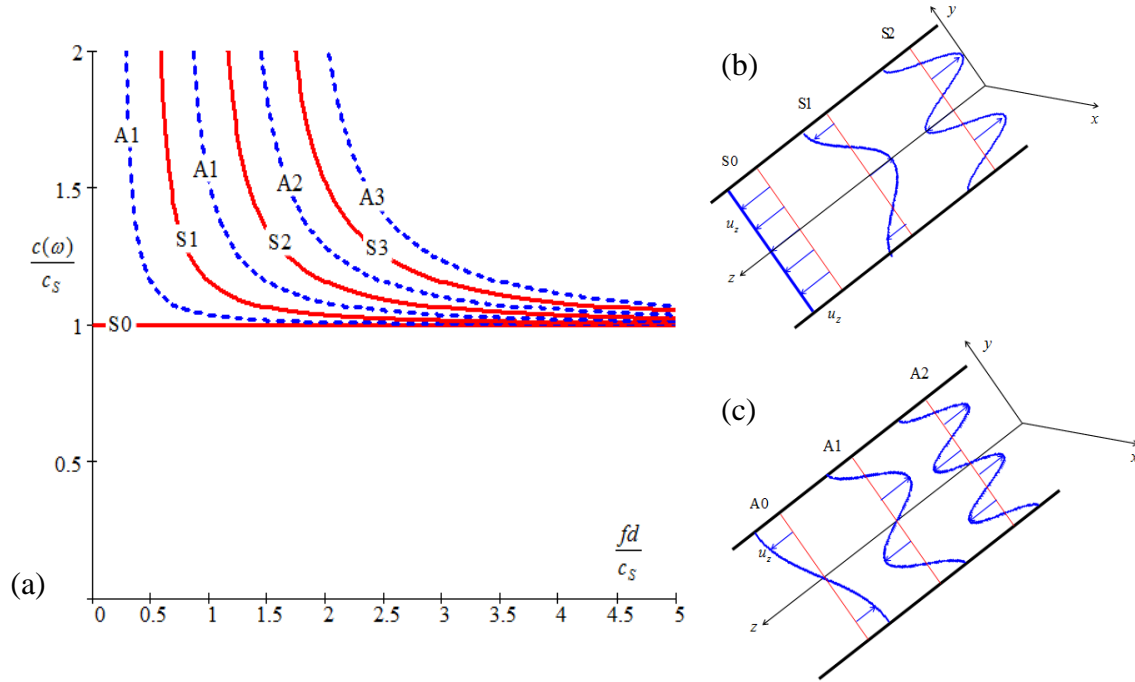


Figure 5.4: (a) SH plate wave-speed dispersion curves; (b) symmetric mode shapes; (c) antisymmetric mode shapes (Giurgiutiu 2014).

Figure 5.4 shows the wave-speed dispersion curve of SH plate waves and the mode shapes. It can be noticed that the fundamental symmetric mode (S0) wave is non-dispersive and always exists starting from low frequency-thickness product values. This nice property makes it a good candidate as the interrogating waves in SHM systems. Recently, considerable research has been carried out on the transmission and reception of SH plate wave for SHM (Kamal et al. 2013; Zhou et al. 2014). Higher wave modes only appear beyond the corresponding cut-off frequencies, showing dispersive characteristics, i.e., their phase velocity changes with frequency. For dispersive waves, group velocity is usually used to evaluate the propagation of wave packets. The definition of group velocity is given in Eq. (5.6).

$$c_g = \frac{d\omega}{d\xi} \quad (5.6)$$

5.4 LAMB WAVES

The theory of Lamb waves was originally developed by Horace Lamb in 1916 to describe the characteristics of waves propagation in plates. Frequently, they are also referred to as plate wave. Lamb waves can be generated in a plate with free boundaries with an infinite number of modes for both symmetric and antisymmetric displacements within the layer. The symmetric modes are also called longitudinal direction. The antisymmetric modes are observed to exhibit average displacement in the transverse direction and these modes are also called flexural modes. The infinite number of modes exists for a specific plate thickness and acoustic frequency which are identified by their respective phase velocities. The normal way to describe the propagation characteristics is by the use of dispersion curves based on the plate mode phase velocity as a function of the product of frequency times thickness. The dispersion curves are normally labeled as S0, A0, S1, A1 and so forth, depending on whether the mode is symmetric or antisymmetric. Although the dispersion diagrams are complex, they can be simplified by using the incident angle of the exciting wave to determine which mode is to be dominant. A particular Lamb wave can be excited if the phase velocity of the incident longitudinal wave is equal to phase velocity for the particular mode. Lamb waves are extremely useful for detection of cracks in thin sheet materials and tubular products (ASNT, 2007). There are two general types of Lamb (or plate) waves depending on the way the particles in material move as the wave moves along the plate. Both types are shown in Figure 5.5. Each type of Lamb wave has an infinite number of modes that the wave may attain. These modes are dependent on the three factors: the frequency of the waves, the angle of

incidence and the material. These modes are differentiated by the manner in which the particles in the material are moving.

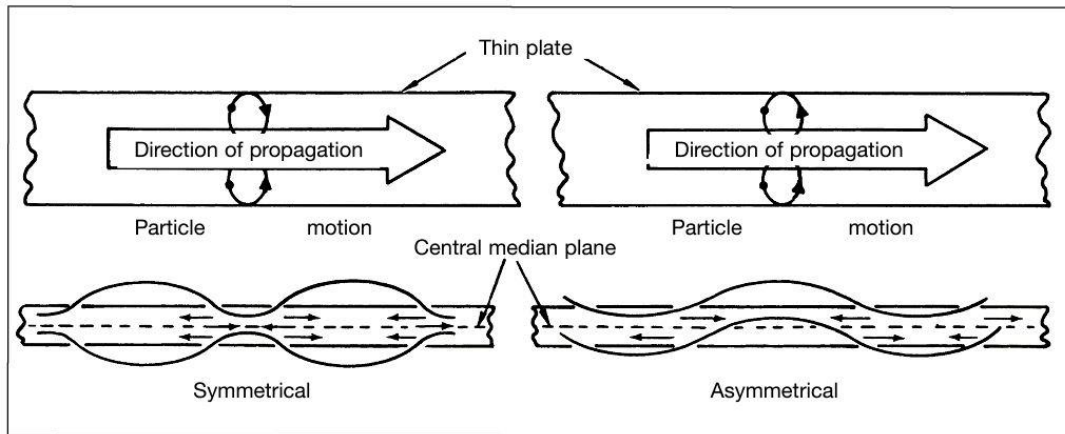


Figure 5.5 Symmetrical and asymmetrical Lamb waves: mode 1.

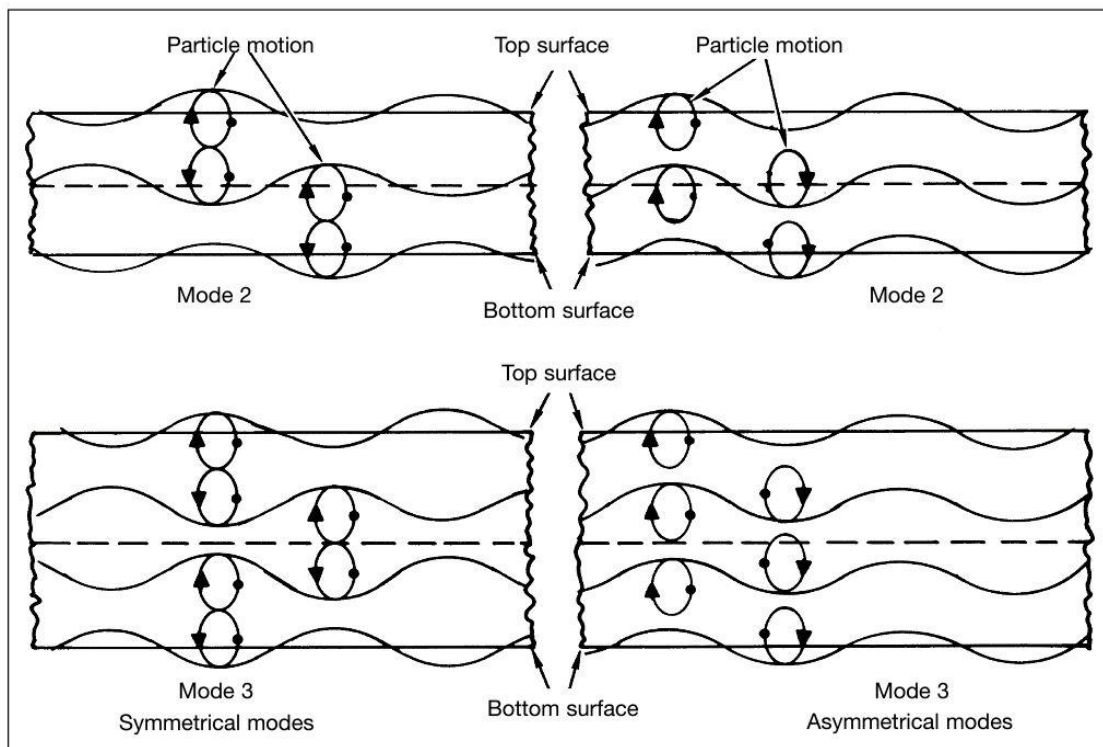


Figure 5.6 Lamb waves mode 2 and 3.

5.5 STRAIGHT CRESTED LAMB WAVES

Lamb waves are a type of ultrasonic waves that are guided between two parallel free surfaces, such as the upper and lower surfaces of a plate. Lamb waves can exist in two basic types, symmetric and antisymmetric. Figure 5.7 shows the particle motion of symmetric and antisymmetric Lamb waves. The Lamb wave motion has asymptotic behavior at low frequency and high frequency. At low frequency, the symmetric mode resembles axial waves, while the antisymmetric mode resembles flexural waves. At high frequency, both symmetric and antisymmetric wave approaches Rayleigh waves, because the particle motion is strong at the surfaces and decays rapidly across the thickness. The axial wave and flexural wave, by their nature, are only low frequency approximations of Lamb waves. The plate structure cannot sustain pure axial and flexural motion at large frequency-thickness product values.

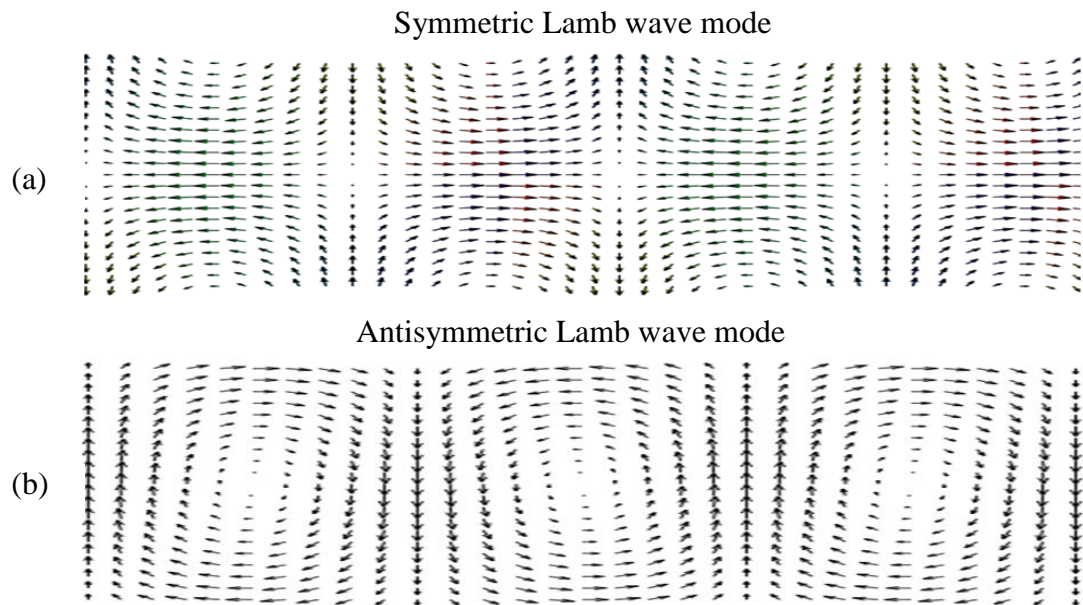


Figure 5.7: Particle motion of Lamb wave modes: (a) symmetric mode and (b) antisymmetric mode (Giurgiutiu, 2014).

The straight crested Lamb wave equations are derived under z-invariant assumptions using pressure wave and shear vertical wave (P+SV) waves in a plate. Through multiple reflections on the plate's lower and upper surfaces, and through constructive and destructive interference, the pressure waves and shear vertical waves give rise to the Lamb-waves, which consist of a pattern of standing waves in the thickness y -direction (Lamb-wave modes) behaving like traveling waves in the x -direction. For detailed derivation of Lamb wave equations, readers are referred to Graff (1991), Rose (1999), and Giurgiutiu (2007). The derivation finally reaches the Rayleigh-Lamb equation:

$$\frac{\tan \eta_s d}{\tan \eta_p d} = \left[\frac{-4\eta_p \eta_s \xi^2}{(\xi^2 - \eta_s^2)^2} \right]^{\pm 1} \quad (5.7)$$

Where +1 exponent corresponds to symmetric Lamb wave modes and -1 exponent corresponds to antisymmetric Lamb wave modes. d is the half plate thickness, and ξ is the frequency dependent wavenumber. η_p and η_s are given in Eq. (5.8). λ and μ are Lamé's constants of the material, and ρ is the material density.

$$\eta_p^2 = \frac{\omega^2}{c_p^2} - \xi^2; \quad \eta_s^2 = \frac{\omega^2}{c_s^2} - \xi^2; \quad c_p = \sqrt{\frac{\lambda + 2\mu}{\rho}}; \quad c_s = \sqrt{\frac{\mu}{\rho}}; \quad (5.8)$$

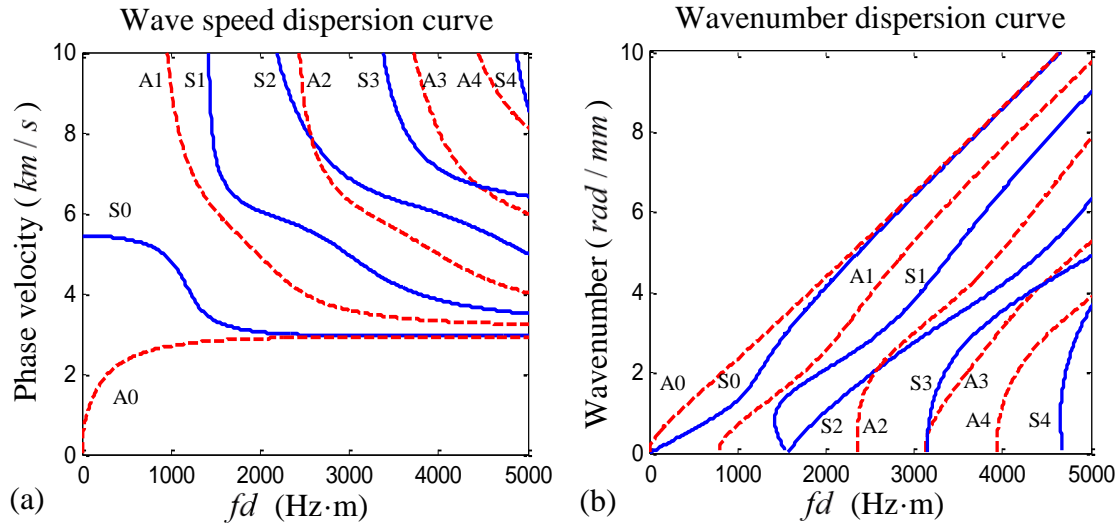


Figure 5.8 (a) Wave speed dispersion curve; (b) wavenumber dispersion curve.

Figure 5.8 shows the dispersion curves of aluminum plates calculated from the Rayleigh-Lamb equations. It can be noticed at least two wave modes (the fundamental symmetric mode: S0; the fundamental antisymmetric mode: A0) exist simultaneously. Beyond the corresponding cut-off frequencies, higher Lamb modes will participate in the propagation. At small frequency-thickness product values, the S0 mode is less dispersive than A0 mode, and all the Lamb wave modes converge to non-dispersive Rayleigh waves at large frequency-thickness product values. The dispersive and multi-mode nature of Lamb waves adds complexity in both Lamb wave propagation modeling and SHM application.

In their multi-modal and dispersive nature, Lamb waves also have complicated frequency dependent mode shapes associated with particle motion across the plate thickness. Even for certain Lamb modes, the mode shape changes under different frequencies. The displacement mode shapes can be calculated using Eq. (5.9) and Eq. (5.10) (Giurgiutiu 2014).

For symmetric Lamb modes:

$$\begin{aligned} u_x^S(x, y, t) &= iC^S \left[-2\xi^2 \eta_S \cos \eta_S d \cos \eta_P y + \eta_S (\xi^2 - \eta_S^2) \cos \eta_P d \cos \eta_S y \right] e^{i(\xi x - \omega t)} \\ u_y^S(x, y, t) &= C^S \left[2\xi \eta_P \eta_S \cos \eta_S d \sin \eta_P y + \xi (\xi^2 - \eta_S^2) \cos \eta_P d \sin \eta_S y \right] e^{i(\xi x - \omega t)} \end{aligned} \quad (5.9)$$

For antisymmetric Lamb modes:

$$\begin{aligned} u_x^A(x, y, t) &= iC^A \left[2\xi^2 \eta_S \sin \eta_S d \sin \eta_P y - \eta_S (\xi^2 - \eta_S^2) \sin \eta_P d \sin \eta_S y \right] e^{i(\xi x - \omega t)} \\ u_y^A(x, y, t) &= C^A \left[2\xi \eta_P \eta_S \sin \eta_S d \cos \eta_P y + \xi (\xi^2 - \eta_S^2) \sin \eta_P d \cos \eta_S y \right] e^{i(\xi x - \omega t)} \end{aligned} \quad (5.10)$$

Where C^S and C^A determine the mode shape amplitudes; y is the location of interested point across the plate thickness; i is the imaginary unit; x is the coordinate along propagation direction.

Figure 5.9 shows the mode shapes of fundamental S0 and A0 Lamb waves in a 2-mm aluminum plate under various frequencies. It can be observed that for certain Lamb mode, the mode shapes vary a lot with frequency. Within low frequency range, the mode shapes show that S0 and A0 Lamb modes could be approximated by axial and flexural wave motion. However, within high frequency range, the mode shapes become more complicated and deviate from the axial-flexural approximation. And, at even higher frequency, e.g. at 10 MHz, the particle motions are mainly near the top and bottom surfaces of the plate, while the particles in the middle of the plate undergo very small oscillation. This shows that at high frequency range, Lamb modes converge to Rayleigh waves.

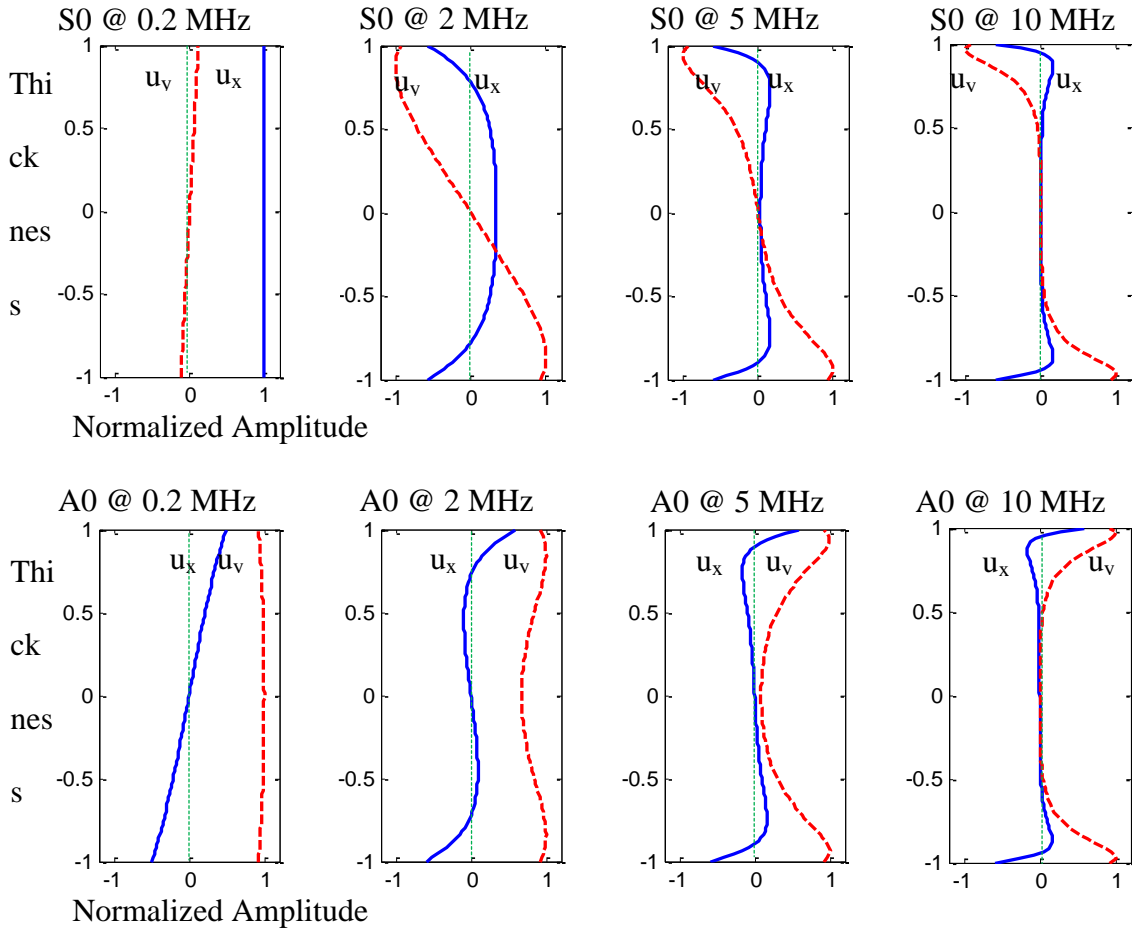


Figure 5.9: Mode shapes of S0 and A0 Lamb waves in a 2-mm thick aluminum plate (Shen, 2014).

5.6 CIRCULAR CRESTED LAMB WAVES

In their practical applications, the interrogating Lamb waves generated by a transmitter will propagate out in a circular crested wave front instead of a straight crested wave front, because the transmitter can be considered as a point source compared with the large inspection area. With the wave propagating outward, this amount energy is distributed on a larger area. Thus, the amplitude of the interrogating wave is strong near the wave source and decays along the propagation direction. The circular crested Lamb wave solution can capture these effects due to outward propagation pattern.

A detailed and rigorous derivation of circular crested Lamb waves is well documented in Giurgiutiu (2014). The derivation of circular crested Lamb waves is found to be more appropriate in a cylindrical coordinate system shown in Figure 5.10 a. The derivation arrives at the same Rayleigh-Lamb equation as Eq. (5.7) which means the circular crested Lamb waves propagate with the same wave speed as the straight crested Lamb waves.

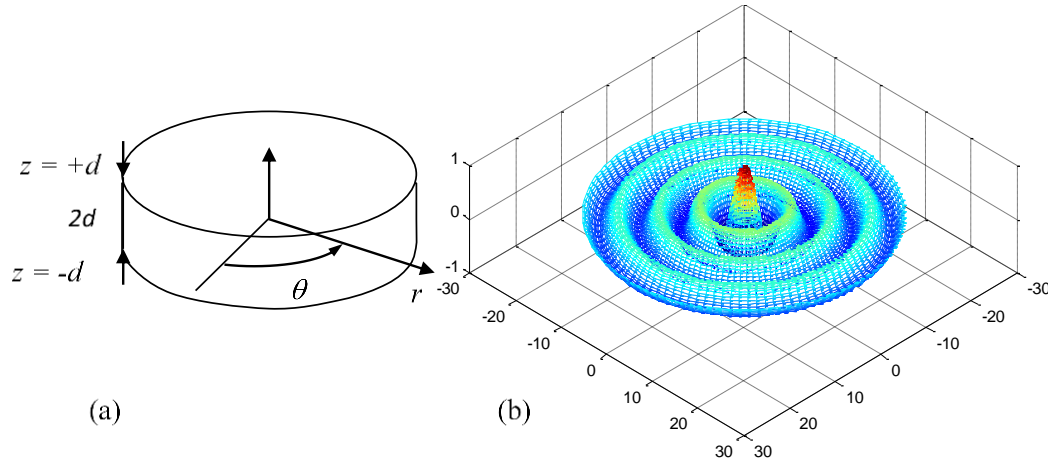


Figure 5.10 (a) Cylindrical coordinate for problem derivation (Giurgiutiu 2014);
 (b) Circular crested wave pattern (Shen, 2014).

The propagation pattern of circular Lamb waves admits the Bessel and Hankel function family solution. The Bessel functions J_0 and J_1 is appropriate for standing waves, and the Hankel functions $H_0^{(1)}$ and $H_1^{(1)}$ are appropriate for propagating waves. The first kind Hankel functions ($H_0^{(1)}$ and $H_1^{(1)}$) describes an outward propagating wave field, when $e^{-i\omega t}$ is chosen as the convention for the derivation. While, the second kind Hankel functions ($H_0^{(2)}$ and $H_1^{(2)}$) describes an outward propagating wave field, when $e^{i\omega t}$ is chosen as the convention for the derivation. The mode shape solutions for the circular crested Lamb waves are given below for outward propagating wave fields.

Symmetric Lamb modes:

$$\begin{aligned}
u_r^S(r, z, t) &= C^S \left[2\xi^2 \zeta_S \cos \zeta_S d \cos \zeta_P z - \zeta_S (\xi^2 - \zeta_S^2) \cos \zeta_P d \cos \zeta_S z \right] H_1^{(1)}(\xi r) e^{-i\omega t} \\
u_z^S(r, z, t) &= C^S \xi \left[2\zeta_P \zeta_S \cos \zeta_S d \sin \zeta_P z + (\xi^2 - \zeta_S^2) \cos \zeta_P d \sin \zeta_S z \right] H_0^{(1)}(\xi r) e^{-i\omega t}
\end{aligned} \tag{5.11}$$

Antisymmetric Lamb modes:

$$\begin{aligned}
u_r^A(r, z, t) &= -C^A \zeta_S \left[2\xi^2 \sin \zeta_S d \sin \zeta_P z - (\xi^2 - \zeta_S^2) \sin \zeta_P d \sin \zeta_S z \right] H_1^{(1)}(\xi r) e^{-i\omega t} \\
u_z^A(r, z, t) &= C^A \xi \left[2\zeta_P \zeta_S \sin \zeta_S d \cos \zeta_P z + (\xi^2 - \zeta_S^2) \sin \zeta_P d \cos \zeta_S z \right] H_0^{(1)}(\xi r) e^{-i\omega t}
\end{aligned} \tag{5.12}$$

where C^S and C^A are the amplitude factor for symmetric mode and antisymmetric mode, and can be determined from the wave generation calculation. ζ_P, ζ_S are defined as

$$\zeta_P^2 = \frac{\omega^2}{c_P^2} - \xi^2; \quad \zeta_S^2 = \frac{\omega^2}{c_S^2} - \xi^2 \tag{5.13}$$

It can be observed from Eq. (5.11) and Eq. (5.12), that the in-plane radian direction motion accepts the solution of the first kind Hankel function of order one ($H_1^{(1)}$), while the out-of-plane direction motion accepts the solution of the first kind Hankel function of order zero ($H_0^{(1)}$). shows a typical outward propagation wave pattern calculated using Hankel function $H_0^{(1)}$, describing an out-of-plane wave motion. It can be noticed that the wave amplitude at the wave source (coordinate center) is strong, and it decays as it propagates out. Figure 5.11 shows the plots of Hankel functions of order zero and order one. It can be noticed that the amplitude is high near the origin of R , and beyond certain distance, the amplitude becomes stable and changes more gradually compared with the origin range of R .

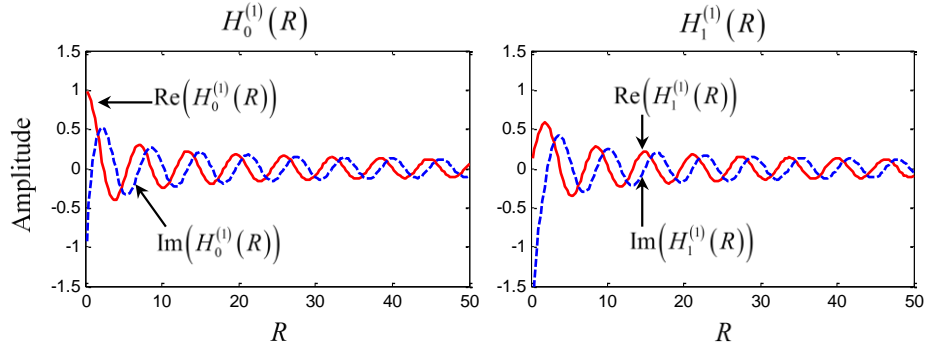


Figure 5.11 Hankel function of order zero ($H_0^{(1)}(R)$) and order one ($H_1^{(1)}(R)$) (Shen, 2014).

5.7 STRUCTURAL HEALTH MONITORING USING GUIDED WAVES

Structural Health Monitoring (SHM) is an emerging multi-disciplinary field with wide applications. This technology evolves from the conventional nondestructive evaluation (NDE) and conditional based maintenance (CBM), where the damage detection and evaluation are done in a schedule based or conditional based manner. In contrast with NDE and CBM, SHM aims at developing real-time or on-demand damage detection and characterization systems for evaluation of structural health status. Within the scope of SHM, guided wave techniques are favorable for their capability of interrogating large areas of structure from a single location. In this section, fundamental SHM concepts are introduced, prevalent guided wave techniques are covered, and key points in guided wave based SHM are discussed.

5.7.1 STRUCTURAL HEALTH MONITORING CONCEPTS

General sensing technology can be cast into two methodological categories: (1) passive sensing and (2) active sensing. Passive sensing systems only passively record events which happened during an interested period of time. By analyzing the recorded signal, diagnosis can be made on the health status of the structure. Examples of passive

sensing SHM can be found in the acoustic emission (AE) monitoring and impact detection, where passive sensors are triggered by crack advancing or impact events. By analyzing the AE or impact signal, location of the AE or impact source can be identified (Yu et al 2012; Gresil et al. 2013). In contrast to passive sensing, active sensing methods interrogate the structures with defined excitations, and record the corresponding response. By analyzing the response, diagnosis can be made. Active sensing procedure has three main advantages for SHM applications: (1) it allows the real-time and on-demand inspection of the structures; (2) the excitation can be optimized for the most sensitive and effective response for damage detection; (3) the active sensing procedure is repeatable, which allows the comparison between two independent interrogations (a baseline data and a current status data).

SHM is a pattern recognition process. SHM techniques aim at finding deviations of sensing signals or data pattern from the baseline, which are due to the presence of damage.

5.7.2 GUIDED WAVE TECHNIQUES

The guided wave techniques can be generally categorized into linear techniques and nonlinear techniques. Many of the interrogating principles stem from conventional NDE. The linear techniques include pitch-catch, pulse-echo, electro-mechanical impedance spectroscopy (EMIS), phased array, and sparse array time-reversal imaging method. The prevalent nonlinear techniques are higher harmonic generation, subharmonic generation, and mixed frequency response (nonlinear modulation).

Figure 5.12 shows the pitch-catch active sensing method in SHM, where one transducer acts as the transmitter and sends out the guided waves, and another transducer acts as the receiver and pick up the sensing signal. In the pristine case (baseline), the interrogating waves are generated by the transmitter, propagate along the structure, and are picked up by the receiver. In the damaged case, the interrogating waves generated by the transmitter, propagate along the structure, interact with the damage, carry the damage information with them, and are finally picked up by the receiver. The subtraction between these two states reveals the damage scattering response, which may indicate the presence and severity of the damage.

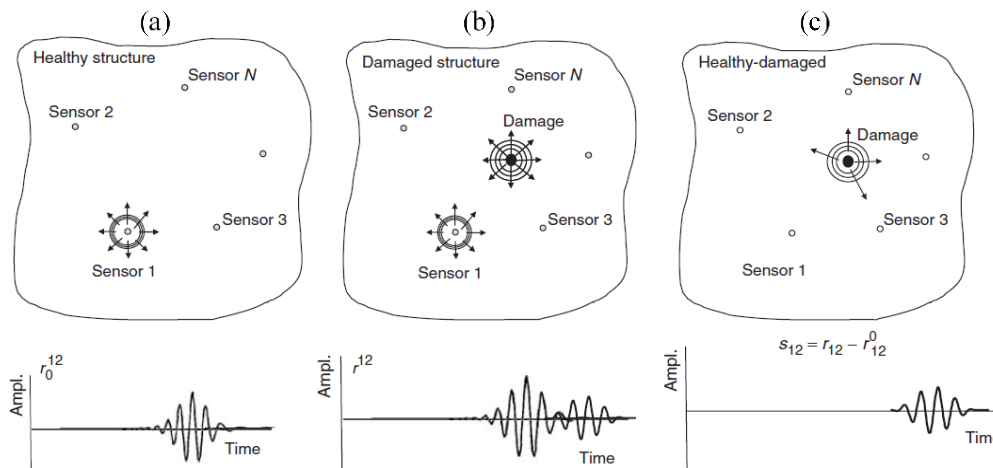


Figure 5.12 Pitch-catch active sensing: (a) baseline response; (b) response with damage; (c) scattered response. (Ihn and Chang 2008)

Several sensors may work together in a systematically designed manner forming a sensor network and achieve more complicated diagnostic approaches. Advanced damage imaging techniques have been developed using phased array and sparse array. Giurgiutiu and Bao (2004) investigated the embedded-ultrasonic structural radar (EUSR) for in situ monitoring of thin-wall structures. Figure 5.13a shows the 1-D phased array EUSR and

its imaging result of a crack. Yu and Giurgiutiu (2007) further extended the EUSR principle to 2-D phased array using 64 sensors. Based on Fink's work (1992), Wang et al. (2004) proposed the synthetic time-reversal imaging method for structural health monitoring. Figure 5.13b shows the sparse array with four sensors and its imaging result using time-reversal method.

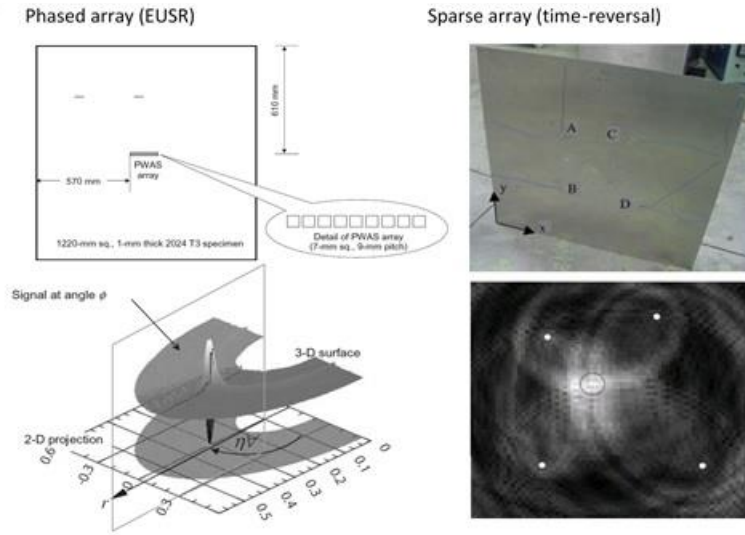


Figure 5.13 (a) Phased array imaging using EUSR (Giurgiutiu and Bao 2004); (b) sparse array imaging using time-reversal method (Wang et al. 2004).

In addition to traveling wave techniques, the EMIS is a standing guided wave SHM method. The continuous harmonic excitation of a transducer will excite the structure with guided waves, which will be reflected by structural boundaries and damage, forming standing waves between the wave source and the reflectors. This standing wave formation will result in local mechanical resonance, which will be shown in the electrical response through the electro-mechanical coupling. Figure 5.14a shows the electro-mechanical coupling between the transducer and the structure. Figure 5.14b is a typical EMIS spectrum, showing that the damaged case spectrum deviates from the pristine case.

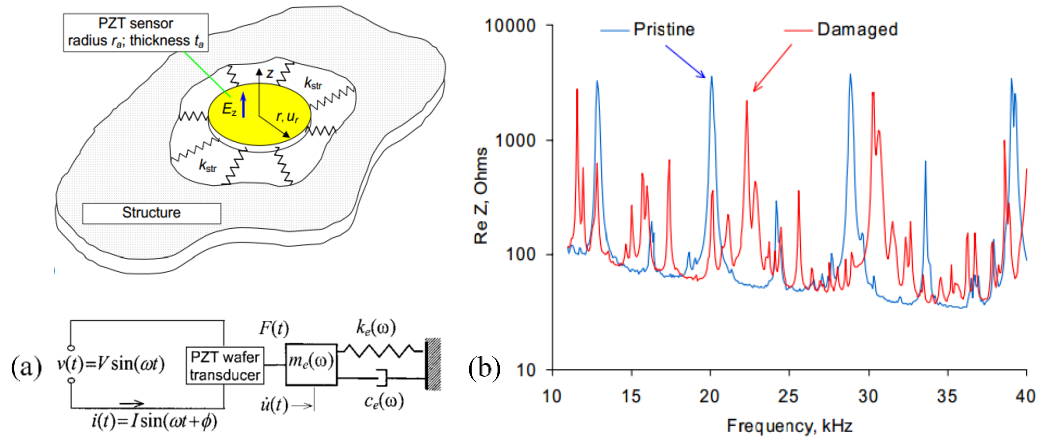


Figure 5.14 (a) Electro-mechanical coupling between the PZT active sensor and the structure (Giurgiutiu et al. 1999); (b) EMIS spectrum (Zagrai and Giurgiutiu 2001).

5.8 PIEZOELECTRIC WAFER ACTIVE SENSORS

Piezoelectric wafer active sensors (PWAS) are convenient enablers for generating and receiving guided waves. Figure 5.15 shows the comparison between the conventional ultrasonic transducer and PWAS.

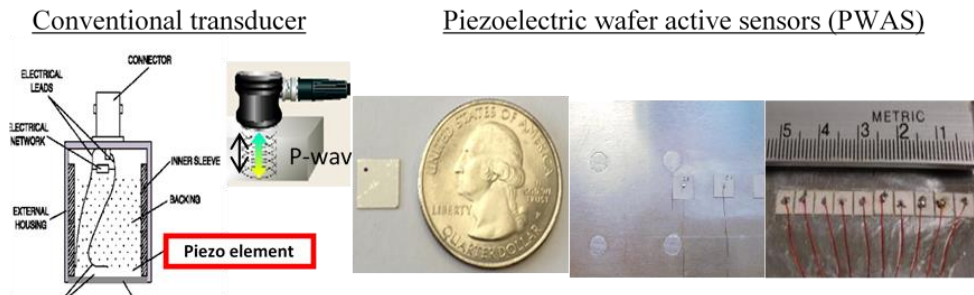


Figure 5.15 Comparison between conventional ultrasonic transducer and PWAS.

The conventional ultrasonic transducers are bulky, expensive, and can only generate through thickness pressure wave in the structures, which cannot satisfy the need for inspection of large areas. Compared with conventional transducers, PWAS are low

profile, light weight, low cost, and unobtrusive to structures. They can be permanently bonded on host structures in large quantities and achieve real-time monitoring of the structural health status. They couple with the structure through in-plane motion and generate Lamb waves, which makes them suitable for inspection large areas of interest.

5.8.1 PWAS PRINCIPLES AND OPERATION MODES

Piezoelectric wafer active sensors (PWAS) couple the electrical and mechanical effects (mechanical strain, S_{ij} , mechanical stress, T_{kl} , electrical field, E_k , and electrical displacement, D_j) through the tensorial piezoelectric constitutive equations

$$\begin{aligned} S_{ij} &= s_{ijkl}^E T_{kl} + d_{kij} E_k \\ D_j &= d_{klj} T_{kl} + \varepsilon_{jk}^T E_k \end{aligned} \quad 5.14$$

Where s_{ijkl}^E is the mechanical compliance of the material measured at zero electric field ($E = 0$), ε_{jk}^T is the dielectric permittivity measured at zero mechanical stress ($T = 0$), and d_{klj} represents the piezoelectric coupling effect. PWAS utilize the d_{31} coupling between in-plane strains, S_1, S_2 and transverse electric field E_3 .

PWAS transducers can be used as both transmitters and receivers. Their modes of operation are shown figure 5.16. PWAS can serve several purposes (Giurgiutiu 2014): (a) high-bandwidth strain sensors; (b) high-bandwidth wave exciters and receivers; (c) resonators; (d) embedded modal sensors with the electromechanical (E/M) impedance method. By application types, PWAS transducers can be used for (i) active sensing of far-field damage using pulse-echo, pitch-catch, and phased-array methods, (ii) active sensing of near field damage using high-frequency E/M impedance method and thickness gage

mode, and (iii) passive sensing of damage-generating events through detection of low-velocity impacts and acoustic emission at the tip of advancing cracks (figure 5.16). The main advantage of PWAS over conventional ultrasonic probes is in their lightweight, low profile, and low cost. In spite of their small size, PWAS are able to replicate many of the functions performed by conventional ultrasonic probes.

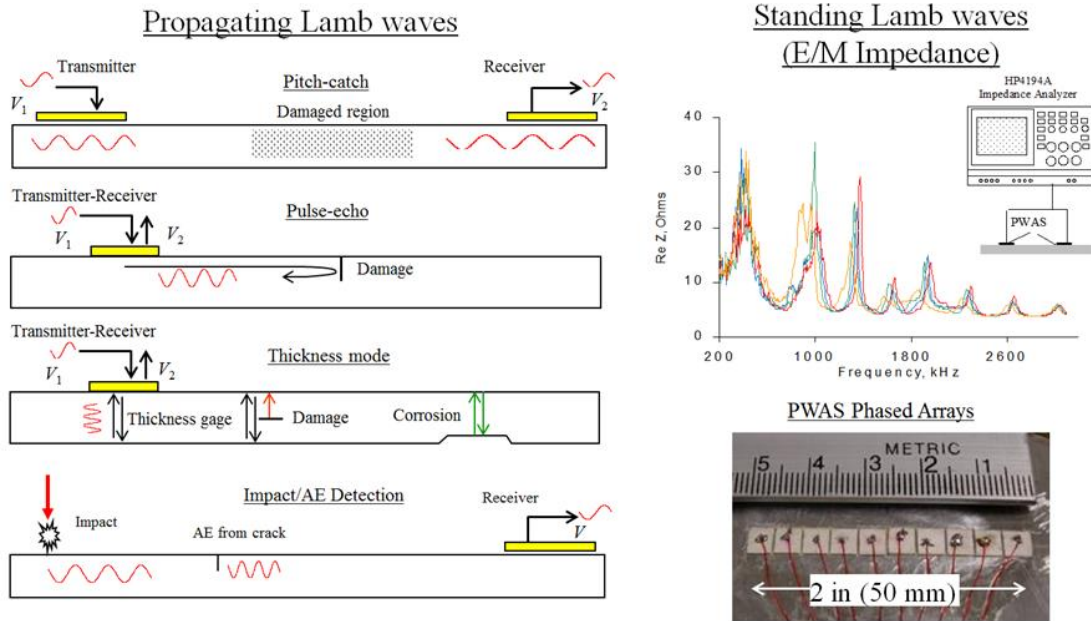


Figure 5.16 Schematic of PWAS application modes (Giurgiutiu 2010).

5.8.2 PWAS COUPLED GUIDED WAVES AND TUNING EFFECT

Figure 5.17 shows the coupling between PWAS and the host structure, and illustrates how PWAS transducers generate Lamb waves. When an oscillatory electric voltage at ultrasonic frequencies is applied on PWAS, due to the piezoelectric effect, an oscillatory strain is induced to the transducer. Since the structure constrains the motion of PWAS, the reacting force from the bonding layer will act as shear stress on the host structure and generate wave motion.

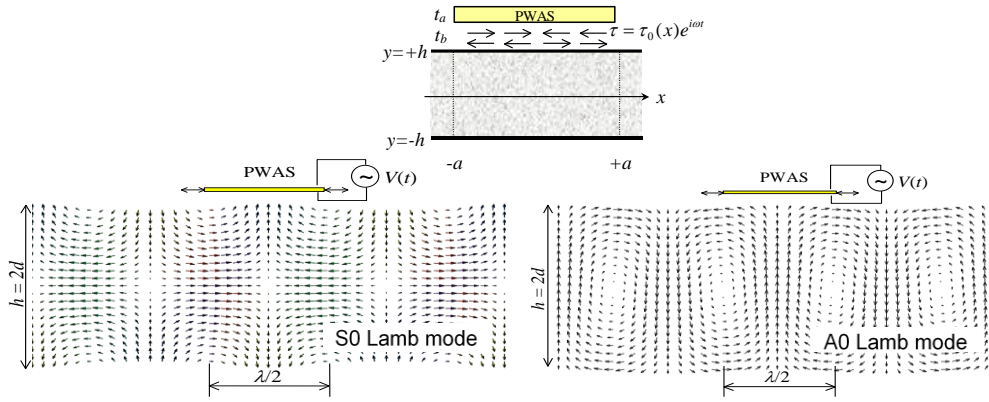


Figure 5.17 Lamb wave generation using PWAS (Giurgiutiu 2014).

The Lamb wave amplitude excited by PWAS depends on the PWAS size, plate thickness, and excitation frequency. For a given PWAS and plate geometry, the amplitudes of Lamb modes changes with frequency. It was found that tuning possibility exists for generating single Lamb mode with PWAS transducers. The tuning effect is important because it overcomes the multimode difficulty for Lamb wave applications. The analytical expression on tuning effect was first developed by Giurgiutiu (2003)

$$\varepsilon_x(x, t) = -i \frac{a\tau_0}{\mu} \left\{ \sum_{\xi^S} (\sin \xi^S a) \frac{N_S(\xi^S)}{D_S(\xi^S)} e^{-i(\xi^S x - \omega t)} + \sum_{\xi^A} (\sin \xi^A a) \frac{N_A(\xi^A)}{D_A(\xi^A)} e^{-i(\xi^A x - \omega t)} \right\} \quad 5.15$$

Figure 5.18 shows the tuning curve for 7 mm PWAS and 1.6 mm thick aluminum plate situation. It is apparent that the amplitudes of S0 and A0 Lamb modes excited by the PWAS transducer change with frequency. Around 300 kHz, A0 Lamb mode reaches the rejecting point where no A0 mode Lamb wave will be excited. This is a sweet spot for generating only S0 wave mode for structural inspection.

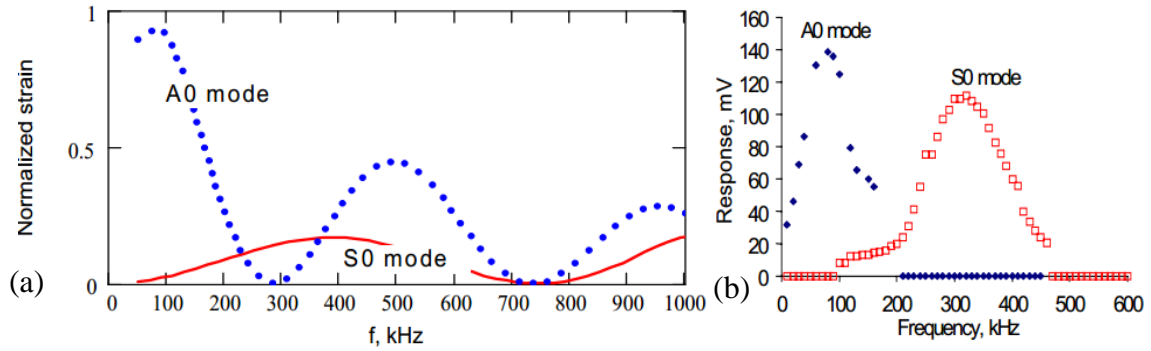


Figure 5.18 (a) Strain Lamb wave tuning results from analytical solution; (b) Experimental results from PWAS response (Giurgiutiu 2003).

5.9 DAMAGE DETECTION USING GUIDED WAVES

Damage is defined as changes to the material and/or geometric properties of these systems, including changes to the boundary conditions and system connectivity. Damage affects the current or future performance of these systems.

The damage identification process is generally structured into the following levels:

1. Damage detection, where the presence of damage is identified
2. Damage location, where the location of the damage is determined
3. Damage identification, where the type of damage is determined
4. Damage extent, where the severity of damage is assessed (Wenzel, 2009)

Two types of defect and their effects on wave propagation are illustrated in Figure 5.19. An internal crack produces an early echo (a reflection) with less attenuation (i.e., a stronger signal) than that from the back face of an object. Low-density material attenuates and slows a wave so that it arrives late and with reduced amplitude (Lempriere, 2002).

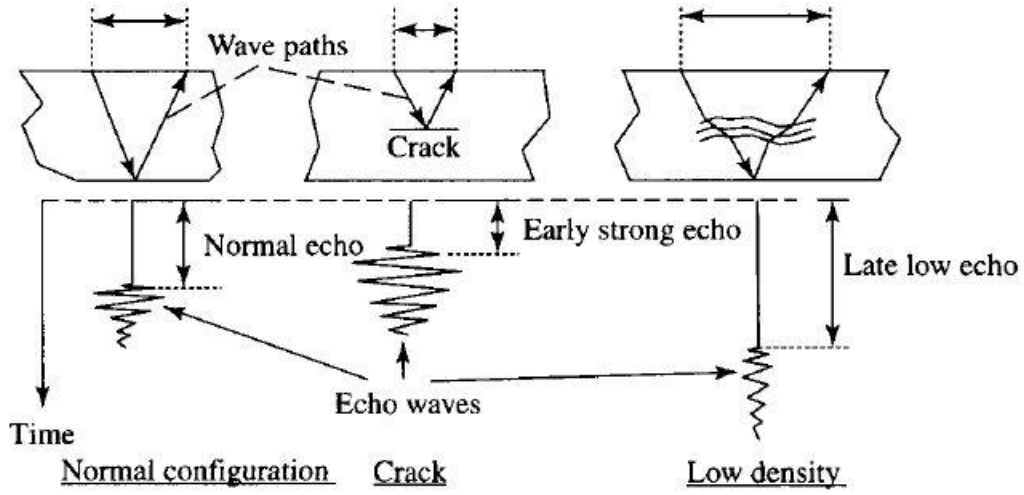


Figure 5.19 The effects of two types of defect (Lemproere, 2002).

CHAPTER 6

WELDED JOINTS WITH REALISTIC DEFECTS

The weld defects and discontinuities are in general undesirable from the point of view of the industrial uses of the welded materials. But for purposes of proper training and qualification of NDT personnel it is necessary to have the test specimens with known flaws. Development of NDT techniques and validation of NDT procedures for their performance and reliability are not done on simple calibration blocks or real defects. Calibration blocks (Figure 6.1) with very simple artificial discontinuities, such as side drilled holes (SDH), flat bottom holes (FBH), and electro discharge machining (EDM) notches are used to perform demonstration NDT techniques and set equipment and recording levels. Real defects (Figure 6.2) in a structure present only particular cases and does not provide the inspector with a performant technique for the whole of the damage considered for detection. Thus, the realistic defects (Figure 6.3) are crucial and important for development of NDT field and to improve the level of their accuracy of defects detection and characterization assessment. Therefore, there is a need to pay greater attention to this subject.



Figure 6.1 Real crack



Figure 6.2 NDT calibration blocks. Olympus-ims.com



Figure 6.3 Realistic defects kit

This chapter will discuss the methods of fabrication of welding defects because the welding being the most popular industrial sector and crack being the most severe defect (Crutzen et al., 1998; ENIQ report No 44, 2011).

6.1 STATE-OF-THE-ART

A significant amount of research has been carried out aimed at developing the techniques for manufacturing of test pieces for NDT development and qualification. Virkkunen et al. (2009). developed defect manufacturing technology based on controlled thermal fatigue which are called True Flaw. Ngon and Toan (2015) produced longitudinal welding crack with residual stress using cast iron electrodes. The crack is produced by combining two welding technique, shielded metal arc welding (SMAW) and gas tungsten arc welding (GTAW). da Silva (*Institute Superior Tecnico*) developed welding procedure to produce specimens with artificial defects for NDT training and personal certification. Srivastava et al. (2013) were used welding and heat treatment processes to produce surface cracks that detectable by liquid penetrant test and magnetic particle test.

6.2 REPRESENTATIVENESS OF FLAWS

This means, the used artificial or realistic defects give similar response in the used NDT than real flaw. (Kemppainen & Virkkunen, 2011) discussed three approaches (real, artificial, and realistic flaws representativeness):

First, the flaw is produced by the same damage mechanism that is postulated to be active in service is not recommended for representativeness of flaws. The postulated damage

mechanism of a real defect presents only particular case and it is not always possible to produce a flaw to relevant components.

Second, is to directly compare NDT response acquired from artificial flaws and service induced flaws. This approach is not recommended for the following drawbacks:

1. The result becomes overly linked to the used NDT method. If the method is developed or changed, the response may change and the comparison must be re-done every time.
2. The representative service-induced cracks are not generally available. If representative service induced flaws of known size were available, artificial flaws would not be needed.
3. Service-induced flaws, as any natural phenomena, exhibit wide range of variance in their characteristics.

Third, the recommended approach is to use metallographic crack characteristics as the basis for representativeness.

6.3 METHODS OF FABRICATION OF REALISTIC WELDING DEFECTS

There are four methods to obtain realistic weld flaws:

1. Implanted defects: where a pre-existing defect is attached to the test piece. The attachment usually takes the form of a weld in a machined recess.
2. Weld doping or weld modification: where for instance crack prone material is added to a weld to promote localized weld cracking. Other examples include introduction of porosity or slag.

3. Machined defects: where a defect can consist of a cut or machined void. Electro Discharge Machining (EDM) is perhaps the most relied upon technology in this area where a shaped electrode is used to erode the test piece. The process is most suitable for production of surface defects, although it is possible to use it in combination with welding to produce buried defects.
4. Grown defects: where cracking is initiated and propagated into test pieces in much the same way as would occur in a plant, simply accelerated to make fabrication times practical. The main processes used for this class of defect are thermal fatigue and stress corrosion cracking.

These four methods are documented and used in the most fabrication of realistic defects as shown in the state of the art of this chapter. The above description of these methods is quoted by Virkkunen et al. (2009) from an ENIQ report work, but that ENIQ document was never published in the form referred to in their paper.

It is acceptable to produce flaws using any process from the four methods, providing the resulting flaw is distinguishable by its NDT characteristics. NDT results are dependable upon the specific type of flaw in the test specimen. Therefore, locating the flaw is dependent upon its position and type in the test specimen along with its characteristics.

The following are the characteristics of crack as example of defect characteristics:

1. Location and orientation of the crack,
2. Size of the crack,
3. Opening of the crack through the whole path and at crack tip,
4. Fracture surface roughness,
5. Filling of the crack with some substance (e.g., water or oxide).

NDT methods should be used to evaluate the characteristics or existence of realistic flaws (IAEA, 2001; ENIQ report No 42)

6.4 NONDESTRUCTIVE EVALUATION OF WELDING

First, let discuss the deference between testing and evaluation.

Test something means to check, to determining the presence quality, a basis for evaluation or judgment, or a hard-external covering; testing the acting of test. While, evaluation means judgment (Longman dictionary). So, the Nondestructive evaluation (NDE) based on NDT method employed, NDT personnel, procedures, and equipment. The NDE is judged by comparing the acquired inspection result with known state of the sample. The reliability of non-destructive evaluation depends on multitude of different factors. These range from physical aspects of the used technology (e.g., wavelength of ultrasound) to application issues (e.g. probe coupling or scanning coverage) and human factors (e.g. inspector training and stress or time pressure during inspection). Due to this complexity, the only practical way to asses inspection reliability and to confirm that the inspection procedure functions as intended is by using practical trials as shown in the flow chart Figure 6.4 (IAEA, 200; Kemppainen & Virkkunen, 2011; API 1104; ASME section V).

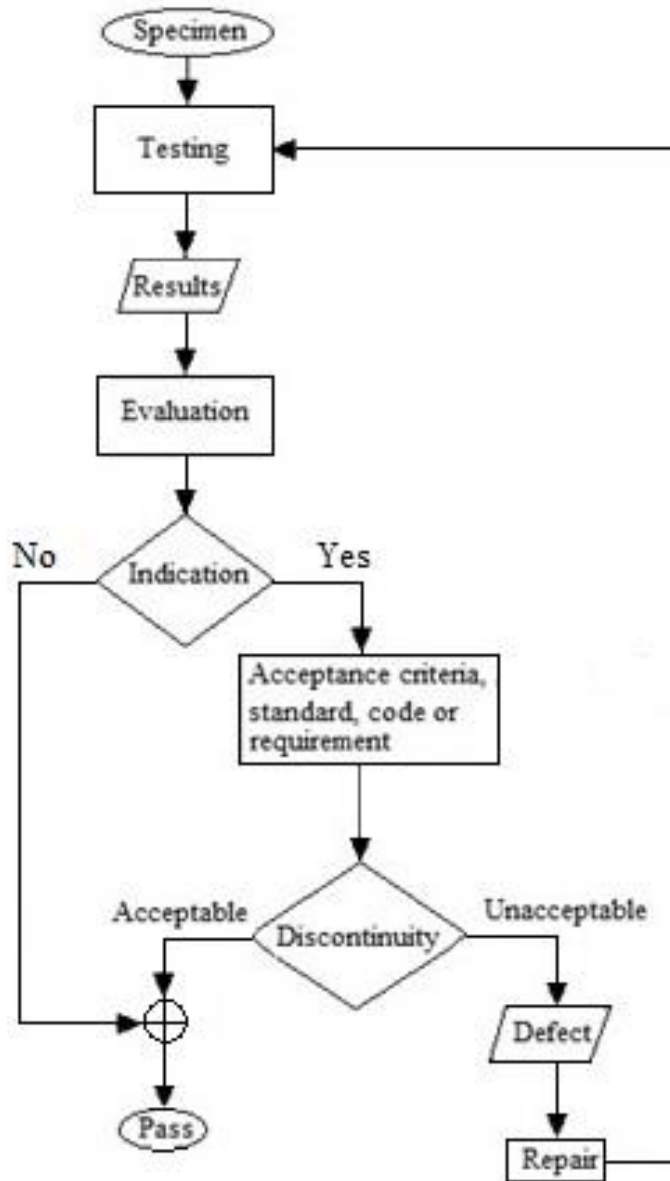


Figure 6.4 Flow chart of welding NDE

For this chapter, the flow chart of welding NDE is modified to produce realistic defects as shown in Figure 6.5

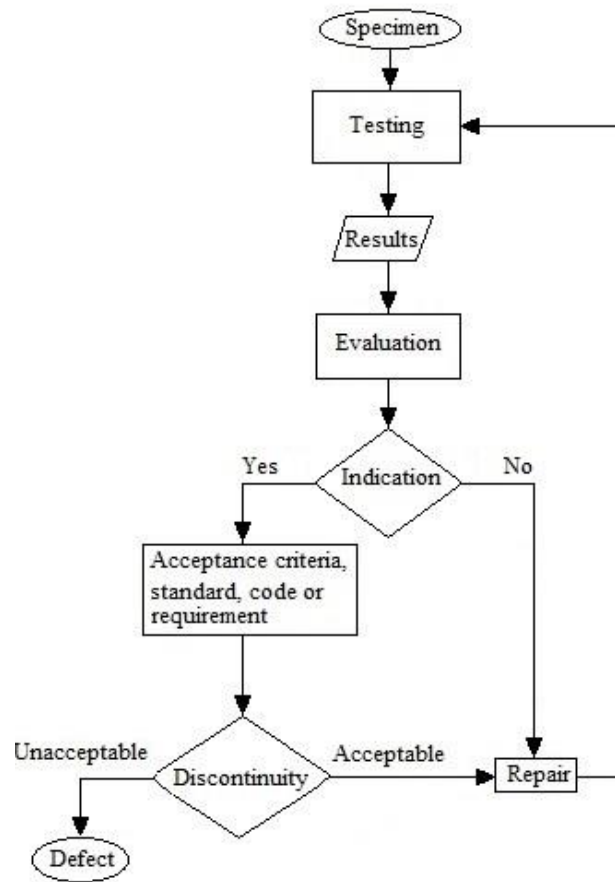


Figure 6.5 Flow chart of realistic welding defects

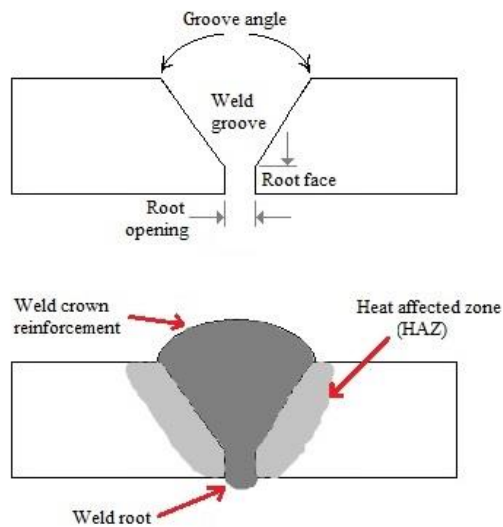


Figure 6.6 Weld terminology

6.5 EXPERIMENT SET-UP #1

Initially austenitic stainless steel plate type 304 of 7"×6"×0.5", Figure 6.7, is bought from the welder training and testing institute and fabricated at the machine shop of USC, Figure 6.8. This specimen is fabricated per ASME IX, procedure qualification record (PQR), as per the parameters given in below:

Joint design: Single-V-groove

Joint type; Butt joint

Groove angle: 60°

Root opening: 0.125"

Root face: 0.125"

Welding process: GTAW

Type of welding process: Manual

Filler metal: ER 308/308L

Filler Metal size: 0.125"

Deposit thickness: 0.5"

Maximum pass thickness: 0.125"

Position of groove: 1G (the test plates are placed in a horizontal plane and the weld metal deposited from the upper side).

Shielding gas: Argon

Welding technique: Stringer and weave

Multiple passes

Initial/inter-pass cleaning: Brushing.

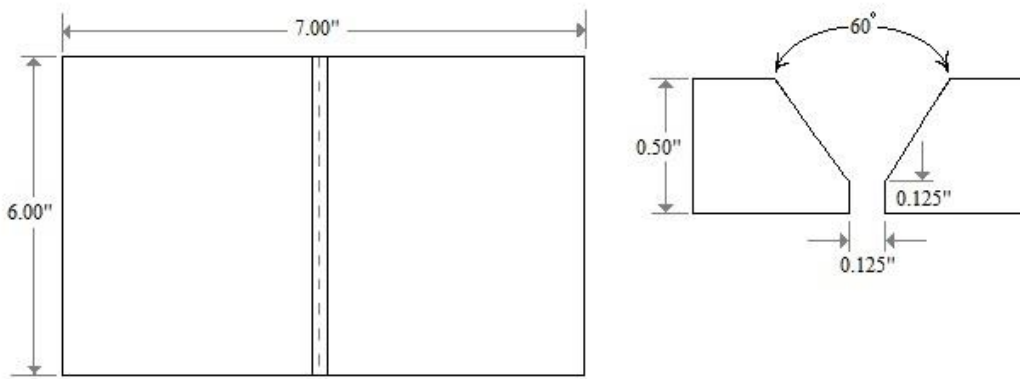


Figure 6.7 Set-up of 0.50" thick austenitic SS 304 plate

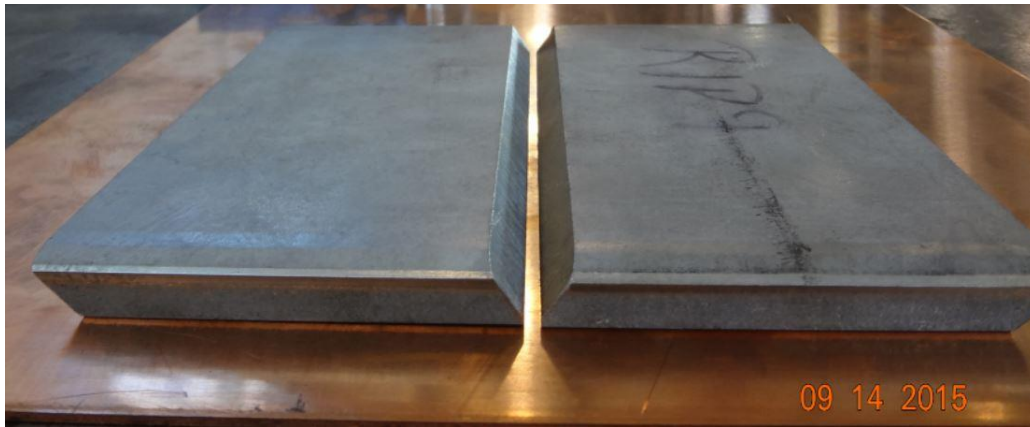


Figure 6.8 Specimen #1 configuration

In this part of experiment, the second method of fabrication a realistic defect is used. This method based on weld modification which is used to produce porosities, tungsten inclusion, slag inclusion, and lack of root penetration.

First, incomplete root penetration, in butt welding, a root opening is usually left at the bottom of the groove (in one side welding) or at the center of the weld (in two side welding). If the opening between the two plates is narrow, it is difficult to achieve

complete penetration and fusion at the root of the weld. Therefore, a lack of fusion in the root of the weld left by the failure of the weld metal to fill the root of a butt weld. It is caused by the electrode held at an incorrect angle, an electrode too large in diameter, a rate of travel too fast, an insufficient welding current, or an improper joint preparation (e.g. joint misalignment). In this experiment, it is done by fix copper plate to the opening root area as shown in Figure 6.9.and Figure 6.10.



Figure 6.9 copper plate is used to get lack of root penetration



Figure 6.10 Back side of the plate which shows lack of root penetration

Second, porosities, Figure 6.11, are created by interrupting or removing the arc shield during welding, such as creating a long arc. Figure shows the porosities in the filling pass.



Figure 6.11 Welding porosities

Third, tungsten inclusions are particles of metallic tungsten embedded in the weld metal which originate from the tungsten electrode used in tungsten arc welding. Causes are excessive welding current allowing the melting and deposition of tungsten in the weld and incorrect polarity of electrode using a DC source. Tungsten inclusions can also be caused by dipping the electrode into the molten weld metal or by touching the filler rod to the electrode during welding. Figure 6.12 shows tungsten inclusion in filling pass which is done by dipping the electrode into the molten weld metal.



Figure 6.12 Tungsten inclusion

6.6 RESULTS AND DISCUSSION OF SET-UP #1

NDT method, RT, is applied to the fabricated plate. This test is conducted by Applied Technical Service company (ATS) to confirm the procedure of manufacturing realistic defects. PAUT is not applied to this plate because of the limitation of its dimensions.

Radiographic inspection or testing (RT) is a non-destructive inspection method based on using short wavelength electromagnetic radiation passing through the material, Figure 6.13. Materials with areas of reduced thickness or lower material density allow more, and therefore absorb less, radiation. The radiation, which reaches the film after passing through the material, forms a shadow image on a photographic film (radiograph).

Areas of low absorption (slag, porosity) appear as dark areas on the developed film (radiograph). Areas of high absorption (dense inclusions) appear as light areas on the

developed film. Lower energy radiation can be in the form of either gamma or X-rays. X-rays are produced when electrons, travelling at high speed, collide with matter. The conversion of electrical energy to X radiation is achieved in an evacuated tube. A low current (mA) is passed through a filament to produce electrons. Application of a high potential (kV) voltage between the filament and a target accelerates electrons across this voltage differential. The action of an electron stream striking the target produces X rays; these are produced only while voltage is applied to the X ray tube. Whether using gamma or X ray sources, the test object, e.g. weld, is not radioactive following the inspection

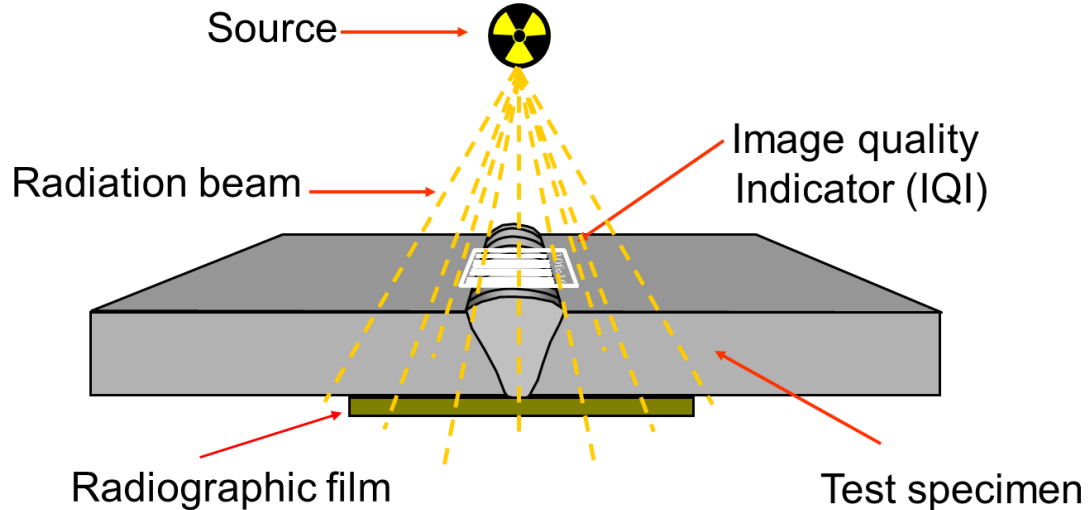


Figure 6.13 Set-up of radiographic testing method (RT)

Image quality indicator (IQI), Figure 6.14, an object that known in form and size placed on the specimen so that its image appears on the film, wire type from ASMT (International Association for Testing Materials) is used. It is used because there are so many variables in a radiographic technique to judge whether a radiograph has been obtained.

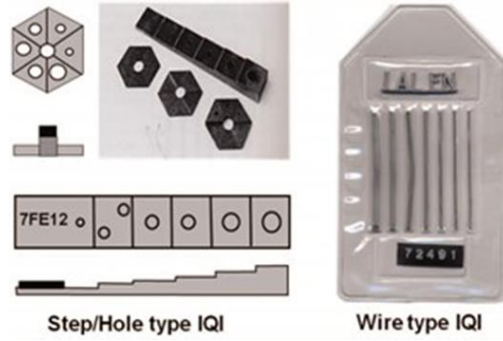


Figure 6.14 Image Quality Indicators. Adopted from The Welding Institute (TWI)

The Figure 6.15 shows that RT result of porosities, incomplete root penetration, and tungsten inclusion, are achieved successfully.

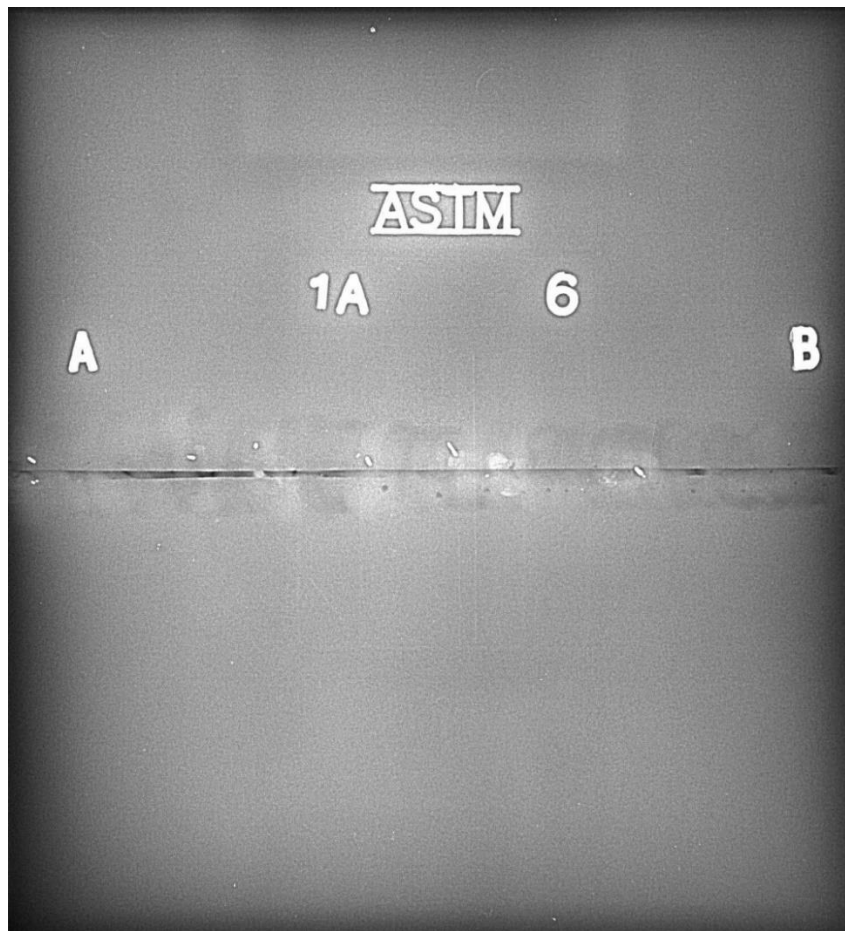


Figure 6.15 RT of 0.50" thick austenitic SS 304 plate

6.7 EXPERIMENT SET-UP #2

Austenitic stainless steel plate type 304 of 20"×15"×0.25" is bought from Metal supermarkets and fabricated at Flaw Tech. This specimen is fabricated per ASME IX procedure qualification record (PQR) with modification to produce two types of cracks in weld (longitudinal and transverse crack) as illustrated in figures Figure 6.16 and Figure 6.17. These cracks are manufactured by *proprietary method*.

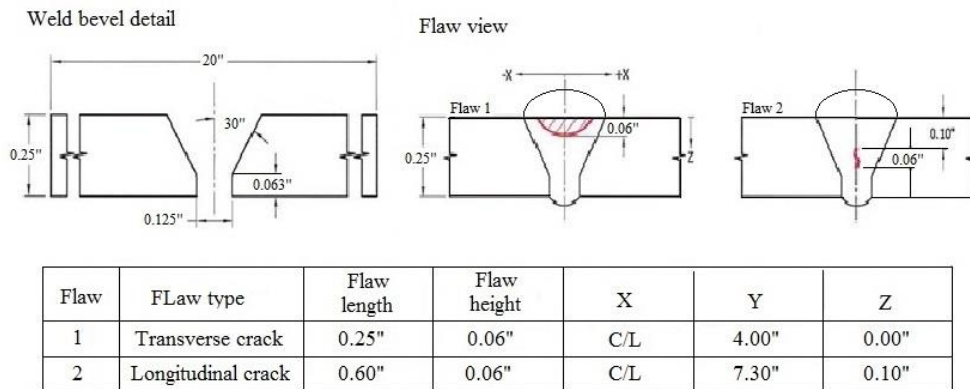


Figure 6.16 Weld bevel detail

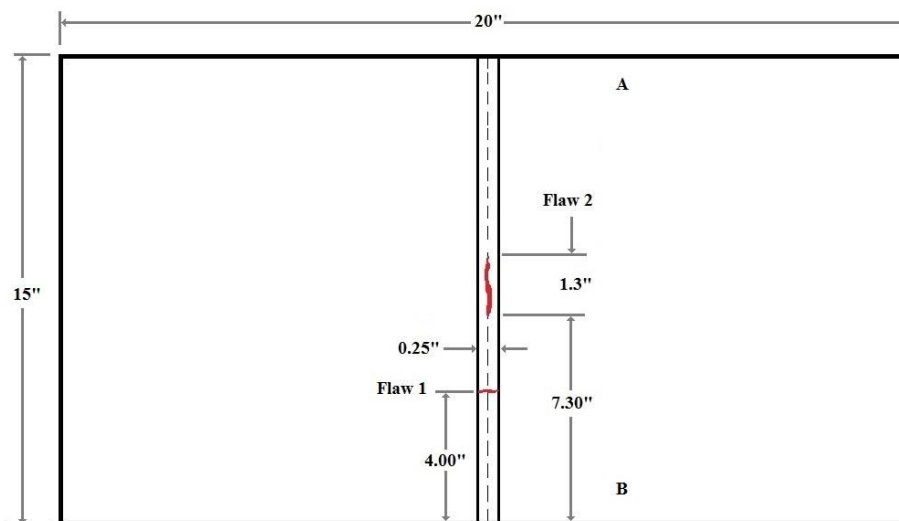


Figure 6.17 Set-up of 0.25" thick austenitic SS 304 plate

It is important to describe the cracks and their types. Cracks are fractures or ruptures of the weld metal occurring when the stress in a localized area exceeds the weld metal's ultimate tensile strength as shown Figure 6.18.

1. Hot cracks occur as tears while the weld metal is in the plastic condition whereas cold cracks and delayed cracks occur after the weld metal has cooled.
2. Delayed cracks are cold cracks that may occur hours after the weldment has cooled. There are several crack types associated with weldments.
3. Longitudinal crack is oriented along the length or approximately parallel to the longitudinal axis, of the weld.
4. Transverse crack is approximately perpendicular to the longitudinal axis of the weld.
5. Under bead crack forms in the heat affected zone and are usually short but may also be an extensive network.
6. Toe crack. begins at the toe of the weld and propagate along the plane of highest stress.
7. Root crack. is longitudinal crack located in the root pass.
8. Crater crack. is usually star shaped patterns that occur in the crater (ASNT, 2002).

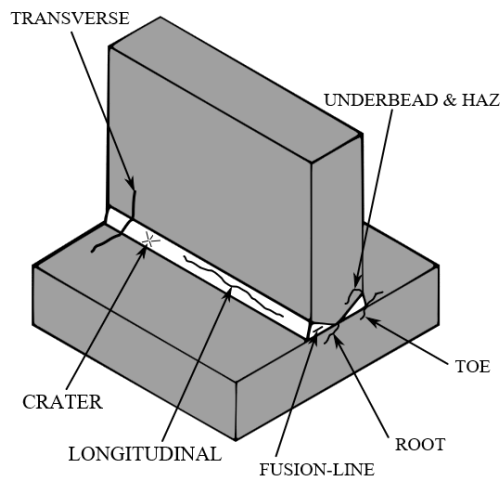


Figure 6.18 Welding cracks. Adopted from wikimedia.org

The following important types of hot cracks can be identified in the connection with the welding of austenitic stainless steels. The cracks differ in respect of their time and place of origin. They are:

1. Solidification cracks in the weld metal
2. Liquation cracks in the heat affected zone (HAZ)
 - a. of the base metal
 - b. of the weld metal in multilayer welds

Solidification cracks occur during solidification of the liquid weld metal, when liquid-i.e. low melting phases remain between the primary, mainly dendritic crystals. Liquation cracks are produced by the enrichment of liquid, low melting phases at the grain boundaries of the crystals formed near the HAZ of a weld bead or, to be more precise, in the high temperature zone which borders immediately upon the liquid weld metal but has not yet been fully fused. This type of crack can be found in both the HAZ of the base

metal and the heat affected zones of previously deposited weld metal beneath newly deposited weld beads(Folkhard et al., 1988).

6.8 RESULTS AND DISCUSSION OF SET-UP #2

NDT methods, RT and PAUT, are applied to the fabricated plate. RT is conducted by Applied Technical Service company (ATS) and PAUT is carried out at LAMSS.

In RT, X-ray source Varian type NDI-320-26 as shown in figure is used to generate X-ray.as shown in Figures Figure 6.19 and Figure 6.20.



Figure 6.19 NDT-RT-X-ray source details

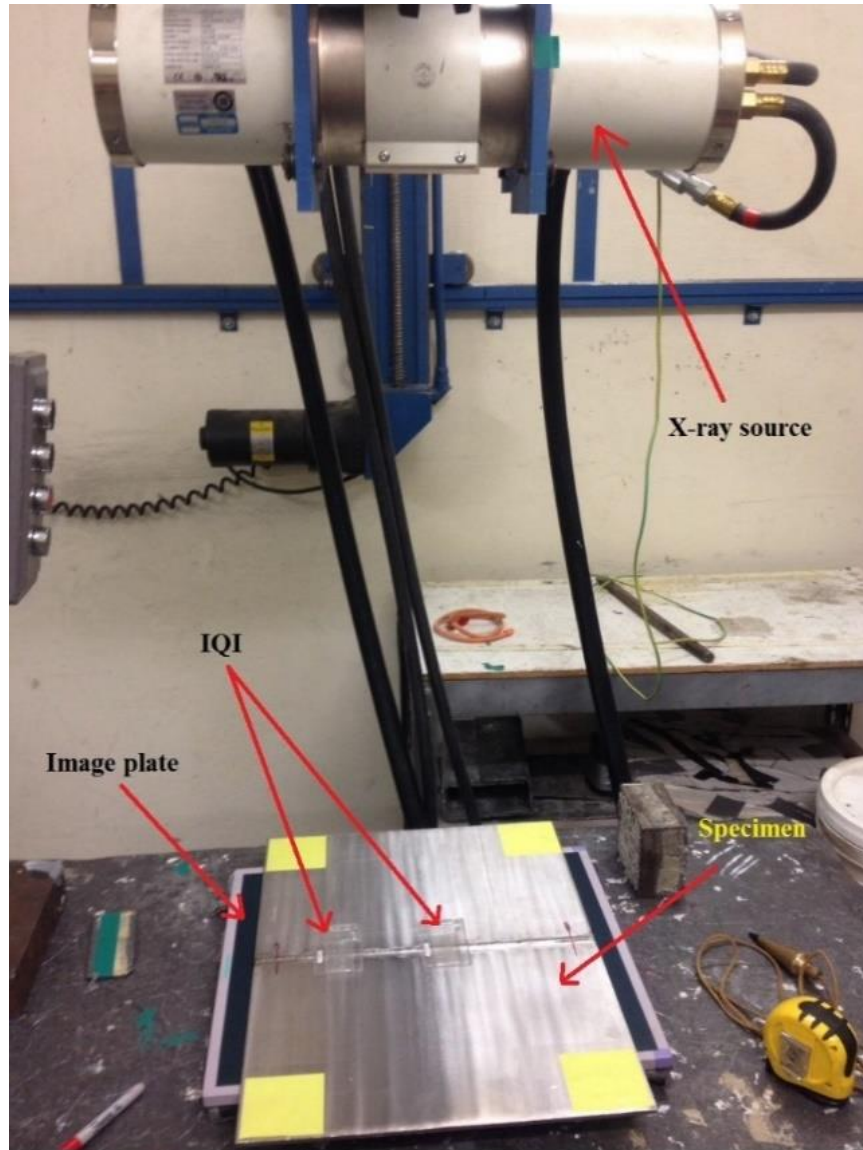


Figure 6.20 RT Set-Up for specimen#2

The following RT film, Figure 6.21, shows obviously the longitudinal and transverse cracks in welded area.

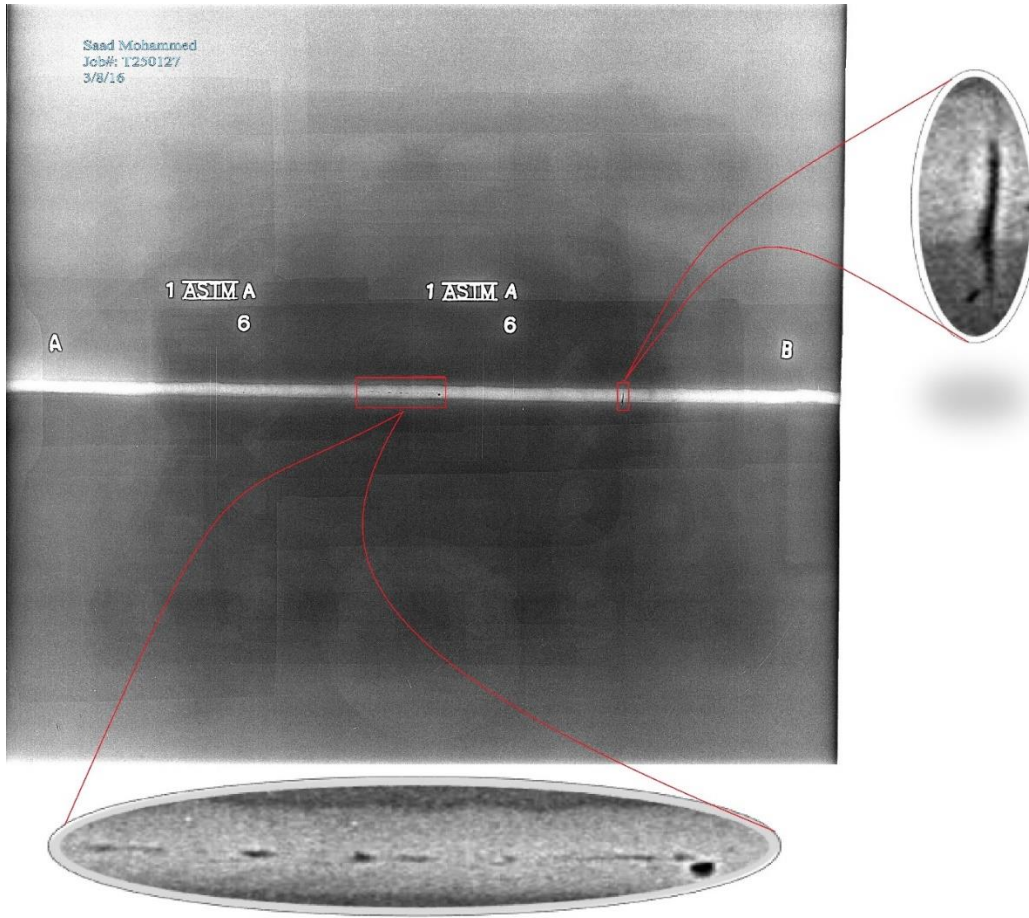


Figure 6.21 RT of SS 304 plate #2 with close-up view of two cracks

The coarse, dendritic grain structure of the weld material, formed during the welding process, is extreme and unpredictably anisotropic. Such structure is no longer direction-independent to the ultrasonic wave propagation; therefore, the ultrasonic beam deflects and redirects and the wave front becomes distorted. Thus, the use of conventional ultrasonic testing techniques using fixed beam angles is very limited and the application of ultrasonic Phased Array techniques becomes desirable (Pudovikov et al., 2008).

PAUT is conducted at LAMSS using OMNISX-PA 1664PR as shown in Figure 6.22.



Figure 6.22 .Olympus-omniscan sx. Adopted from (olympus-ims.com)

PAUT probe type 5L64-38.4X10-A12-P-2.5-OM, Figure 6.23, is attached to the PAUT instrument.

PAUT probe details are: Standard Phased Array Probe, 5 MHz linear array, 64 elements, 38.4x10 mm total active aperture, 0.60 mm pitch, 10 mm elevation, A12 case type, 2.5 m cable length, omniscan connector.



Figure 6.23 Standard PA probe. Adopted from (olympus-ims.com)

Also, Standard wedge for angle beam phased-array probe A12, normal scan, 55-degree shear wave, plain wedge as illustrated in Figure 6.24 is connected to the PAUT probe.



Figure 6.24 Standard wedge for angle PA probe. Adopted from (olympus-ims.com)

The following report shows the parameters of PAUT to detect flaw #1 (transverse crack).

Report Date	Report Version	File Name	Inspection Date	Inspection Version	Save Mode
2016 / 10 / 04	MXU- 4.1R14	longitudinal.ops	2016 / 10 / 04	MXU- 4.1R14	Report
OmniScan Type	OmniScan Serial #	Module Type	Module Serial #	Data File Name	
OmniScan SX	QC-001704	OMNISX-PA1664PR	QC-001704	flaw1	

Setup					
A:40.00 Sk:090 L:001					
Beam Delay	Start (Half Path)	Range (Half Path)	PRF	Type	Averaging Factor
20.0 μ s	0.000 in	3.289 in	60	PA	1
Scale Type	Scale Factor	Video Filter	Rectification	Filter	
Compression	9	On	FW	None (1.0 - 17.8 MHz)	
Voltage	Gain	Mode	Wave Type	Sound Velocity	Pulse Width
40 (Low)	40.00 dB	PE (Pulse-Echo)	Shear	0.122 in./ μ s	100.00 ns
Scan Offset	Index Offset	Skew			
0.000 in	1.127 in	90.0°			
Gate	Start	Width	Threshold	Synchro.	Peak Selection
A	0.350 in	0.200 in	24.00 %	Pulse	Max Peak

Calculator					
Element Qty. Used	First Element	Last Element	Resolution	Wave Type	Material Velocity
16	1	16	1.0	Shear	0.122 in./ μ s
Start Angle	Stop Angle	Angle Resolution	Focal Depth	Law Configuration	
40.00°	70.00°	1.00°	1.968 in	Sectorial	

Part		
Material	Geometry	Thickness
STEEL, STNLS	Plate	0.500 in

Scan Area					
Scan Start	Scan Length	Scan Resolution	Synchro.	Scan Speed	
0.000 in	3.937 in	0.039 in	Time	2.362 in/s	
Axis	Encoder	Encoder Type	Encoder Resolution	Polarity	
Scan	Off	Off	Off	Off	

Also, the following report shows the parameters of PAUT to detect flaw #2 (longitudinal crack).

Report Date	Report Version	File Name	Inspection Date	Inspection Version	Save Mode
2016 / 10 / 04	MXU- 4.1R14	Unnamed	2016 / 10 / 04	MXU- 4.1R14	Inspection Data
OmniScan Type	OmniScan Serial #	Module Type	Module Serial #	Data File Name	
OmniScan SX	QC-001704	OMNISX-PA1664PR	QC-001704	sand20161004	

Setup

A:40.00 Sk:270 L:001					
Beam Delay	Start (Half Path)	Range (Half Path)	PRF	Type	Averaging Factor
20.0 μ s	0.000 in	3.289 in	60	PA	1
Scale Type	Scale Factor	Video Filter	Rectification	Filter	
Compression	9	On	FW	None (1.0 - 17.8 MHz)	
Voltage	Gain	Mode	Wave Type	Sound Velocity	Pulse Width
40 (Low)	45.00 dB	PE (Pulse-Echo)	Shear	0.122 in/ μ s	100.00 ns
Scan Offset	Index Offset	Skew			
0.000 in	0.748 in	270.0°			
Gate	Start	Width	Threshold	Synchro.	Peak Selection
A	1.100 in	0.502 in	23.00 %	Pulse	Max Peak

Calculator

Element Qty. Used	First Element	Last Element	Resolution	Wave Type	Material Velocity
16	1	16	1.0	Shear	0.122 in/ μ s
Start Angle	Stop Angle	Angle Resolution	Focal Depth	Law Configuration	
40.00°	70.00°	1.00°	1.968 in	Sectorial	

Part

Material	Geometry	Thickness
STEEL, STNLS	Plate	0.500 in

Scan Area

Scan Start	Scan Length	Scan Resolution	Synchro.	Scan Speed
0.000 in	3.937 in	0.039 in	Time	2.362 in/s
Axis	Encoder	Encoder Type	Encoder Resolution	Polarity
Scan	Off	Off	Off	Off

Figure 6.25 shows the location of transverse crack in the welded plate.

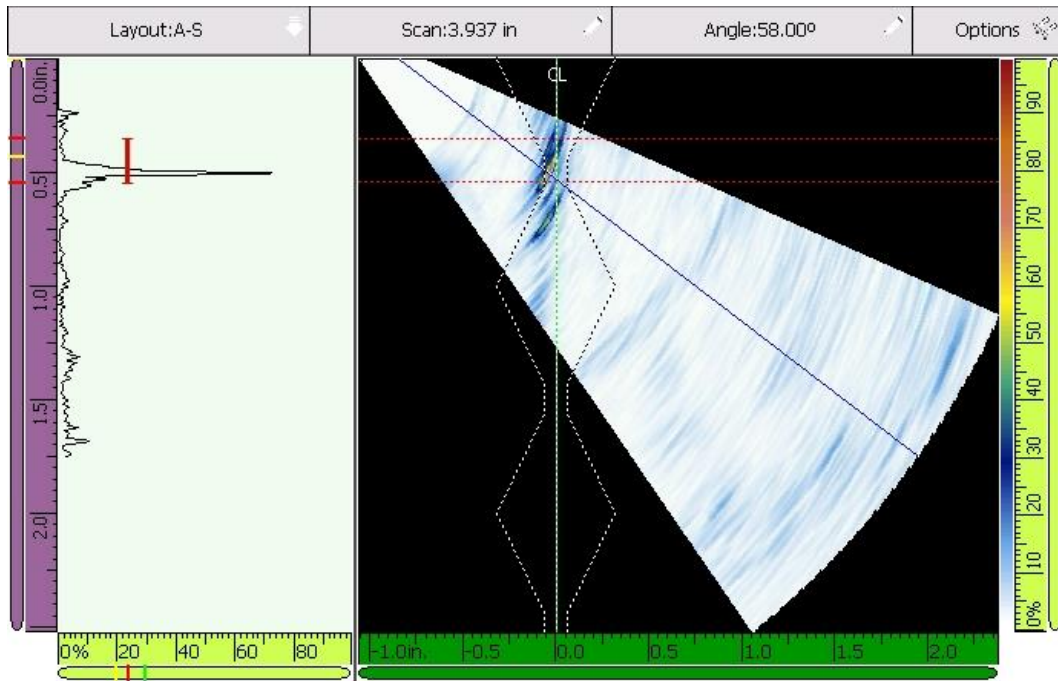


Figure 6.25 Flaw#1 (transverse crack)-Olympus PAUT

While, Figure 6.26 is PAUT representation of longitudinal crack.

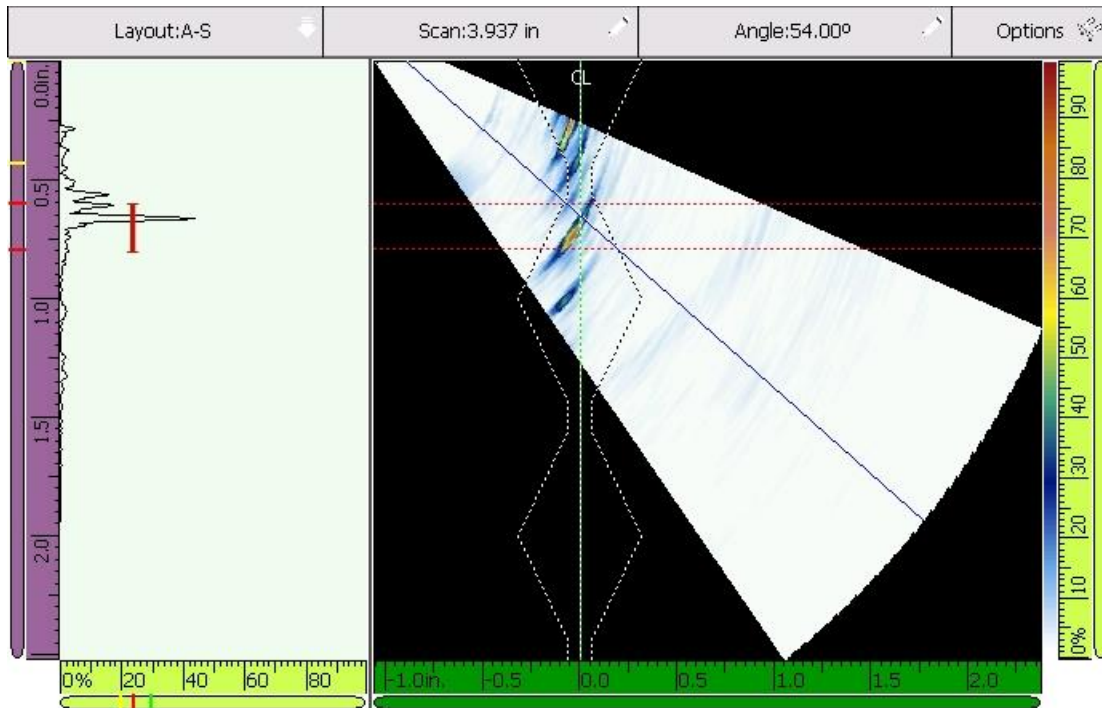


Figure 6.26 Flaw 2 (longitudinal crack)-Olympus PAUT

To confirm that welded area of austenitic stainless steel is anisotropic, Miniature Specimen Technique (MST) which is an NDT tool can be applied to estimate the mechanical properties of a welded area. But in this research, the welded area is mixture of austenite and ferrite phases. So, the properties are anisotropic. Also, we can check do quick test to confirm this by using magnetic piece. Since the austenite is paramagnetic and the ferrite is ferromagnetic. Thus, the welded area of austenitic stainless steel type 304 is mixture of these two phases and anisotropic.

CHAPTER 7

DAMAGE DETECTION IN AUSTENITIC STAINLESS STEEL WELDED PLATE

This chapter presents a theoretical and experimental study of ultrasonic guided wave method for health monitoring of austenitic stainless steel. This study is aimed at the monitoring of welded area status and characteristics of Lamb wave propagation through the plate. The interrogating waves generated by a transmitter piezoelectric wafer active sensor (T-PWAS) propagate along the structure, interact with the welded area and its defects, carry the information of welded area and are picked up by a receiver PWAS (R-PWAS). MATLAB[®] graphical user interface (GUI) named 'Modeshape_v2e'8 and WaveFormRevealer (WFR), these were generated and developed in Laboratory for Active Materials and Smart Structures (LAMSS), are produced the analytical results. WaveFormRevealer (WFR) is a general description of wave generation, propagation, interaction with damage, and detection. AGU-Vallen Wavelet, a freeware software program is used to create the wavelet transform of signals. The pitch-catch method is used to detect structural discontinuity that take place between a transmitter transducer and a receiver transducer. The detection is performed through the examination of the guided wave amplitude, phase, dispersion, and TOF in comparison with a "pristine" situation. Experiments on austenitic stainless steel welded plate are verified with the theoretical procedure. Scanning Laser Doppler Vibrometer (SLDV) is used to visualize the wave propagation through the austenitic stainless steel welded plate.

7.1 STATE-OF-THE-ART

Welding has been and continues to be more important secondary process to advance humankind because it has let us build our world (MESSLER, 1999). It is an important fabrication technique for stainless steels(Lippold & Kotecki, 2005). Austenitic stainless steels are the largest group in the stainless steel family. A completed weld may host a variety of defects and under the stress of operation, defects may propagate and mechanical failure may make catastrophic consequences. Inspection and evaluation of austenitic stainless steel multi-pass welds using ultrasonic methods is difficult due to material inhomogeneity and anisotropy, causing significant scattering and beam-steering(Connolly, 2009; Moysan et al., 2009). Thus, the embedded ultrasonic technology enables active SHM to determine its current state of structural health is desired for austenitic stainless steel weld condition monitoring(Giurgiutiu & Cuc, 2005).

A significant amount of research has been carried out aimed at developing SHM techniques for crack detection using ultrasonic waves. Giurgiutiu, (2002) detect a crack with PWAS that generate Lamb wave through aluminum plate, Poddar and Giurgiutiu (2015) detected and characterize a crack with Lamb wave, Yu and Giurgiutiu (2007) used PWAS phased array for guided wave damage detection. Also Yu and Giurgiutiu (2007) produced in situ optimized phased array for Lamb wave, Yu (2006) discussed damage detection using guided wave with PWAS array. Kijanka et al. (2015) used ultrasonic Lamb waves and piezoelectric rosettes for damage location.

(Shen, 2014) applied a pitch-catch experiment with PWAS to detect a notch which was machined onto plate, Figure 7.1 Pitch-catch experiment to detect the notch (Shen, 2014). Shen used WFR program to detect the damage theoretically. The damage interaction

coefficients are physically determined by the size, severity, type of the damage. A trial-and-error approach was used to tune the WFR damage interaction coefficients to the data obtained from the experiment.

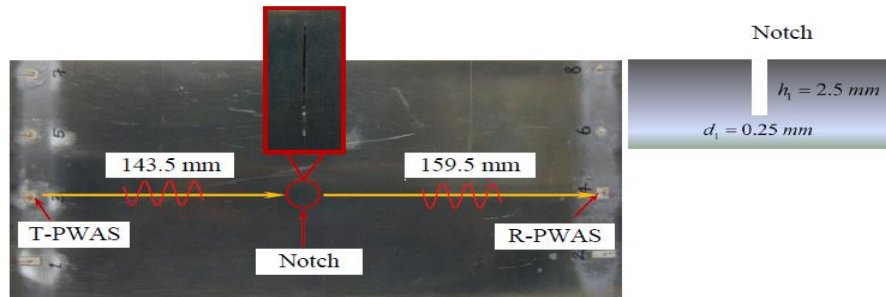


Figure 7.1 Pitch-catch experiment to detect the notch (Shen, 2014)

The results show a good matching between experimental results and analytical results. A new wave packet is generated due to mode conversion at the notch. Figure 7.2 shows a comparison between WFR simulations and experiments for Lamb waves interaction with a notch in pitch-catch method.

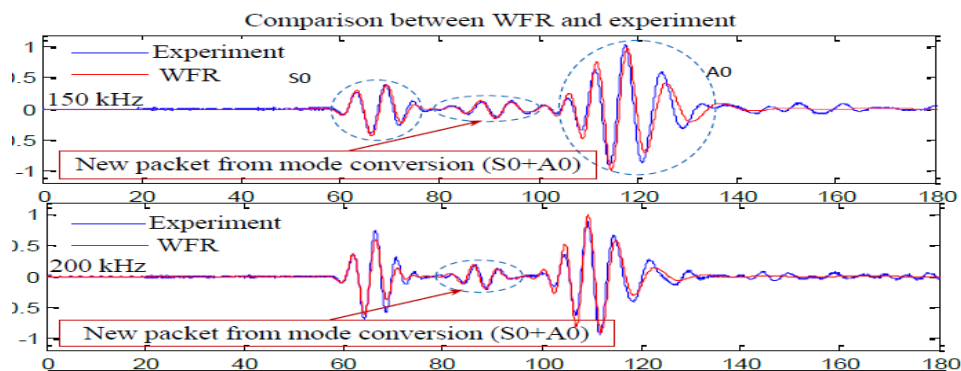


Figure 7.2 Comparison between WFR simulations and experiments for Lamb waves' interaction with a notch in pitch-catch method (Shen, 2014)

Higher order wavelets are used for de-noising the ultrasonic signals from the austenitic stainless steel welds and the results are compared with respect to the lower order wavelets(Praveen et al., 2013).

Sensor installation on the health-monitored structure is an important step that may have significant bearing on the success of the health monitoring process. The development of a reliable and repeatable installation method, which would provide consistent results, was one of the major objectives of PWAS development. In the installation process, the adhesive used to bond the sensor to the structure plays a crucial role. The thickness and stiffness of the adhesive layer can significantly influence the sensor's capability to excite the structure and may affect the quality and repeatability of the E/M impedance signatures. The cyanoacrylate adhesive is used in this study was M-Bond 200 from Measurements Group, Inc. The accompanying strain-gage installation instruction bulletin 309D (Measurements Group Inc., 1992) and installation kit (Figure 7.3) were also used. The complete procedure that was elaborated for bonding piezoelectric active sensors is presented in Figure 7.4.



Figure 7.3 The installation kit for strain gages (Giurgiutiu, 2014)

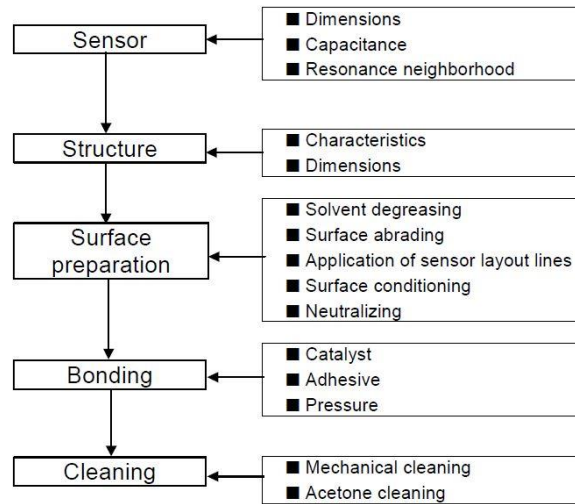


Figure 7.4 Installation procedure for piezoelectric active sensors (Giurgiutiu, 2014)

7.2 EXPERIMENTS WITH PITCH-CATCH METHOD

7.2.1 PITCH-CATCH SET-UP

The pitch-catch method can be used to detect structural changes that take place between a transmitter transducer and a receiver transducer, Figure 7.5. The detection is performed through the examination of the guided wave amplitude, phase, dispersion, and TOF in comparison with a “pristine” situation. Guided wave modes that are strongly influenced by small changes in the material stiffness and thickness (such as the A0 Lamb wave) are well suited for this method. The pitch-catch method can also be used to detect the presence of cracks from the wave signal diffracted by the crack. (Giurgiutiu & Cuc, 2005)

Propagating lamb waves

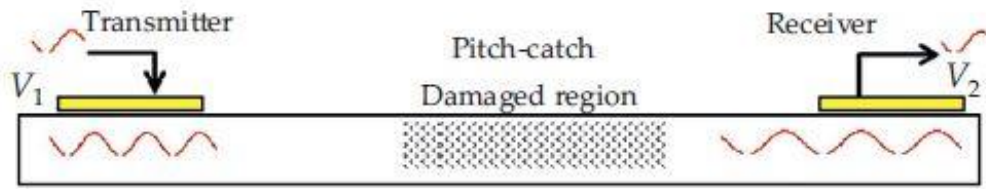


Figure 7.5 A pitch-catch configuration between a T-PWAS and a R-PWAS(Giurgiutiu, 2014)

In this work, a pitch-catch experiment was implemented on 20"×15"×0.25" thick austenitic stainless steel plate type 304. This plate is welded by gas tungsten arc welding (GTAW) technique and has two welding defects, longitudinal and transverse crack. Eight PWASs ($7 \times 7 \text{ mm}^2$ and 0.2 mm thick PWAS) are distributed in two line, four PWAS transducers on each side of welded area. Figure 7.6 shows the experimental setup to evaluate the propagating Lamb wave in the plate. The function generator was used to generate a 3-count Hanning window modulated tone burst, Figure 7.7 and Figure 7.8, applied to the T-PWAS. Lamb waves generated by the T-PWAS propagated along the structure, interacted with the welded plate, and were measured by the T-PWAS which was amplified by the charge amplifier.

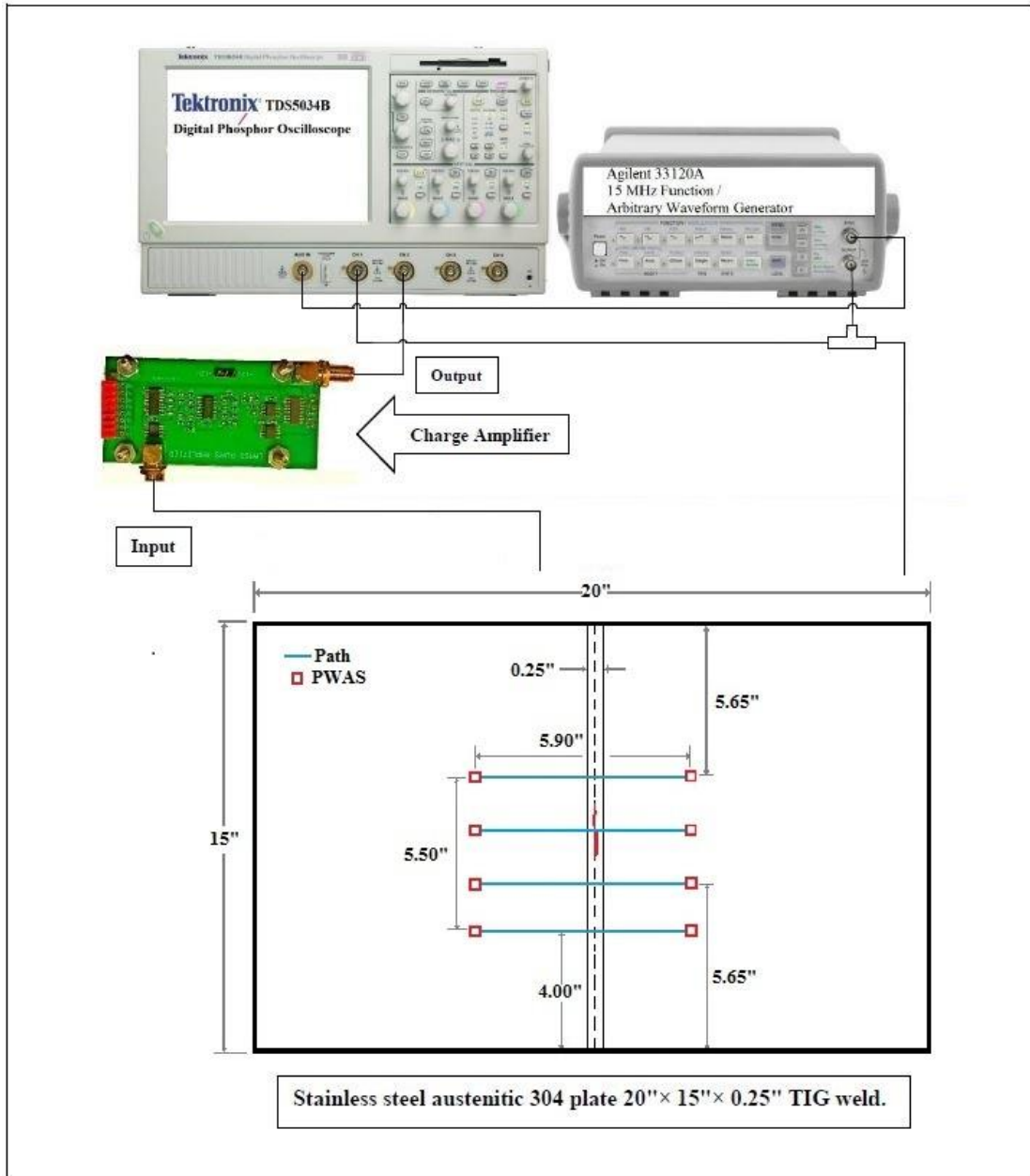


Figure 7.6 Setup for pitch-catch Lamb wave interaction with damage.

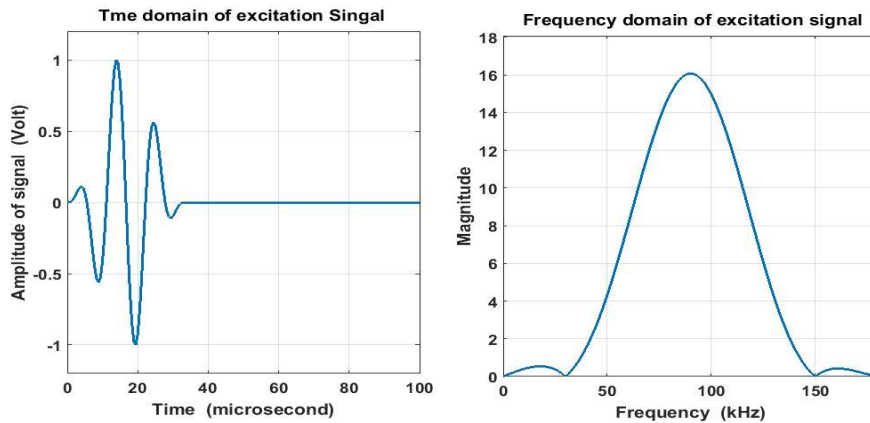


Figure 7.7 Hanning window modulated tone burst 3-count and its frequency domain at 90 kHz

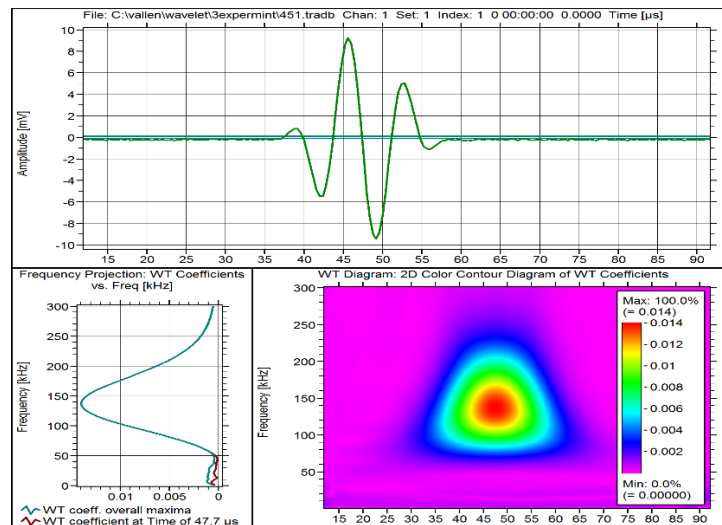


Figure 7.8 Waveform and wavelet transform of 3-counts tone burst excited signal at 135 kHz are generated by AGU-Vallen wavelet software

7.2.2 RESULTS AND DISCUSSION

7.2.2.1 TUNED LAMB WAVE

It is important to study and determine the tuning curve theoretically and experimentally before using the SHM methods to detect damages in a structure. The tuning curve reveals the behavior of Lamb modes when they are propagating in a

structure like plate as a function of the frequency of excitation signal. From tuning curve, it can be easy to determine the range of frequencies of suppressed and dominant of Lamb wave modes. So, a certain mode and its frequency can be chosen for damage detection (Giurgiutiu et al., 2003). studied the interaction between Lamb waves and PWAS theoretically and experimentally. The equation 1 considers the analytical foundation and expression of tuning effect:

$$\varepsilon_x(x,t) = -i \frac{a\tau_0}{\mu} \left\{ \sum_{\xi^S} (\sin \xi^S a) \frac{N_S(\xi^S)}{D_S'(\xi^S)} e^{-i(\xi^S x - \omega t)} + \sum_{\xi^A} (\sin \xi^A a) \frac{N_A(\xi^A)}{D_A'(\xi^A)} e^{-i(\xi^A x - \omega t)} \right\} \quad 7.1$$

The equation 7.1 only for A0 and S0 Lamb modes. Where ξ is the frequency dependent wave number of each Lamb wave mode and the superscripts S and A refer to symmetric and antisymmetric Lamb wave modes. Figure 7.9 shows the plotting of theoretical and experimental tuning curves of interaction of PWAS (7mm) and aluminum plate with 1.6 mm thickness. It was found that the asymmetric Lamb mode (A0) is much stronger than symmetric Lamb mode (S0) when the excitation frequency less than 150 kHz. After increasing the excitation frequency more than 200 kHz, the amplitude of S0 is increasing and the amplitude of A0 mode is decreasing significantly. At 300 to 400 kHz range, it was found a “sweet spot” for S0 mode. With tuning curve, the convenient excitation frequency (300 kHz) for pitch-catch experiment was chosen (Giurgiutiu, 2014).

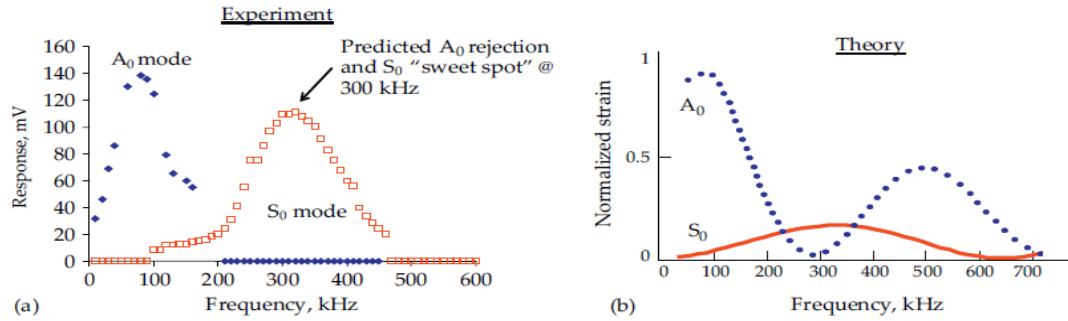


Figure 7.9 (a) Plotting tuning curve experimentally, (b) Plotting tuning curve theoretically(Giurgiutiu, 2014)

The tuning curve of interaction of a 1mm thickness aluminum plate and 7 mm rounded PWAS was implemented as is shown in Figure 7.10 (Yu et al., 2010). The frequency of excitation signal is being changed from 0-500 kHz. In this curve, two Lamb mods are excited simultaneously. At 300 kHz, the A0 mode is suppressed while the S0 is dominated. The tuning curve was used to find an active Lamb wave mode at certain frequency for detecting the damages in a plate.

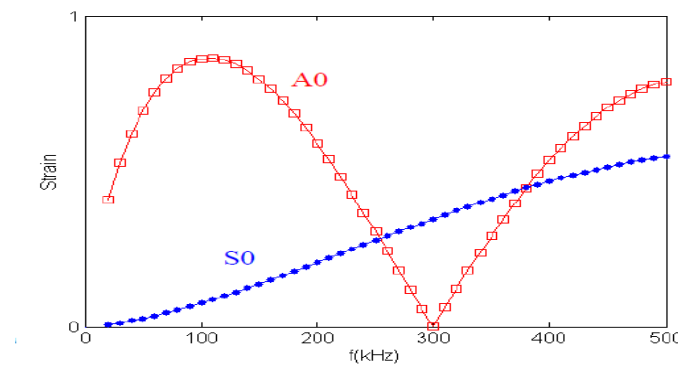


Figure 7.10 Tuning curve of 1mm aluminum plate (Yu et al., 2010)

MATLAB® graphical user interface (GUI) named WaveFormRevealer (WFR) software, which was generated and developed in Laboratory for Active Materials and

Smart Structures (LAMSS), is used to describe the wave generation, propagation and interaction with damage in a plate. Based on equation 1 of tuning expression, the WFR is used to plot the tuning curve of the material theoretically. The tuning curve is plotted by WaveFormerRevealer based up on the information of material properties, the thickness of plate, the PWAS size and the properties of excitation signal, Figure 7.11. The tuning curve is used to overcome the difficulties of choosing the certain Lamb mode and the frequency of excited wave to detect the damage in structure(Shen, 2014).

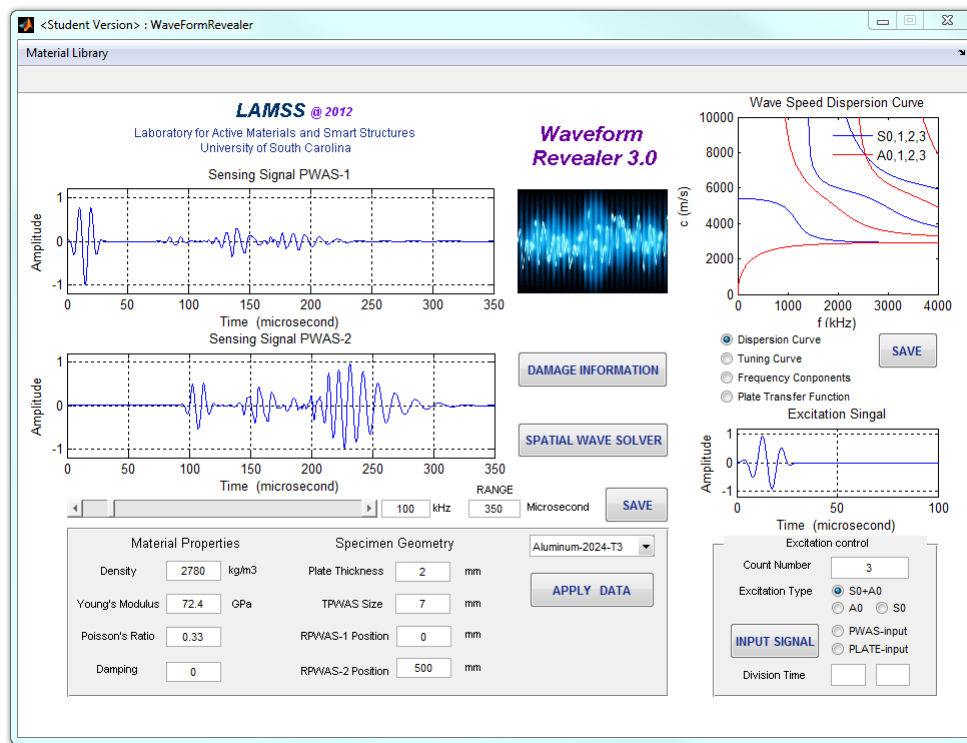


Figure 7.11 Main GUI of WaveFormRevealer (Shen, 2014)

Figure 7.12 shows pitch-catch method between PWAS#1 and #4 on austenitic stainless steel plate with thickness 6.5 mm to plot the tuning curve experimentally.

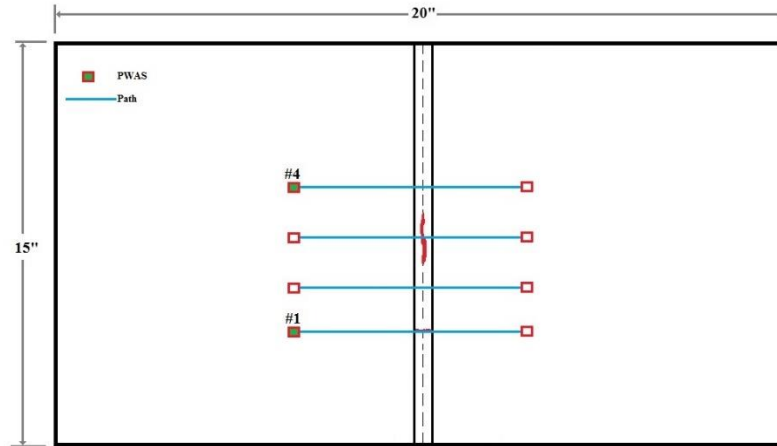


Figure 7.12 Schematic of the pristine plate and PWAS configuration

The experimental tuning curve is illustrated in Figure 7.13. It is found that, the frequency range between 0-250 kHz, A₀ mode and S₀ mode (Lamb wave modes) are existed simultaneously. Around the excitation frequency 100 kHz, both Lamb modes A₀ and S₀ have higher amplitude. Also, the asymmetric mode (A₀) is stronger than symmetric mode (S₀). In addition, the mode A₀ is partially rejected at frequency 210 kHz while S₀ mode is partially rejected at frequency 190 kHz. When the excitation frequency is higher than 270 kHz, the second asymmetric mode (A₁) becomes excited. Three modes A₀, S₀, A₁ appeared at frequency range 270- 480 kHz. The mode A₀ and S₀ reach the second peak around 300 kHz and A₀ is stronger than S₀. At frequency 380 kHz, the A₁ reaches its peak value and becomes stronger than other two modes, A₀ and S₀. After the frequency 380 kHz, the amplitude of three modes decreases gradually. Around excitation frequency 480, the second symmetric mode S₁ appears and becomes much dominant than other three modes.

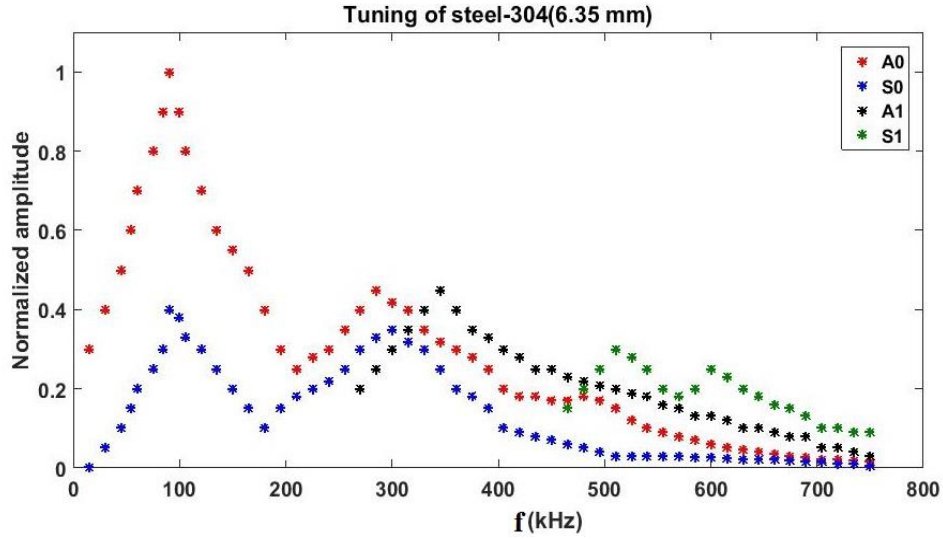


Figure 7.13 Tuning curve of a pristine plate (experimental)

The tuning curve is determined theoretically by using WaveFormRevealer (WFR) software as shown in Figure 7.14.

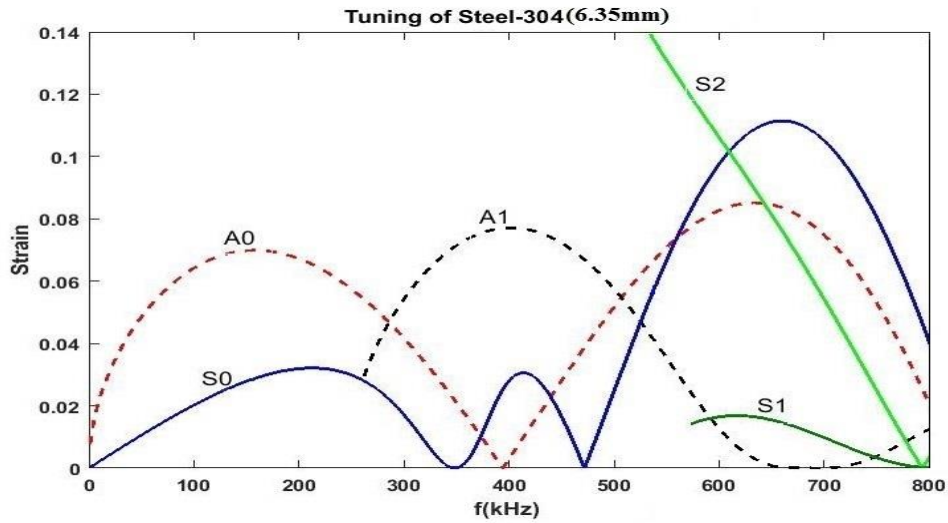


Figure 7.14 Tuning curve of a pristine plate (theoretical)

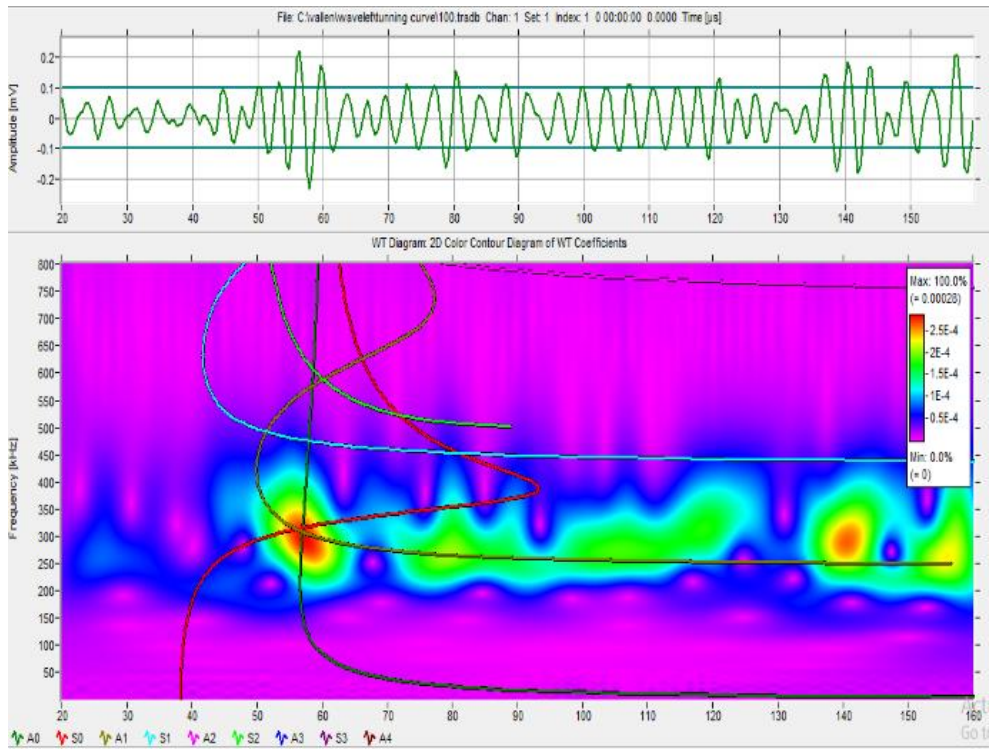
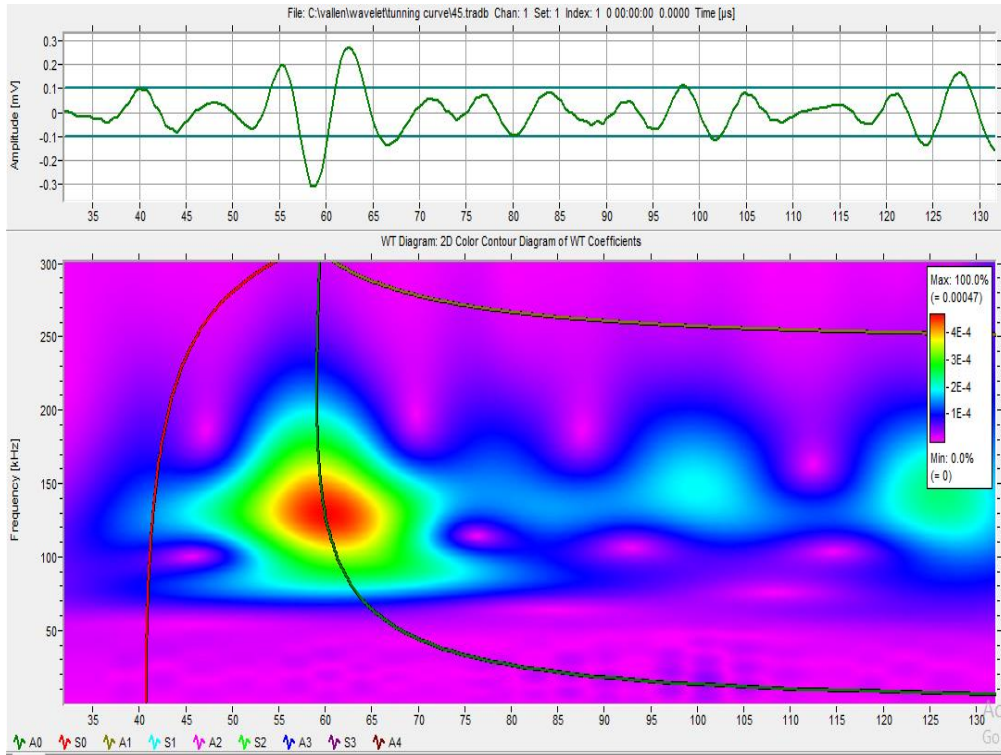
Figure 7.15 shows the Continuous Wavelet Transform (CWT) magnitude as a function of frequency versus time. The CWT was calculated with AGU-Vallen Wavelet,

a freeware software program (Vallen-System , 2001). This program has a Gabor function as the “mother” wavelet. Figure 7.15 (a) shows a superimposed between the waveform of receiving signal at 135 kHz and its wavelet transform with slowness curve (reciprocal of dispersion curve). This superposition is facilitated by an option that converts the group velocity scale to a time scale using the known propagation distance. It is found that just two modes A0 and S0 are appeared. The WT coefficients (value of signal amplitudes) of mode A0 is higher (red color) than S0.

Figure 7.15(b) shows three modes A0, S0, A1 are close to each other at excitation frequency 300 kHz.

At frequency range 270-400 kHz figure 10c, it is found that the interference between these modes is very clear and both S0 and A1 are dispersive. The mode A0 is still stronger than other modes.

At frequency excitation range 380- 450 kHz the mode A1 becomes stronger than other modes A0 and S0. After frequency excitation 480 kHz, the second symmetric mode S1 appears with others three modes A0, S0 and A1 as shown clearly in figure 10d. The S1 becomes much stronger than others modes around the frequency 510 kHz.



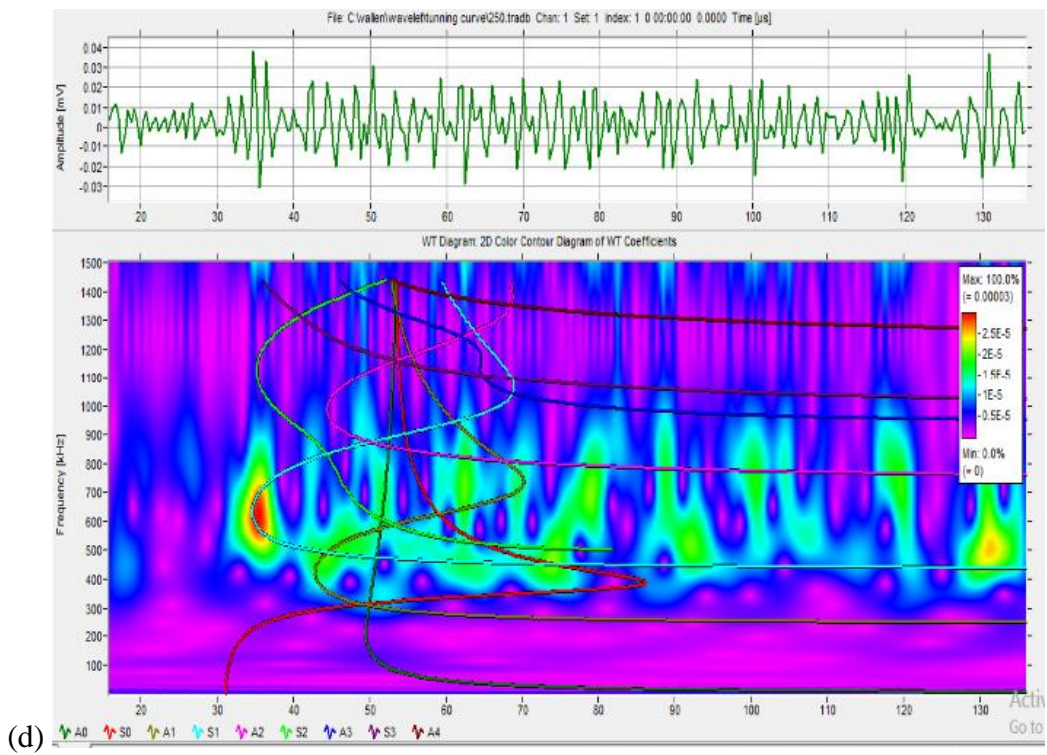
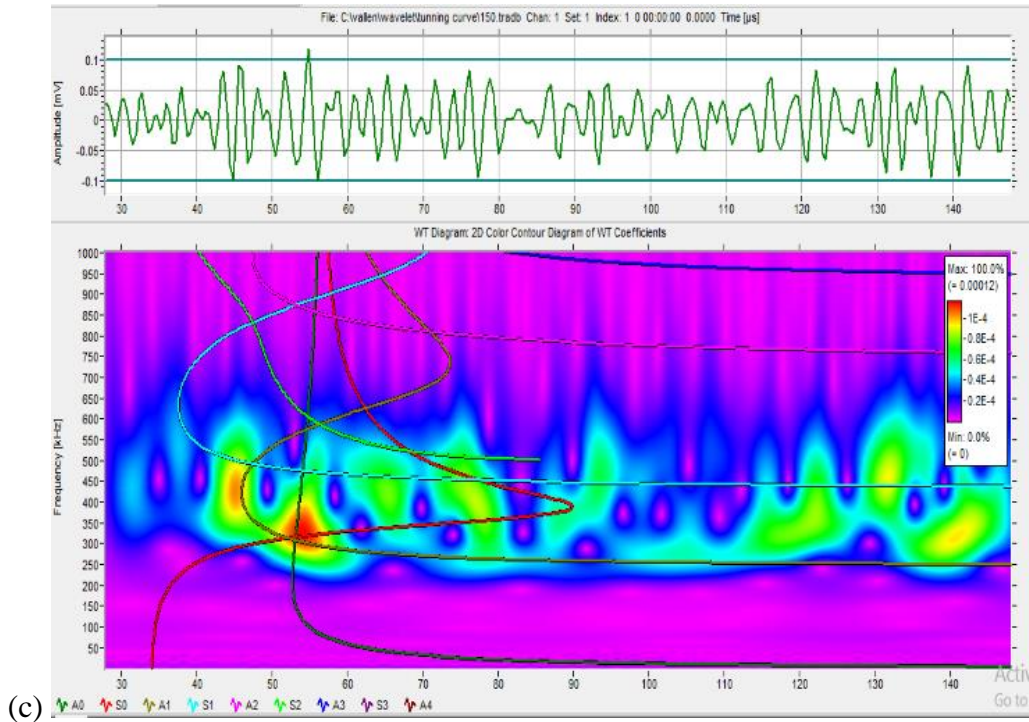


Figure 7.15 Superimposed between WT of signals with its slowness curve at frequency excitation (a) 135 kHz (b) 300 kHz (c) 450 kHz (d) 750 kHz

7.2.2.2 GROUP VELOCITY DISPERSION CURVE

The dispersion curve is defined as a the effect of changing frequency on the magnitude of wave speed in plate (Kundu, 2004). The group velocity of Lamb wave is considered as an important property of Lamb wave modes when investigate the traveling of Lamb wave packets (Giurgiutiu, 2014). Equation 7.2 shows the phase velocity c is derived to get the group velocity, c_g .

$$c_g = c^2 \left(c - fd \frac{\partial c}{\partial (fd)} \right)^{-1} \quad 7.2$$

The fd is the product of frequency with plate thickness and c , the phase velocity of Lamb wave, is estimated by equation 7.3

$$c^2 = E/\rho \quad 7.3$$

Where the E is the. Modulus of elasticity and ρ is the density of material. Equation 7.2 is used to plot the group velocity dispersion curves for symmetric and antisymmetric Lamb modes as shown in Figure 7.16

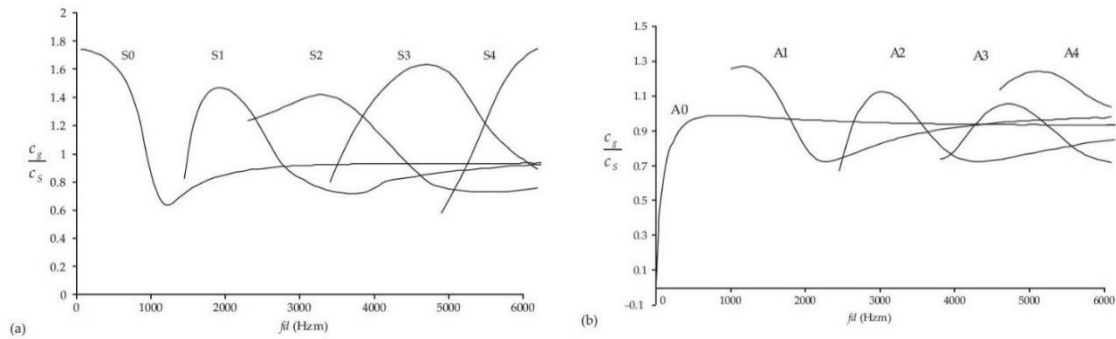


Figure 7.16 Group velocity dispersion curve in plates: (a) symmetric Lamb waves; (b) antisymmetric Lamb waves (Giurgiutiu, 2014)

A group velocity dispersion curve was plotted experimentally with two Lamb modes A0, S0 for 1 mm thick aluminum plate (Yu et al., 2010). It was found that S0 has constant speed because it is not dispersive, see Figure 7.17

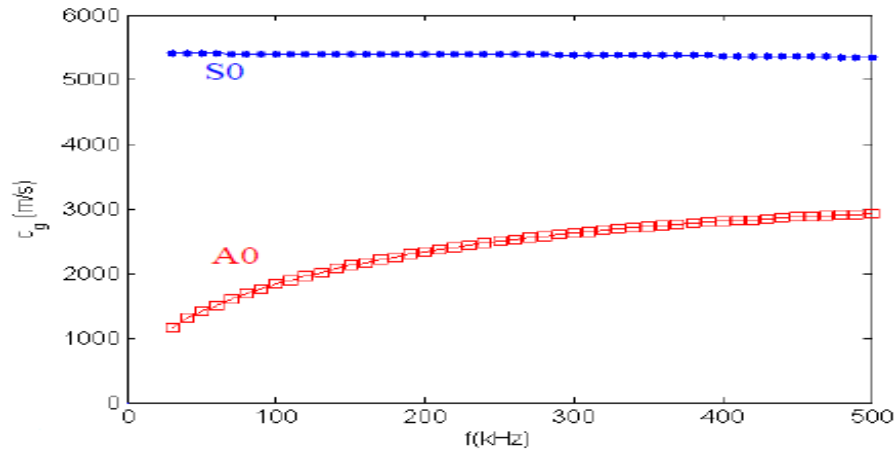


Figure 7.17 Experimental a group velocity dispersion curve (Yu et al., 2010)

In this work, the group velocity dispersion curves for 6.35 thick steel-304 are plotted theoretically and experimentally.

The group velocity dispersion curve as function of frequency is plotted theoretically by WaveFormRevealer software as shown in Figure 7.18. It can be concluded, in the range from 0 to 1000 kHz, the austenitic stainless steel plate of 6.35 mm thick has three symmetric modes (S0, S1, S2) and three antisymmetric modes (A0, A1, A2).

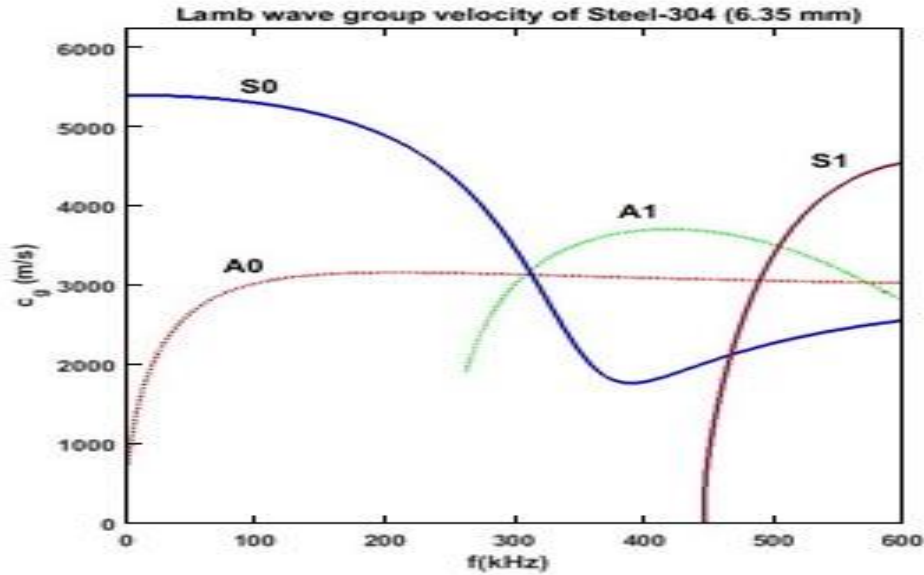


Figure 7.18 Dispersion curve (theoretical)

A pitch- catch experiment between PWAS#1 and #4 was performed with a range of frequency between 10- 600 kHz with 10 kHz step to determine the group velocity curves of Lamb wave modes (symmetric and antisymmetric), Figure 7.19. In the 0-250 kHz range, antisymmetric Lamb mode (A0) and symmetric mode (S0) are appeared. The group velocity of A0 highly increases between frequency ranges of 0-150 kHz (dispersive situation). After frequency 150 kHz the velocity of A0 becomes approximately constant. While the group velocity of S0 highly decrease between frequencies range 0-250 kHz. Around the frequency of 300 kHz, the group velocities of A0, S0 and A1 are much closed to each other. In the 300 to 450 kHz range, the velocity of A1 is higher than A0 (constant) and S0, which is in dispersive situation. In the frequency range 450 to 600 kHz, four Lamb modes are appeared (A0, S0, A1 and S1). The group velocity of S1 is highly increasing in this range. The velocity of S0 is slightly increasing while A1 is slightly decreasing. A0 is still constant. In frequency point 600 kHz, the S1 has higher

velocity than others while S0 has lower velocity than A0 and A1 which are close to each other.

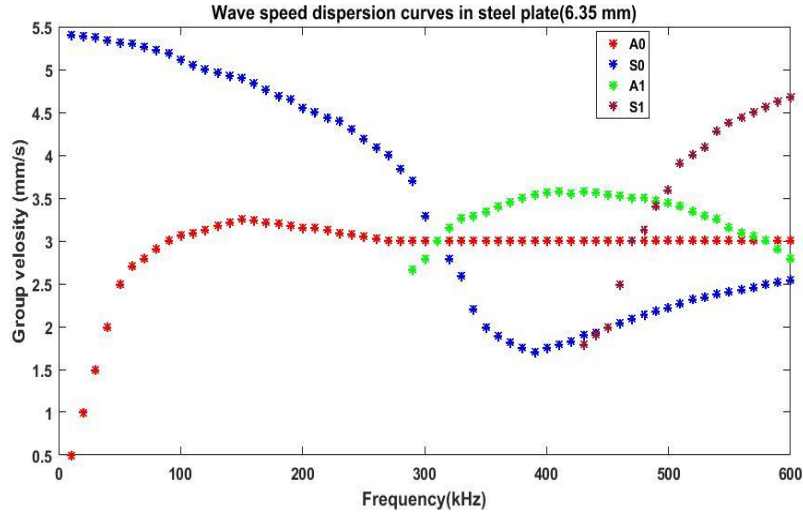


Figure 7.19 Dispersion curve (experimental)

7.2.2.3 MODE SHAPE OF LAMB WAVE

The displacements of Lamb wave modes vary across the plate thickness with varying frequency and thickness. This variation called the displacement mode shapes. The structure of Lamb wave has two displacements, in plane displacement (u_x) and out plane displacement (u_y). For SHM, it is important to study the shape Lamb wave modes to choose a certain types of mode shapes which are important for damage detection in plates. The displacement of symmetric and anti-symmetric modes Lamb can be estimated using equation (4) and (5). (Giurgiutiu, 2014).

For symmetric Lamb modes

$$\begin{aligned}
 u_x^S(x, y, t) &= iC^S \left[-2\xi^2 \eta_S \cos \eta_S d \cos \eta_P y + \eta_S (\xi^2 - \eta_S^2) \cos \eta_P d \cos \eta_S y \right] e^{i(\xi x - \omega t)} \\
 u_y^S(x, y, t) &= C^S \left[2\xi \eta_P \eta_S \cos \eta_S d \sin \eta_P y + \xi (\xi^2 - \eta_S^2) \cos \eta_P d \sin \eta_S y \right] e^{i(\xi x - \omega t)}
 \end{aligned}
 \tag{7.4}$$

For antisymmetric Lamb modes

$$\begin{aligned} u_x^A(x, y, t) &= iC^A \left[2\xi^2 \eta_S \sin \eta_S d \sin \eta_P y - \eta_S (\xi^2 - \eta_S^2) \sin \eta_P d \sin \eta_S y \right] e^{i(\xi x - \omega t)} \\ u_y^A(x, y, t) &= C^A \left[2\xi \eta_P \eta_S \sin \eta_S d \cos \eta_P y + \xi (\xi^2 - \eta_S^2) \sin \eta_P d \cos \eta_S y \right] e^{i(\xi x - \omega t)} \end{aligned} \quad 7.5$$

The y in above equation is a point across the thickness of plate; C^S and C^A calculates the mode shape amplitudes; η_P and η_S are calculated in Eq. (1.6)

$$\eta_P^2 = \frac{\omega^2}{c_p^2} - \xi^2; \quad \eta_S^2 = \frac{\omega^2}{c_s^2} - \xi^2; \quad c_p = \sqrt{\frac{\lambda + 2\mu}{\rho}}; \quad c_s = \sqrt{\frac{\mu}{\rho}}; \quad 7.6$$

Where λ and μ are Lamé's constants of the material, and ρ is the material density.

From equation (1) and Figure 7.20. It can be concluded that the x displacement u_x changes symmetrically with y . While y displacement u_y changes antisymmetrically with y

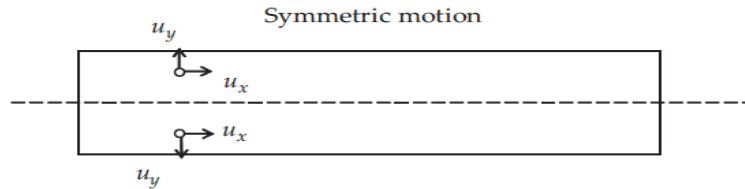


Figure 7.20 Symmetric motion

The shape Lamb modes across the 1 mm thickness of aluminum plate were plotted and proved that the modes shape changes with frequency. (Giurgiutiu, 2014). Figure 7.21 shows the modes shape of symmetric Lamb mode S0 across 1 mm thickness of aluminum plate changes with frequency.

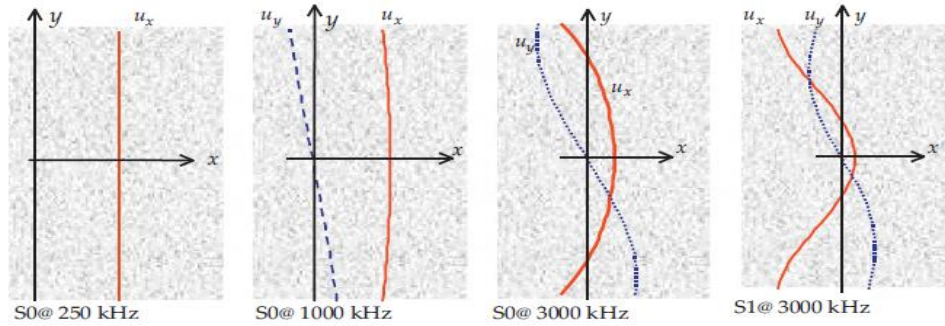


Figure 7.21 Modes shape of S0 across 1 mm thickness of aluminum plate changes with frequencies (Giurgiutiu 2014)

From the above equation (1.2) and Figure 7.22, it can be concluded that the displacement $u_x(y)$ changes antisymmetrically with y . While the displacement $u_y(y)$ changes symmetrically with y . So this motion is considered as an antisymmetric motion. The modes shape of antisymmetric Lamb modes A0 across the 1 mm thickness aluminum plate were plotted with different magnitude of frequencies are shown in Figure 7.23 (Giurgiutiu, 2014).

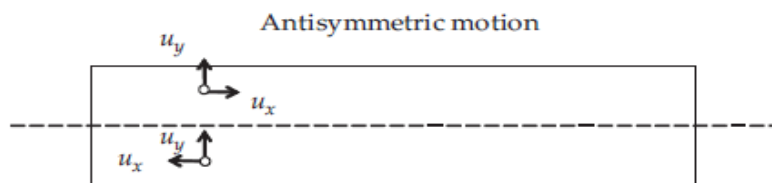


Figure 7.22 Antisymmetric motion

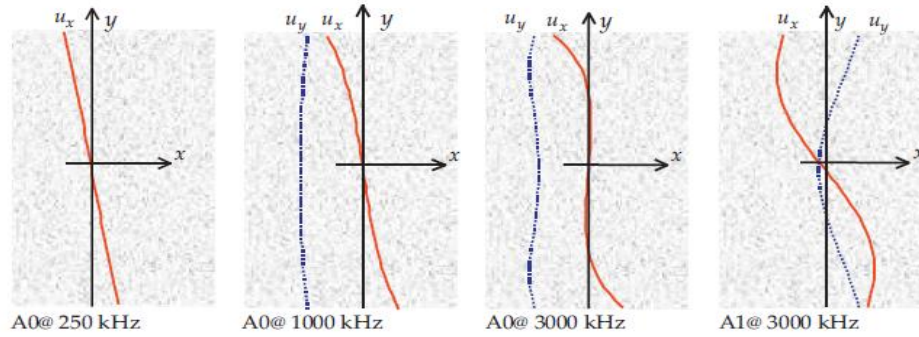


Figure 7.23 Modes shape of A0 across 1 mm thickness aluminum plate at different frequencies (Giurgiutiu, 2014).

The MATLAB® graphical user interface (GUI) named ‘Modeshape_v2e which was generated in Laboratory for Active Materials and Smart Structures (LAMSS) was used to plot the displacement vectors and modes shape of Lamb modes a cross 14 mm thick steel (Kamas, 2014). The continuous lines depict the in-plane displacement u_x and the dotted lines depict the out-of-plane displacement u_y , Figure 7.24. It can be concluded that at 450 kHz, the displacement u_x has high oscillation near the top and bottom surfaces of the plate and small oscillation around the middle of plate thickness. The displacement u_y on the surface is almost twice as large as that on the mid-surface.

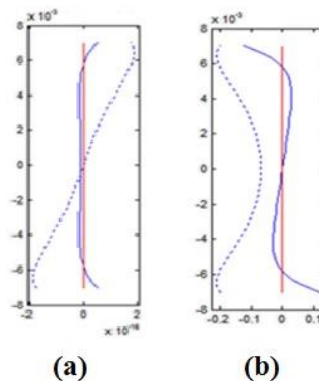
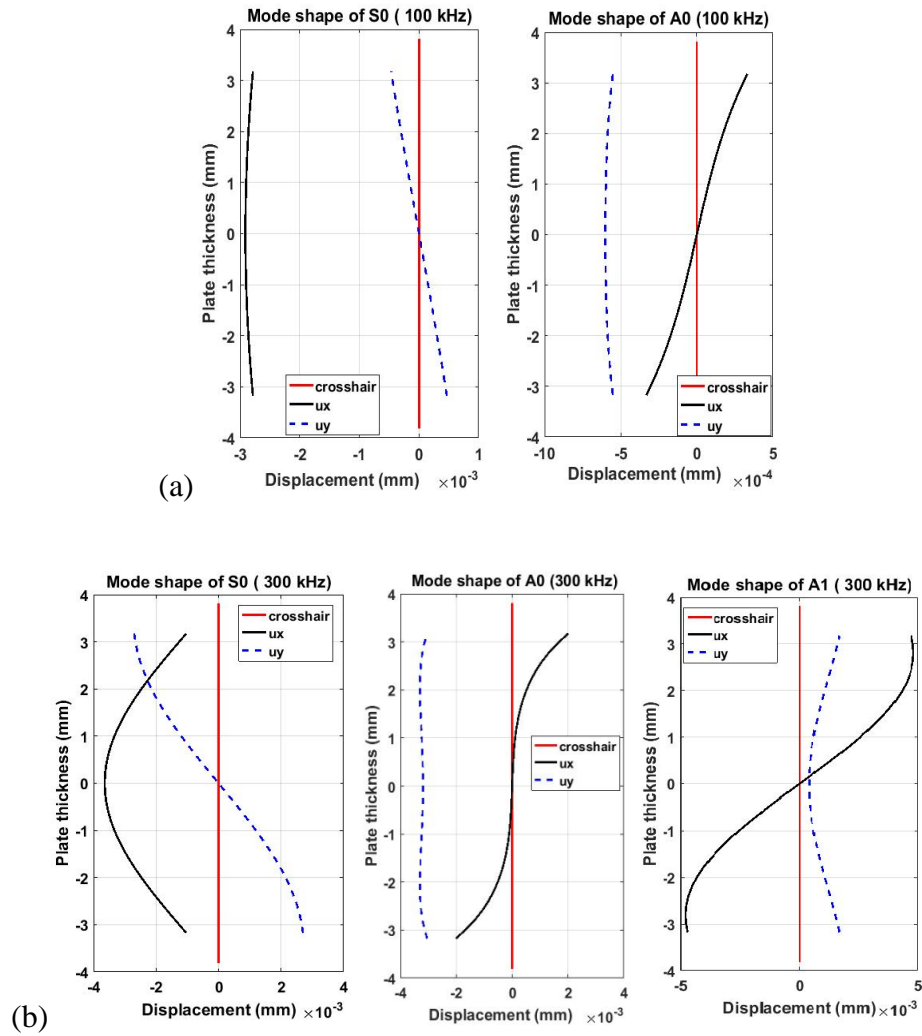


Figure 7.24 Mode shapes for 19-mm thick steel at frequency 450 kHz (a) symmetric (b) antisymmetric (kamas, 2014)

In this work, the modes shape across the 6.35 thick steel-304 for various Lamb wave modes at different values of frequency were plotted by using a MATLAB® graphical user interface (GUI) named ‘Modeshape_v2e.’, Figure 7.25.

In-plane displacement (u_x) and the out-of-plane displacement (u_y) of the modes are changed w.r.t. the change of fd.



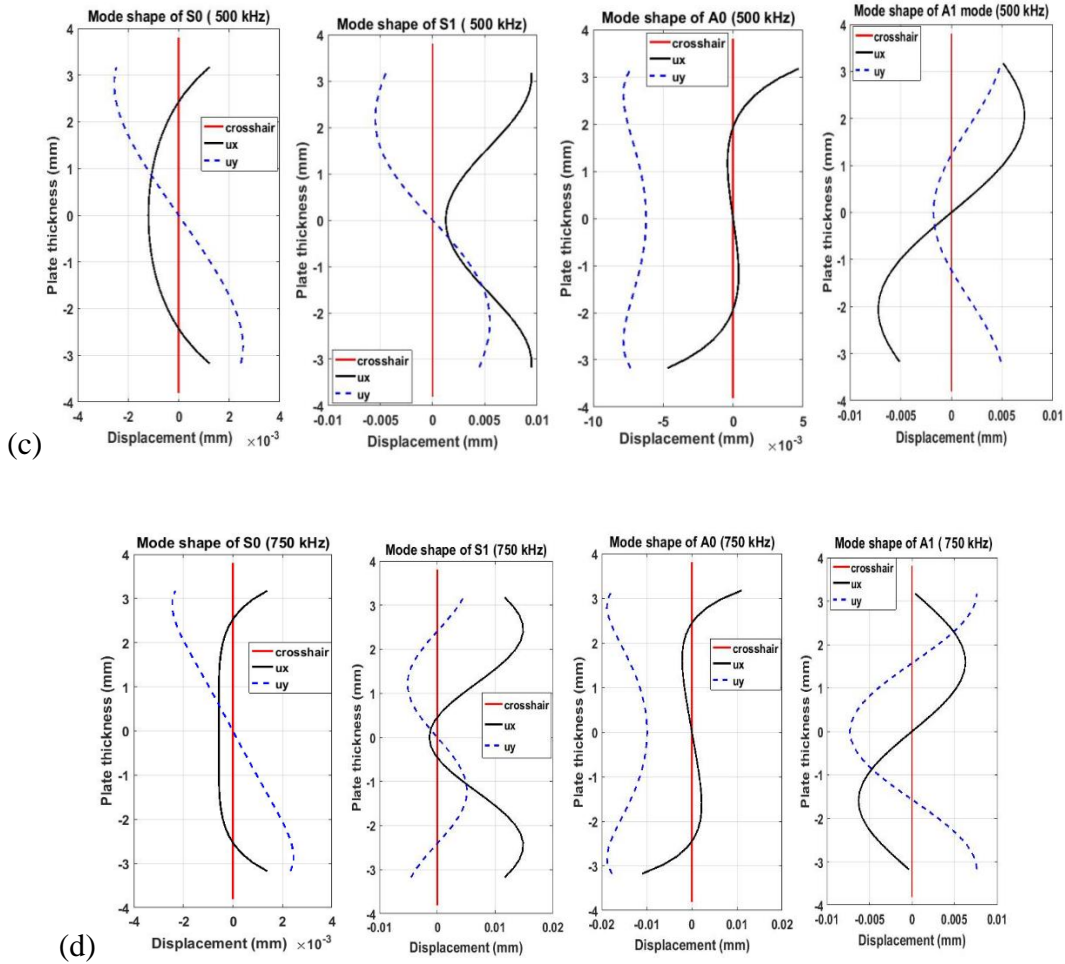


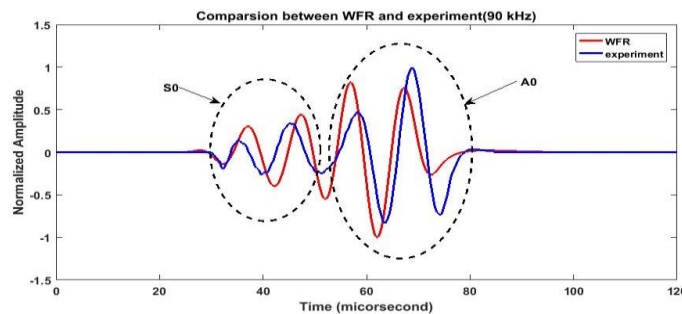
Figure 7.25 Modes shape across the 6.35 mm thickness of steel-304 plate for various Lamb modes at various frequencies

It can be concluded from above shape Lamb modes that there is a clear relation between the mode shape curvature of Lamb modes and excited frequency. The modes shape curvature of Lamb modes (A0, S0, A1, S1) increase with increasing the excited frequency. At excited frequency 500 kHz, the mode shape curvature of Lamb modes (S1, A1) are more curvature than (S0, A0). So, it can be concluded that the mode shape curvature increases with increasing mode order at certain frequency. From most of mode shape plots, the displacement u_x is larger than u_y . The last point that can be noticed from the mode shape plots is the number of nodes (the intersections of u_x and u_y with

crosshair). The displacements u_x and u_y have a different behavior related to the number of nodes. The number of nodes of displacement u_x increase with increasing frequency and decrease with increasing the order number of Lamb modes for both A and S modes. The Lamb wave modes A and S have a different behavior related to the nodes of displacement u_y . The u_y of S0 mode has one node for all the values of frequencies. However, the number of nodes of displacement u_y increase with increasing the order of S. The displacement u_y of A0 mode has no nodes with all the values of frequency. While A1 mode has two nodes for all the values of frequency more than 500 kHz. Also, it can be concluded that the number of nodes of u_y increase with increasing the order of A.

7.2.2.4 LAMB WAVE PROPAGATING IN PRISTINE PLATE

Figure 7.26 shows the time domain and frequency domain of tone burst excitation signal at 90 kHz. The analytical waveforms were obtained by using WFR software, which is generated by LAMSS. The mechanical property of material, plate thickness, PWAS size and propagating distance are used as input information. Figure 1.26 shows the comparison between analytical solution from WFR and experimental data.



(a)

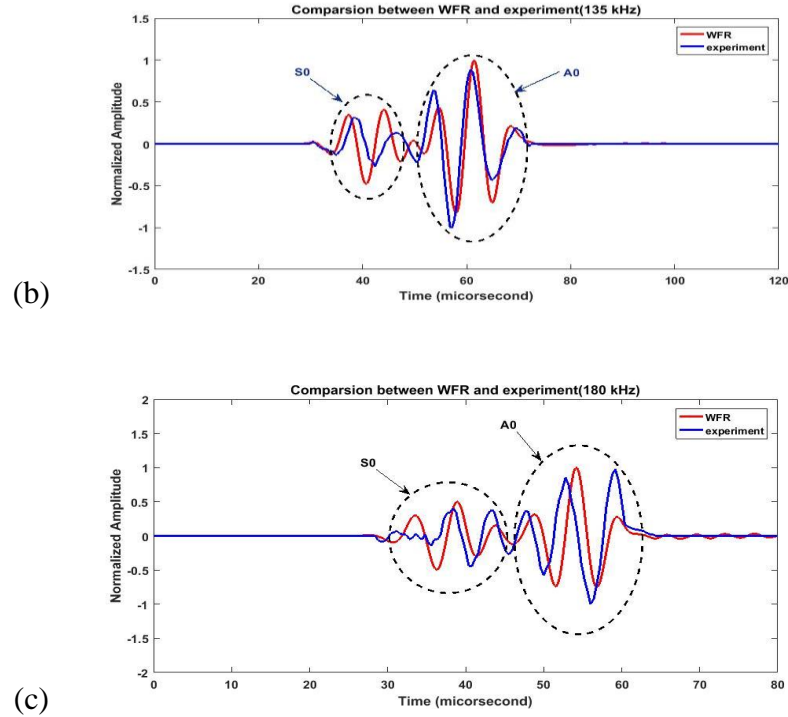


Figure 7.26 Comparison between WFR and experiment for Lamb wave modes propagation in a pristine 6.35-mm austenitic stainless steel-304 plate

From Figure 7.26, it can be noticed that, at frequencies 90 kHz, 135 kHz and 180 kHz there are two Lamb wave modes A0 and S0. Also, it can be observed that the experimental results match with WFR results.

7.2.2.5 LAMB WAVE PROPAGATING IN WELDED AREA

The pitch-catch technique with PWAS is applied on welded area of the plate to investigate Lamb wave propagation. The detection of weld defects is implemented by making comparison between two signals. The first one is the pristine signal that presents pristine welded area. The second signal is the damaged signal that that presents defected weld area. The detection of weld defects is implemented by comparing the features of the second signal (amplitude, phase, dispersion and TOF) with the first signal (pristine signal).

Firstly, pitch-catch experiments with PWAS are done for pristine welded areas, #2-#7 and #4-#5 as shown Figure 7.27, to verify these areas have the same pristine signal.

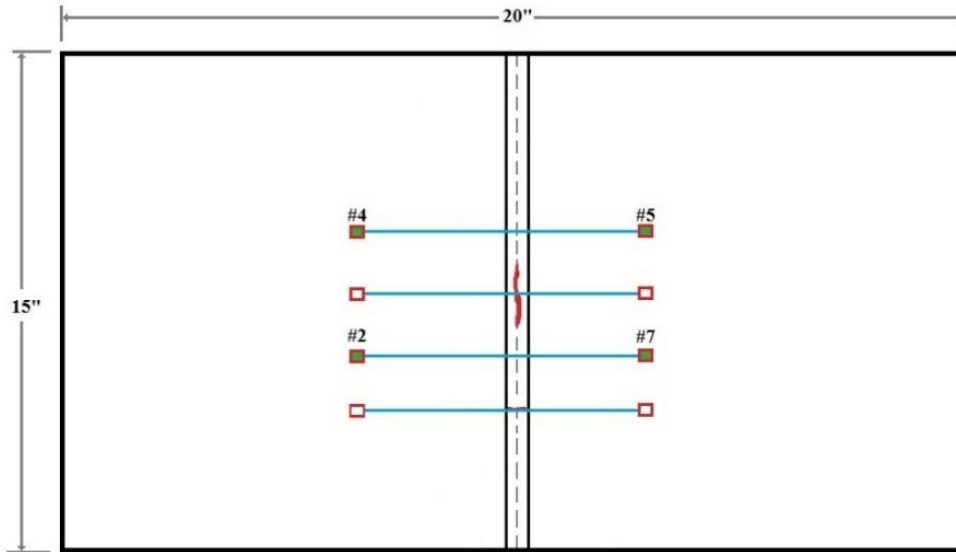


Figure 7.27 Schematic of the pristine welded areas and PWAS configuration

Figure 7.28 shows small difference between the signals of pristine welded areas due to the small difference in the distances between T-PWAS and R-PWAS.

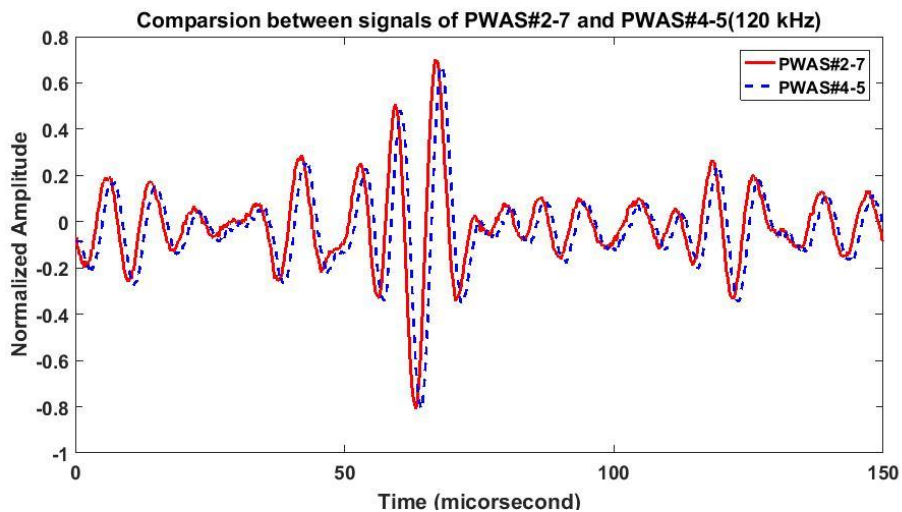


Figure 7.28 Pristine signal before modification

After measuring the distance difference, multiplying this distance with velocity and based on this multiplication factor, the signals are shifted and matched perfectly as shown in Figure 7.29.

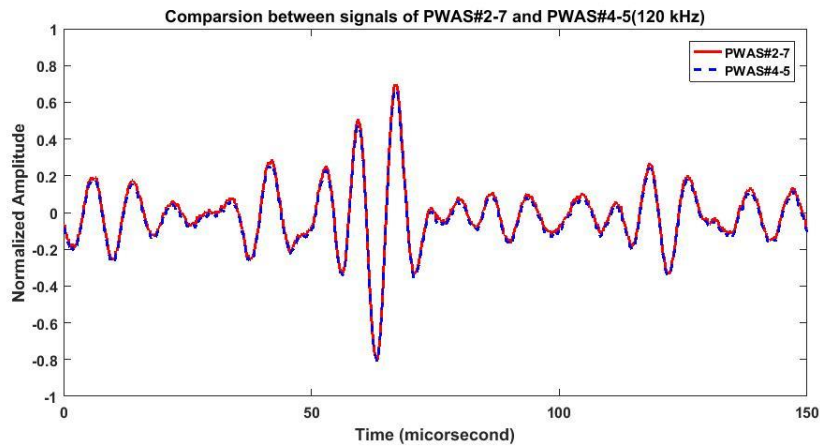


Figure 7.29 Pristine signal after modification

The results show a good matching for the signals of pristine welded areas at different excitation frequencies as shown in Figure 7.30. So, the signal of area 2-7 is chosen as pristine signal for the comparison with the signals of damaged areas.

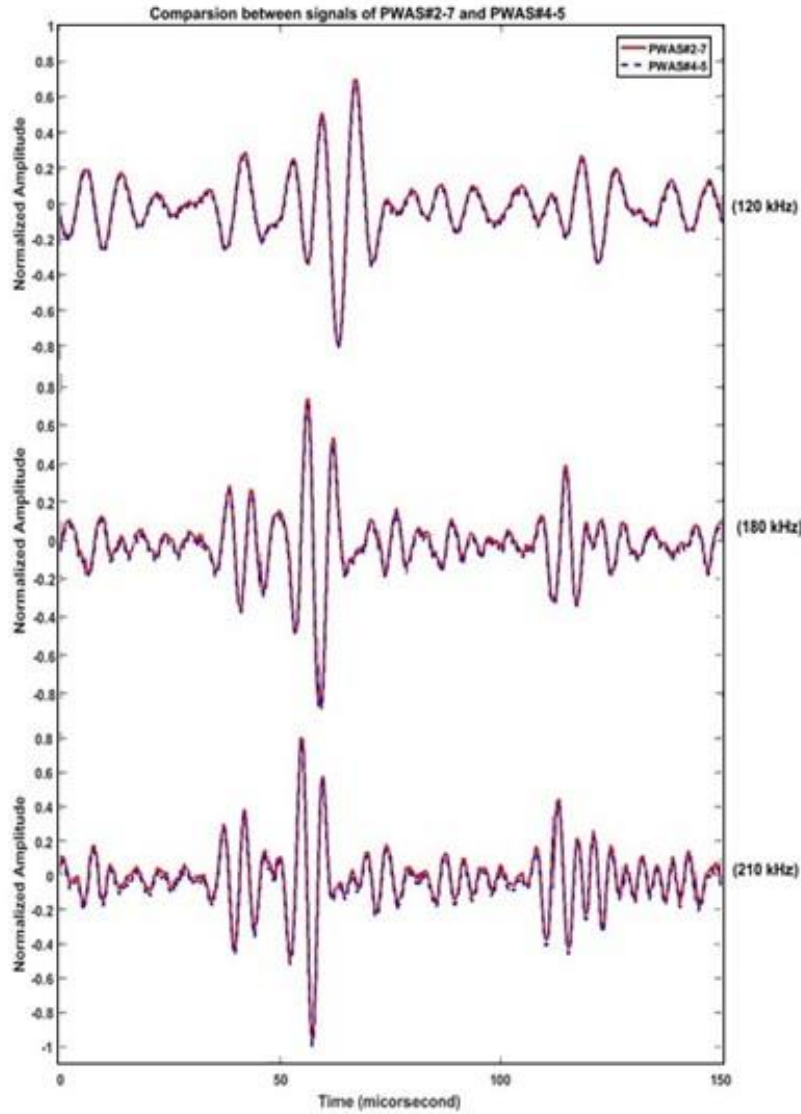


Figure 7.30 signals comparison of pristine welded areas at different frequencies

Secondly, a pitch-catch experiment with PWAS is performed at different frequencies for area 1-8 which has a transverse crack as shown in Figure 7.31.

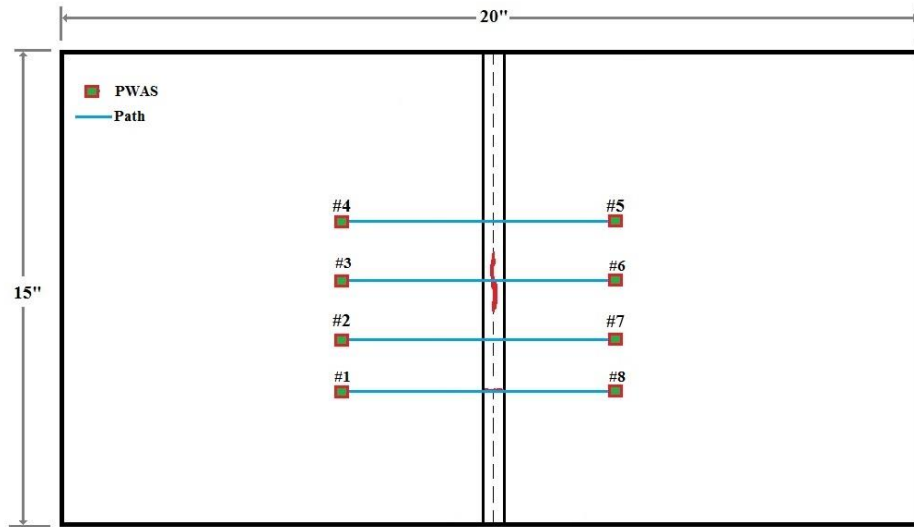


Figure 7.31 Schematic of the welded plate and PWASs configuration

Thirdly, a pitch-catch experiment with PWAS is conducted at different frequencies for area 3-6 which has a longitudinal crack as shown in Figure 7.31.

The signals of transverse crack in area #1-#8 and longitudinal crack in area #3-#6 are compared with the pristine signal which is signal of area #2-#7.

Figure 7.32 and Figure 7.33 show a great comparison between damaged signals (transverse and longitudinal crack signals) with the pristine signal at different frequencies.

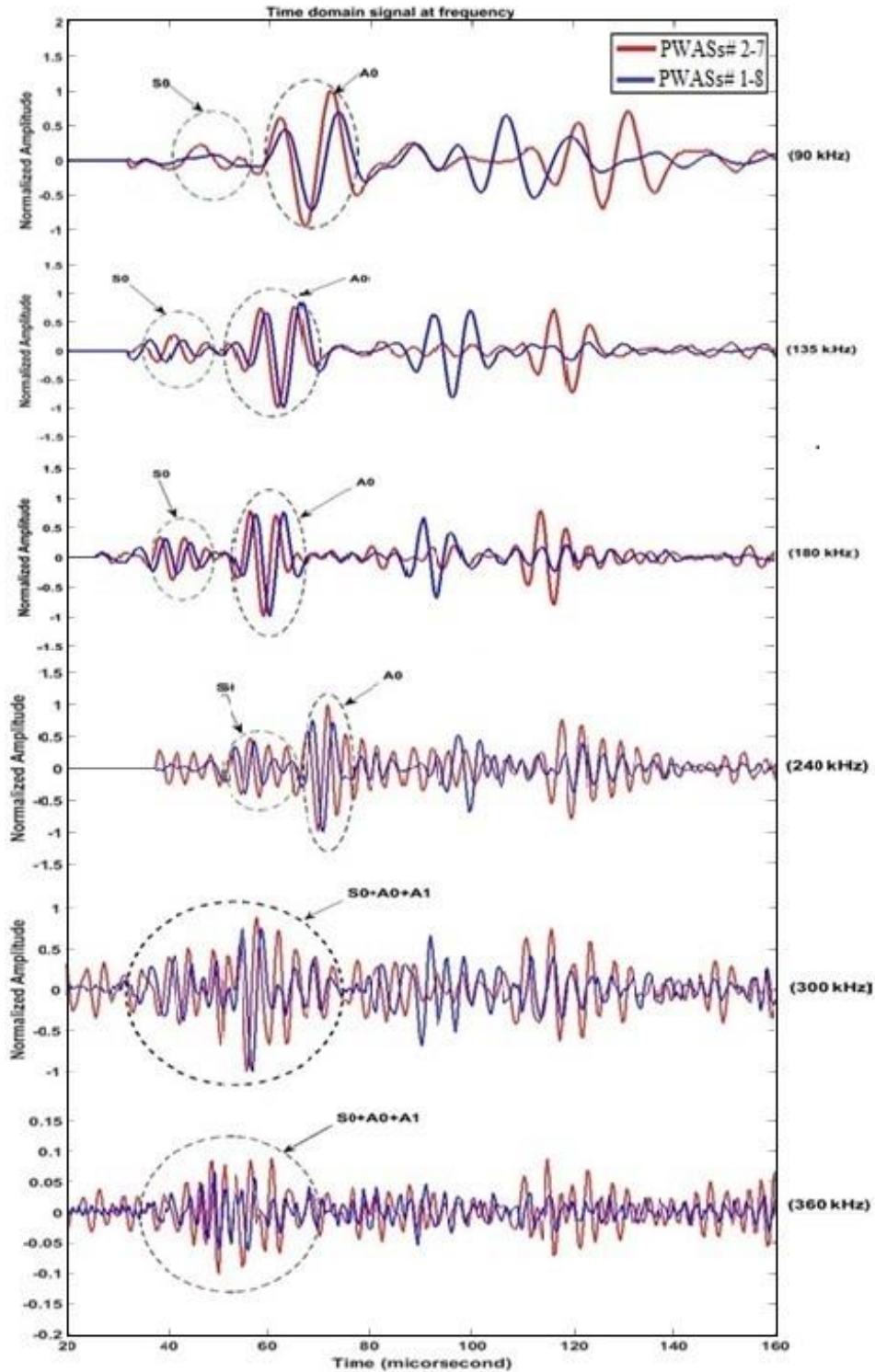


Figure 7.32 A comparison between pristine signal and damaged signal (transvers crack signal) at 90 kHz, 135 kHz, and 180 kHz, 240, 300, and 360 excited signals

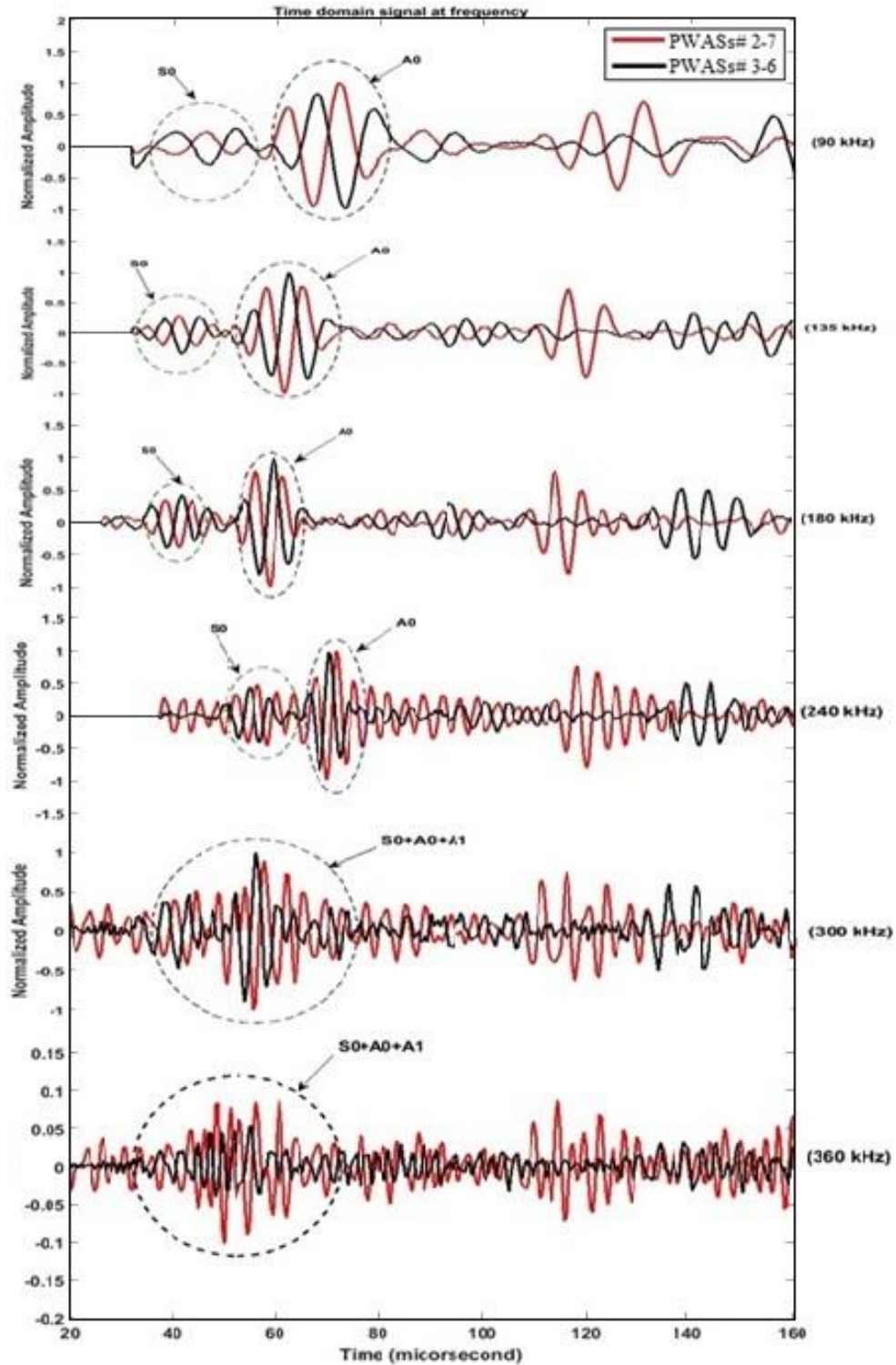
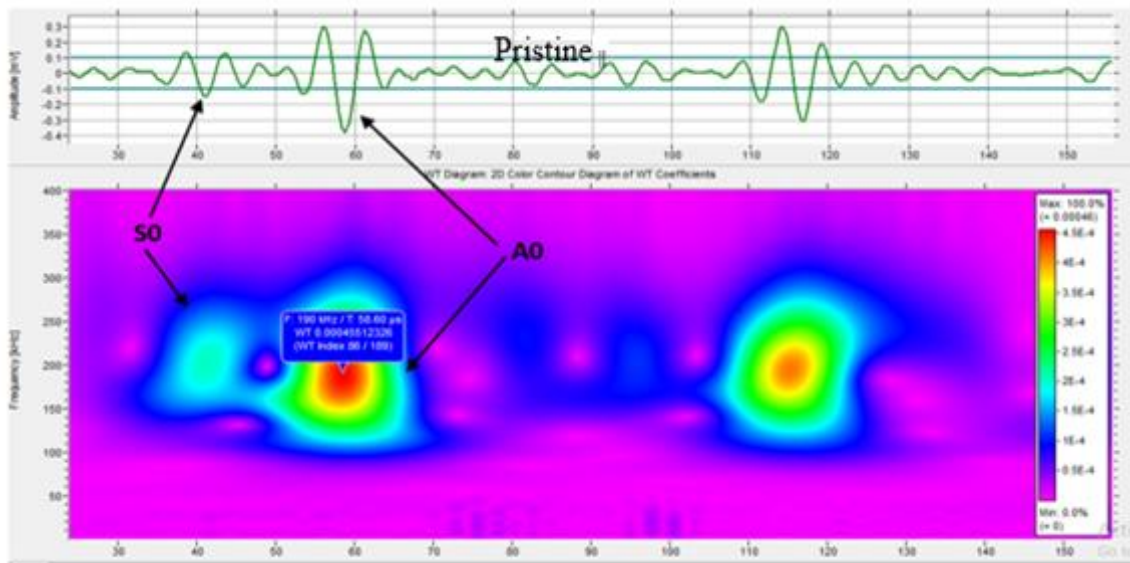


Figure 7.33 A comparison between pristine signal and damaged signal (longitudinal crack signal) at 90 kHz, 135 kHz, and 180 kHz, 240, 300, and 360 excited signals

It can be noticed that there are clearly differences between the pristine signals and both type of damaged signals at different frequencies. Since Lamb wave is not active at the surface of the plate, as shown in Figure 7.25, at low frequencies. So, in case of transverse crack (damage close to the surface) at low frequencies, the difference between pristine and damaged signals will be not clear. While, at high frequencies, the difference will be clear because the Lamb wave is active at the surface of the plate. The features of propagating signals (amplitude, frequency and time of flight) are affected by damaged area. Figure 7.34 shows the waveforms and wavelet transforms of pristine, transvers damage and longitudinal cracks signals at 180 kHz excitation frequency. It can be obviously seen the features values of each signals.



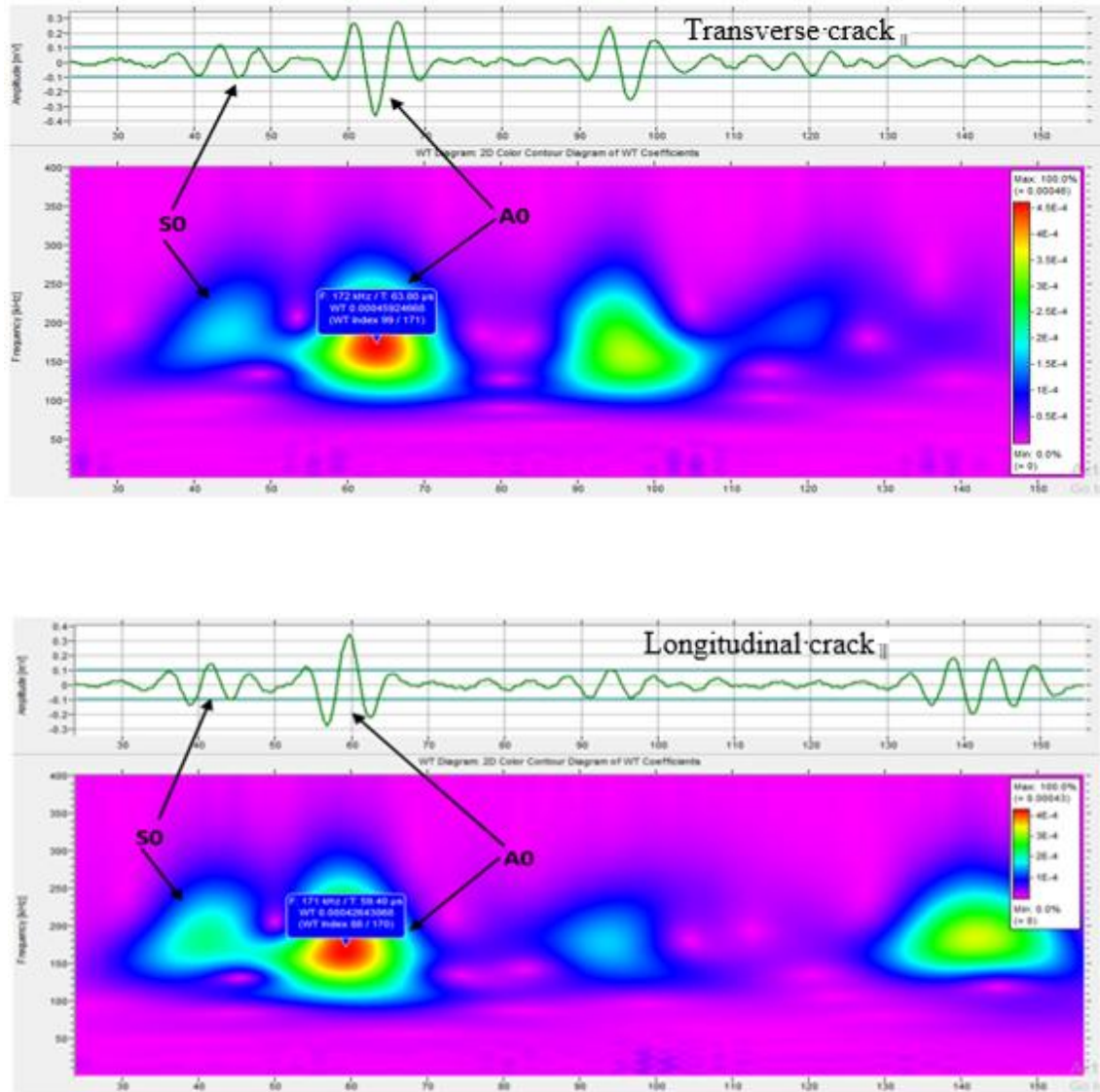


Figure 7.34 Wavelet transforms of pristine weld, transverse crack and longitudinal crack signals at excitation frequency of 180 kHz

7.3 EXPERIMENTS WITH SCANNING LASER DOPPLER VIBROMETER

7.3.1 SLDV SET-UP

To visualize the wave propagation through the austenitic stainless steel welded, the Polytec PSV-400 Scanning Laser Doppler Vibrometer is used to capture the propagating wave field. The experimental setup is shown in Figure 7.35. The excitation

signal, 3-count Hanning window modulated tone burst, generated by the HP 33120A function generator and HAS 4014 voltage amplifier is applied to the T-PWAS. The SLDV scans the welded plate surface, and measures the out-of-plane vibration velocity during wave propagation. The out-of-plane wave field is then visualized by post processing of the scanning data. The reflective tape is used to enhance the surface reflection and improve the visualization quality.

1-D scan of the welded area was carried out for both the pristine and the damaged welds. The locations of the T-PWAS, damaged areas, and special recording points are illustrated in Figure 7.36.

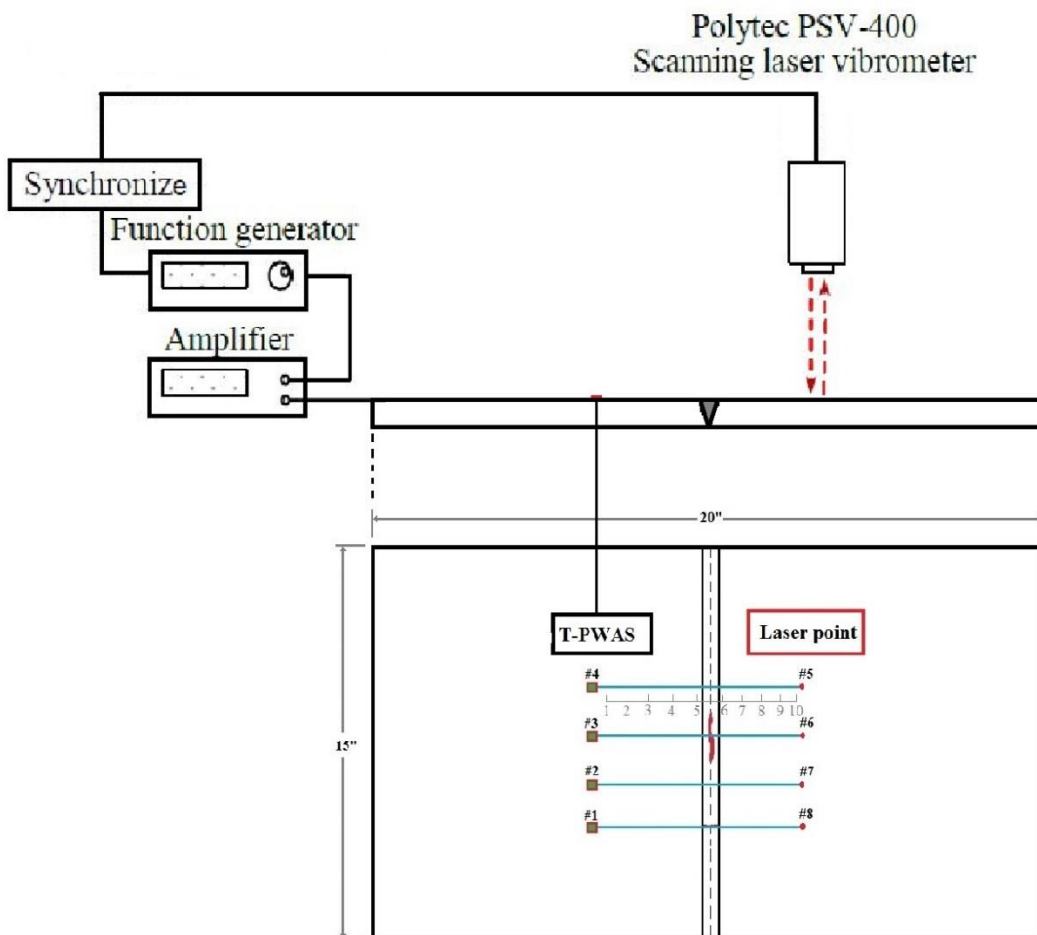


Figure 7.35 SLDV experiment set-up for wave propagation visualization

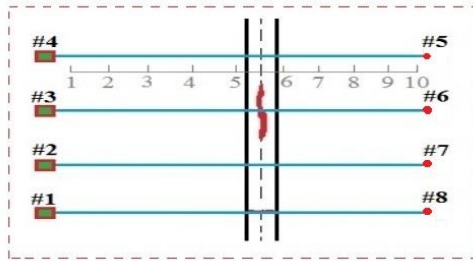


Figure 7.36 SLDV points position

7.3.2 SLDV RESULTS AND DISCUSSION

Figure 7.37 shows the waveform validation results at various sensing locations for a 90-kHz excitation for pristine welded areas. It can be observed that signals of pristine welded areas have good agreement.

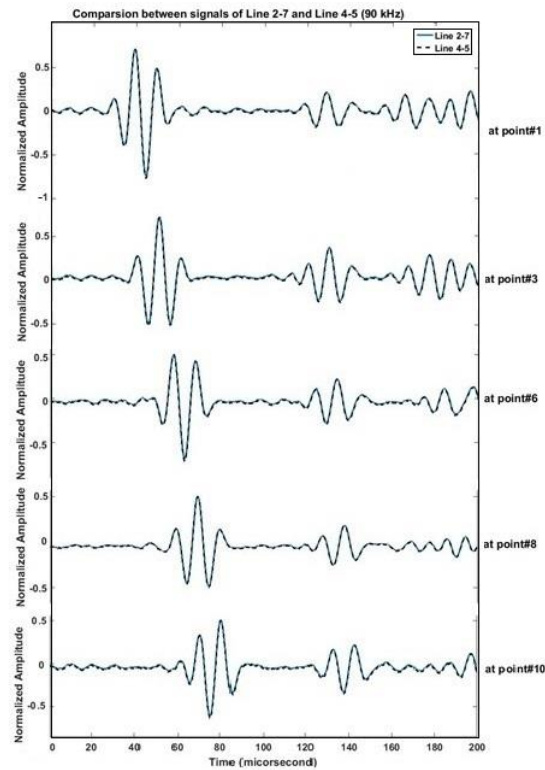


Figure 7.37 Comparison between signals of line (2-7) and (4-5) at different points

Figure 7.38 shows the comparison between pristine welded signal and area with transverse crack at different points.

At the near field (point #1, #3 and #5), S0 and A0 waves are mixed together (overlapped). The plots show small difference between the pristine welded signal and crack signal because the SLDV is ineffective to detect subsurface weld defects.

The boundary sides of reflected Lamb wave modes and packet of S0 and its reflection are determined mathematically based up on the SLDV results, will be discussed in the last part.

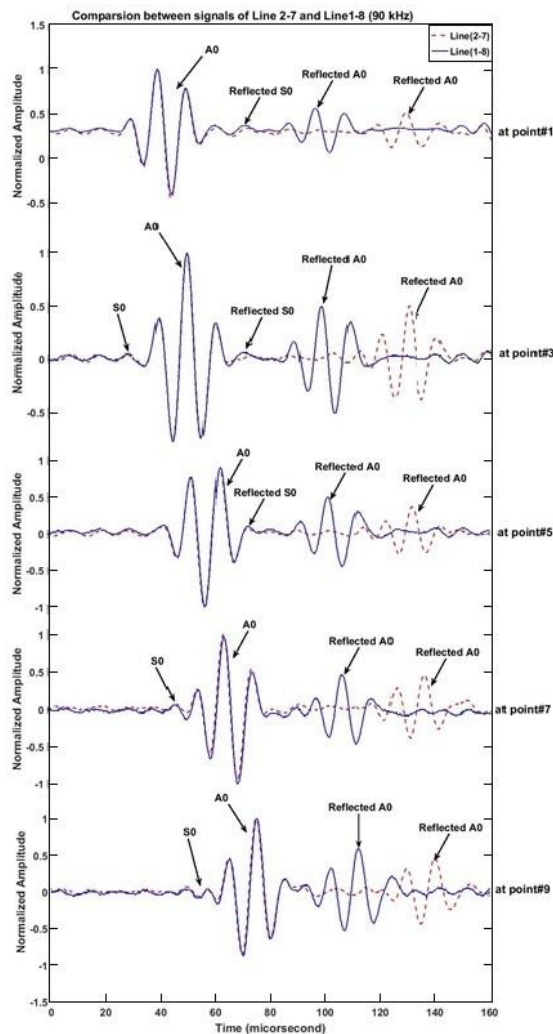


Figure 7.38 Compression between signals of line (2-7) and (1-8) at different points

Figure 7.39 shows the comparison between pristine welded signal and area with longitudinal crack at different points.

Also, at the near field (point #1, #3 and #5), S0 and A0 waves are overlapped (approved mathematically). The plots show small difference between the pristine welded signal and crack signal because the SLDV is ineffective to detect subsurface weld defects.

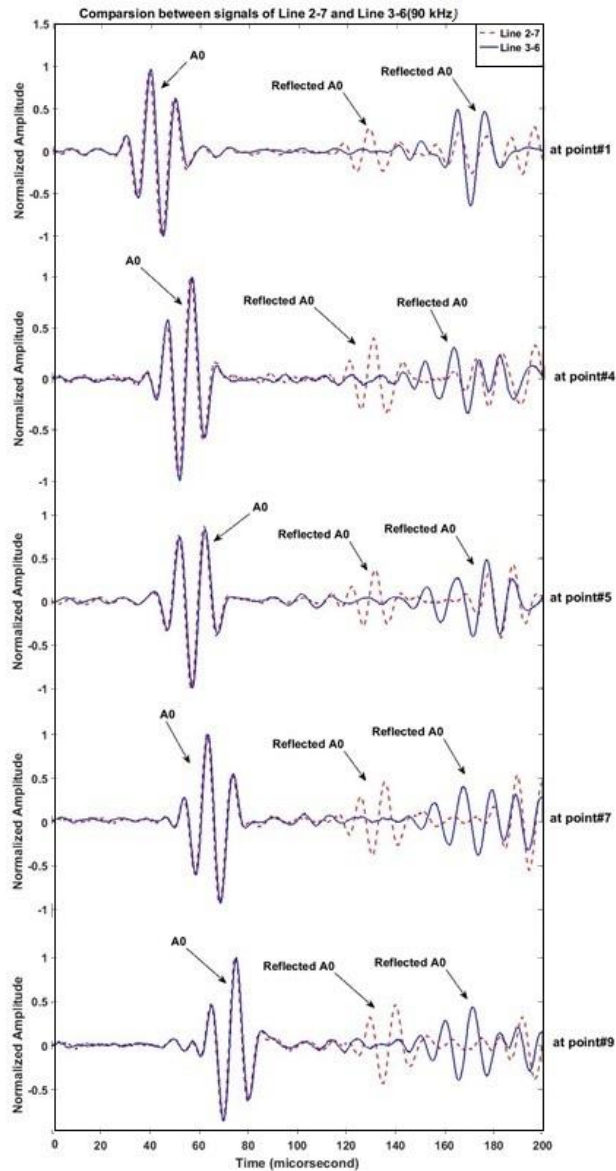


Figure 7.39 Comparison between signals of line (2-7) and (3-6) at different points

7.3.3 LOCALIZATION OF THE BOUNDARY SIDES OF REFLECTED LAMB WAVE MODES

All source localization techniques mainly depend on determination of the time of arrival (TOA) from the source signal to different points. There are many ways to measure TOA: Acoustic Emission (AE) method the most common methods. Also one way of to measure TOA is done with PWAS, excellent detail page 697 in (Giurgiutiu, 2014), and alternative methods (Elhelaly et al., 2014) The alternative method is based on of Lamb theory. As Lamb wave propagating in the plate has dispersive characteristics time deference between arrival of the fundamental modes S0 and A0 could lead to the source location. The group velocity of these two modes can be determined from dispersion curves.

The source to point distance (X_{PR}) can be calculated by this

$$X_{PR} = \Delta t (C_{gS0}C_{gA0}) / (C_{gS0} - C_{gA0}) \quad 7.7$$

Where: $\Delta t = (A_{0R} - S_{0R})$

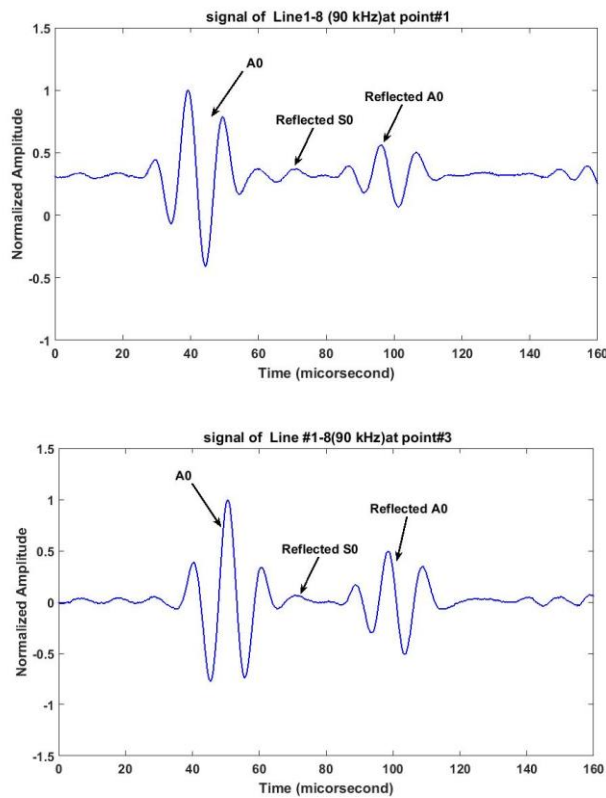
Δt is the time difference between the arrival of S0 and A0.

C_{gA0} and C_{gS0} are group velocity of S0 and A0.

To identify the boundary sides of a reflected Lamb wave modes. The propagation distance of a reflected Lamb wave mode is calculated by measuring the distance from T-PWAS and the boundary sides. Also, this distance is calculated experimentally based up on the time domain, to determine the arrival time of Lamb wave modes, and the group velocity from the dispersion curve. The small difference between of them (measured and experiment distances) will let us located the boundary side of reflection.

Now, to identify the S0 mode and reflected S0 mode packet their propagating distances must be calculated by Equation (1.7) (Elhelaly et al., 2014).

The group velocity C_g can be extracted from the measured signals by $C_g = \Delta X / \Delta t$ at any chosen frequency. Here Δt is the flight time of the wave packets propagating along the plate at two different locations on a monitor line, which can be determined by calculating the shift of the Hilbert envelope of the measured signals, and ΔX is the distance between the different locations. The accuracy of the results was enhanced by measuring at several different locations and taking averages. The small difference between of these distances will let us identify the packets as shown in Figure 7.40 Signal of Line 1-8 at different points.



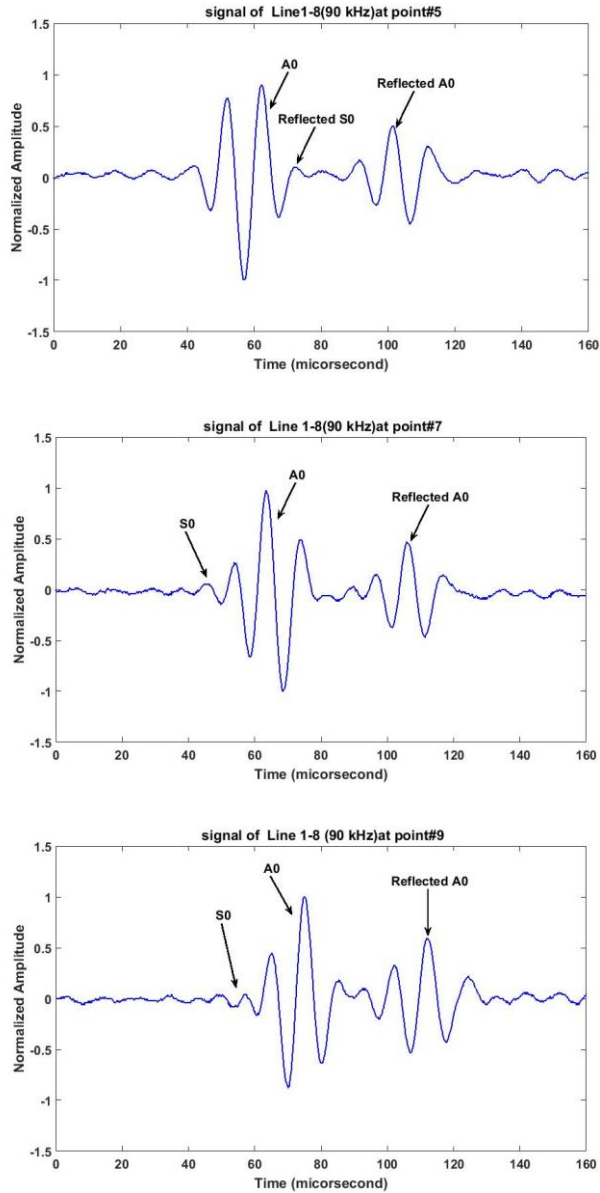


Figure 7.40 Signal of Line 1-8 at different points

7.3.4 VALIDATION OF ATTENUATION

Figure 7.41 Normalized displacement amplitude measured at different locations along line 2-7 and line3-6 and comparison with the theoretical beam-spreading wave from a point source on the plateshows the displacement amplitude measured at different locations along monitor lines 2-7 and 3-6 normalized by the displacement amplitude at 90

kHz. For comparison, the beam-spreading wave on a plane plate from a point source is also plotted in the figure, following the well-known amplitude decay of approximately $1/\sqrt{r}$ where r is the propagating distance (Fan & Lowe, 2009).

From figure 1.38, it can be seen that signal of line 3-6 (longitudinal crack), located within fill pass, has slight attenuation, which come from scattering. While there is good matching between line 2-7 (pristine welded area) and the theoretical attenuation.

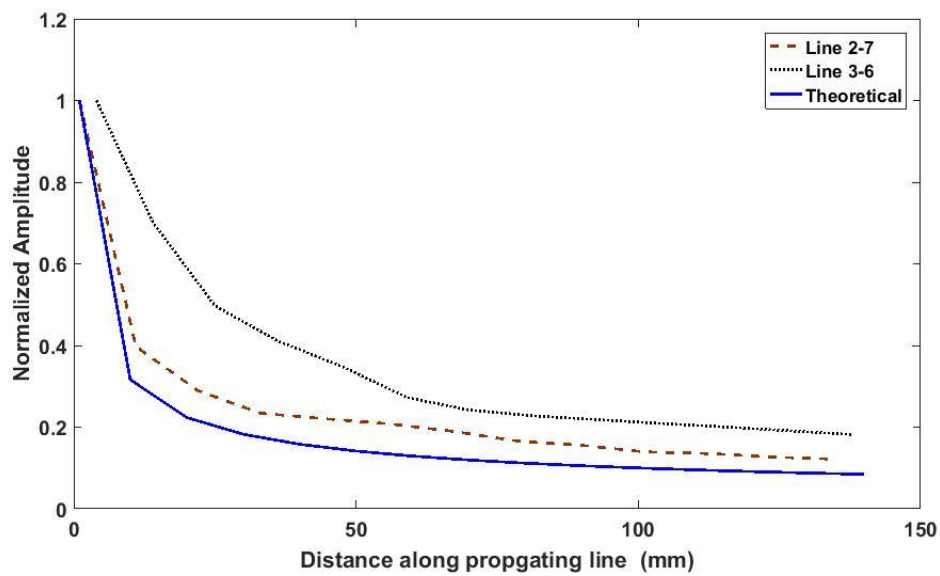


Figure 7.41 Normalized displacement amplitude measured at different locations along line 2-7 and line3-6 and comparison with the theoretical beam-spreading wave from a point source on the plate

From Figure 7.42, signal of line 1-8 (transverse crack), near to the cap pass, has high attenuation, which come from scattering. While there is good matching between line 2-7 (pristine welded area) and the theoretical attenuation.

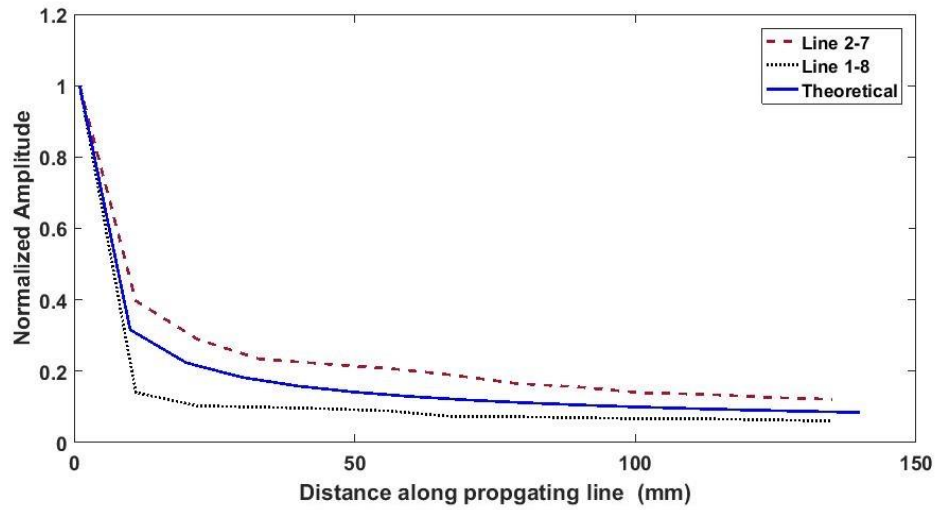


Figure 7.42 Normalized displacement amplitude measured at different locations along line 2-7 and line1-8 and comparison with the theoretical beam-spreading wave from a point source on the plate

Both figures, 1.41 and 1.42, show that SLDV is effective to detect surface or close to surface damages

CHAPTER 8

NDT AND SHM COMPARISON

8.1 THE DIFFERENCE BETWEEN STRUCTURAL HEALTH MONITORING

- ❖ Ultrasonic NDT and SHM: Ultrasonic NDT equipment too expensive and probes too expensive. Giurgiutiu and Zagrai (2000) compared cost and size of NDT and SHM transducers and found big difference. Also, today (October 2016) there are a huge difference between advanced NDT (PAUT) and SHM transducers as shown in Figure 8.1 and Figure 8.2



5L64-38.4X10-A12-P-2.5-OM

Standard Phased Array Probe, 5 MHz Linear Array, 64 Elements, 38.4x10 mm Total Active Aperture, 0.60 mm Pitch, 10 mm Elevation, A12 Case Type, Impedance Matching to Rexolite, PVC Sheathing, 2.5 m Cable Length, Omniscan Connector

[Click on Photo to Enlarge](#)

Item Number	Part Code	Frequency (MHz)	Number of Elements	Case Type	External Dimensions L (mm)	External Dimensions W (mm)	External Dimensions H (mm)	Active aperture (mm)	Pitch (mm)	Elevation (mm)	Estimated ship*	Price (USD)	Add to Cart
U8330593	5L64-38.4X10-A12-P-2.5-OM	5	64	A12	45	23	20	38.4	0.6	10	1-3 days	\$3,300.00	<input style="width: 20px; text-align: center;" type="text" value="1"/>



SA12-N55S

Standard wedge for angle beam phased-array probe A12, normal scan, 55 degree shear wave, plain wedge (without irrigation holes and carbides).

[Click on Photo to Enlarge](#)

Item Number	Part Code	Angle (°)	External Dimensions L (mm)	External Dimensions W (mm)	External Dimensions H (mm)	Sweep (°)	Estimated ship*	Price (USD)	Add to Cart
U8720550	SA12-N55S	55°	58	23/40	23	30° to 70°	1-3 days	\$190.00	<input style="width: 20px; text-align: center;" type="text" value="1"/>

Figure 8.1 PAUT probe and wedge (olympus-ims.com) Last visit 10/18/2016

While, typical PWAS weigh around 68 mg, dimensions 7×7×0.2mm and cost \$0.17 each. (steminc.com) Last visit 10/18/2016.



Figure 8.2 PWAS

❖ Rose (2014) compared NDT and SHM and found:

NDT	SHM
Offline evaluation	Online evaluation
Time-based maintenance	Condition-based maintenance
Find existing damage	Determine fitness for service and remaining useful time damage
More cost and labor	Less cost and labor
Baseline not available	Baseline required
	Environmental data compensation methods required

Figure 8.3 shows the NDT for a plane that done offline. Although NDT is cost more than SHM, it has more resolution than SHM.



Figure 8.3 NDT-RT for a plane. Adopted from NDT handbook, 3rd ed.: v 4, RT

❖ The frequency range:

In UT-NDT starts from 0.1MHz to 1GHz. While in SHM start from 10Hz and goes up to 1MHz, Figures 4.1 and 4.2. Since low frequency produce high penetration for the ultrasonic wave into a structure, low attenuation, high sensitivity to detect a defect within high thickness structure. Thus, the detectability of guided waves in SHM higher than in NDT.

❖ Personnel training

❖ Interpretation of NDT results is somewhat subjective while SHM results interpretation is objective. Because of the skill required in manual testing and the dependence on the operator's care and integrity, many users of ultrasonic weld

inspection require their operators to have certificates of competence in each specific application(Halmshaw, 1996).

❖ NDT and SHM Transducers

Giurgiutiu and Cuc (2005) stated that PWAS may seem very similar to the conventional ultrasonic transducers since both use the piezoelectric effect. However, fundamental differences exist between the conventional ultrasonic transducers and the PWAS.

1. Conventional ultrasonic transducers are weakly coupled with the structure through gel, water, or air. In contrast, PWAS are strongly coupled with the structure through an adhesive bond.
2. Conventional ultrasonic transducers are resonant narrow-band devices. In contrast, PWAS are non-resonant broad-band devices that can be tuned selectively into certain Lamb modes.
3. Conventional ultrasonic transducers excite and sense the Lamb waves in the structure indirectly through acoustic waves impinging on the structural surface and the mode conversion. In contrast, PWAS excite and sense the Lamb waves in the structure directly through in-plane

In general, it is important to apply both NDT and SHM methods to have excellent monitoring of a structure health status.

CHAPTER 9

CONCLUSION AND FUTURE WORKS

The chapter presents summary and conclusions to the overall thesis manuscript by addressing the development and contribution of conducting the research, discussing each research topic of the thesis.

9.1 SUMMARY

The thesis started with an introduction austenitic stainless steel, metallurgy and microstructure characteristics, properties and application. Then, the NDT and SHM methods are introduced to choose good method for inspection of austenitic stainless steel. The fundamental of ultrasonic testing in NDT is discussed. Guided waves, SHM concepts, and piezoelectric wafer active sensors (PWAS) is introduced.

The experimental part produces the fabrication of artificial realistic defects in austenitic stainless steel weld, NDT methods (RT and PAUT) are applied to the specimens. SHM methods (pitch-catch and SLDV) are conducted to detect the realistic defects. The NDT and SHM methods are compared and discussed.

9.2 CONCLUSION

Austenitic stainless steels, especially the welding process zone, exhibit heterogeneous and anisotropic behavior which has a decisive influence on the ultrasonic beam making

the interpretation of ultrasonic inspection results notoriously difficult. The damage detection within this structure is done with NDT and SHM methods. Thus, the conclusions of this work are:

1. Realistic defects are produced to investigate the ultrasonic behavior in anisotropic structure
2. NDT results verify the procedure of fabrication of realistic defects
3. Advanced ultrasonic phased array (PAUT) accurately detect the undersurface weld defects
4. SHM methods provide more details about the guided waves in the structure
5. Pitch-Catch technique shows the efficiency of the Lamb wave guided wave to detect the discontinuities under the surface of structure
6. SLDV visualizes the wave propagation through the austenitic stainless steel welded
7. SLDV is limited to detect very small damages under the plate surface
8. In general NDT and SHM comparison, there is no methods better than other to validate a structure health. In order to get optimum monitoring and test for a structure status, it is important to implement both methods, NDT and SHM.

9.3 RECOMMENDATION FOR FUTURE WORK

This thesis has presented various methods for damage detection, cracks in welding, using NDT and SHM methods. This work has laid the foundation for future investigations to extend the methodologies to more complicated structures. The suggestions for future work are listed below:

1. Austenitic stainless steel plate of (0.5" or thicker) thick to study the guided wave behavior.
2. Use another welding technique.
3. Fabricate the plate with other types of welding defects.
4. Study the effect of high temperature on the welded plate microstructure, PWAS, and the guided waves.
5. Apply FEA based on the grain boundaries of base metal, HAZ, and welding zone to get more accurate results for the wave propagating in the welded plate.
6. Apply combined analytical finite analysis (CAFA)
7. Using another advanced NDT method
8. SHM techniques such as pulse-echo

Applying these suggestions advance ultrasonic method for anisotropic structures.

REFERENCES

- Atomic, I., & Agency, E. (2001). Guidebook for the Fabrication of Non-Destructive Testing (NDT) Test Specimens. *Direct*, (13), 12–14.
- Chassignole, B., El Guerjouma, R., Ploix, M. A., & Fouquet, T. (2010). Ultrasonic and structural characterization of anisotropic austenitic stainless steel welds: Towards a higher reliability in ultrasonic non-destructive testing. *NDT and E International*, 43(4), 273–282. <http://doi.org/10.1016/j.ndteint.2009.12.005>
- Cheeke, J. (2012). *Fundamentals and applications of ultrasonic waves*. CRC Press LLC.
- Connolly, G. D. (2009). MODELLING OF THE PROPAGATION OF ULTRASOUND THROUGH AUSTENITIC STEEL by, (August).
- Consonni, M., Wee, C. F., & Schneider, C. (2012). Manufacturing of welded joints with realistic defects. *Insight: Non-Destructive Testing and Condition Monitoring*, 54(2), 1–9. <http://doi.org/10.1784/insi.2012.54.2.76>
- Crutzen, S., Lemaitre, P., & Bièth, M. (1998). General lessons learnt from round robin tests and qualifications tests relating to non-destructive examination. *International Journal of Pressure Vessels and Piping*, 75(5), 417–427. [http://doi.org/10.1016/S0308-0161\(97\)00086-0](http://doi.org/10.1016/S0308-0161(97)00086-0)
- Dhayalan, R., Kumar, A., Purnachandra Rao, B., & Jayakumar, T. (2016). Ultrasonic high-frequency guided waves for the inspection of shell weld in core support structure of fast breeder reactors. *Structural Health Monitoring*, 15(3), 266–278. <http://doi.org/10.1177/14759217166641904>
- Elhelaly, A., Hassan, M., & Mohany, A. (2014). LOCALIZATION OF ACOUSTIC EMISSION SOURCE IN PLATES USING WAVELET Theoretical background Experimental set-up Results and desiccations References. *Acoustics Week in Canada 2014*, 2–3. Retrieved from <http://awc.caa-aca.ca/index.php/AWC/AWC14/paper/view/72>
- ENIQ, I. for E. (Ed.). (2011). *ENIQ TQG TECHNICAL DOCUMENT PRACTICAL EXAMPLES FOR MANUFACTURING OF* (ENIQ repor). Luxembourg: Publications Office of the European Union. Retrieved from <http://www.jrc.ec.europa.eu/>
- Every, A. G. (2014). The importance of ultrasonics in nondestructive testing and evaluation. *Ultrasonics*, 54(7), 1717–1718. <http://doi.org/10.1016/j.ultras.2014.06.009>
- Fan, Z., & Lowe, M. J. S. (2009). Elastic waves guided by a welded joint in a plate. *Proceedings of the Royal Society A: Mathematical, Physical and Engineering Sciences*, 465(2107), 2053–2068. <http://doi.org/10.1098/rspa.2009.0010>
- Fan, Z., & Lowe, M. J. S. (2012). NDT & E International Interaction of weld-guided waves with defects. *NDT and E International*, 47, 124–133. <http://doi.org/10.1016/j.ndteint.2012.01.001>

- Folkhard, E., Rabensteiner, G., Perteneder, E., Schabereiter, H., & Tösch, J. (1988). *Welding Metallurgy of Stainless Steels*. 1988 by Springer-Verlag/Wi.
- Giurgiutiu, V. (2002). Lamb wave generation with piezoelectric wafer active sensors for structural health monitoring. *Proceedings of the SPIE's 10th Annual International Symposium on Smart Structures and Materials and 8th Annual International Symposium on NDE for Health Monitoring and Diagnostics*, 5056(March), 1–6. <http://doi.org/10.1117/12.483492>
- Giurgiutiu, V. (2014). *Structural Health Monitoring With Piezoelectric Wafer Active Sensors*. Elsevier Inc. (SECOND EDI). Elsevier Inc.
- Giurgiutiu, V. & A. C. (2005). Embedded Non-destructive Evaluation for Structural Health Monitoring, Damage Detection, and Failure Prevention. *The Shock and Vibration Digest*, 37(2), 83–105. <http://doi.org/10.1177/0583102405052561>
- Giurgiutiu, V., Bao, J., & Zhao, W. (2003). Piezoelectric Wafer Active Sensor Embedded Ultrasonics in Beams and Plates. *Experimental Mechanics*, 43(4), 428–449. <http://doi.org/10.1177/0014485103434008>
- Halmshaw, R. (1996). Introduction to the non-destructive testing of welded joints. *NDT & E International*, 24(4), 217. [http://doi.org/10.1016/0963-8695\(91\)90308-P](http://doi.org/10.1016/0963-8695(91)90308-P)
- Hamstad, M. (2001). An illustrated overview of the use and value of a wavelet transformation to acoustic emission technology. *NIST, Boulder, Report*, 6–8. Retrieved from <http://scholar.google.com/scholar?hl=en&btnG=Search&q=intitle:An+illustrated+overview+of+the+use+and+value+of+the+wavelet+transformation+to+acoustic+emission+technology#0>
- Handbook on the Ultrasonic Examination Austenitic Welds Handbook On the Ultrasonic Examination of Austenitic Welds. (1986).
- Harker, A. H., Ogilvy, J. A., & Temple, J. A. G. (1990). Modeling ultrasonic inspection of austenitic welds. *Journal of Nondestructive Evaluation*, 9(2–3), 155–165. <http://doi.org/10.1007/BF00566391>
- Harold M.Cobb. (1999). Steel Products Manual Stainless Steels.
- Hellier, C. J. (2003). *Introduction to nondestructive testing*. *Handbook of Nondestructive Evaluation*. [http://doi.org/10.1016/0308-9126\(88\)90483-X](http://doi.org/10.1016/0308-9126(88)90483-X)
- Hertlein, B., & Davis, A. (2006). *Nondestructive Testing of Deep Foundations*. *Nondestructive Testing of Deep Foundations*. <http://doi.org/10.1002/0470034831>
- Holmberg, B. (2008). Stainless steels – their properties and their suitability for welding. Retrieved from https://scholar.google.com/scholar?hl=en&q=Stainless+steels+-+their+properties+and+their+suitability+for+welding&btnG=&as_sdt=1,41&as_sdt_p=
- Hudgell, R. (1994). Handbook on the ultrasonic examination of austenitic clad steel components, 62. Retrieved from <http://scholar.google.com/scholar?hl=en&btnG=Search&q=intitle:Handbook+on+the+ultrasonic+examination+of+austenitic+clad+steel+components#0>
- Hudgell, R. J., & Gray, B. S. (1985). The ultrasonic inspection of austenitic materials State of the art report, 1201(94), 31. Retrieved from <http://scholar.google.com/scholar?hl=en&btnG=Search&q=intitle:The+ultrasonic+inspection+of+austenitic+materials+State+of+the+art+report#0>
- International Atomic Energy Agency. (2001). Guidebook for the Fabrication of Non-

- Destructive Testing (NDT) Test Specimens. *Iaea-TecdDoc-Tcs-13*, (13).
- Kamas, T., Giurgiutiu, V., & Lin, B. (2015). Quasi-Rayleigh Waves in Butt-Welded Thick Steel Plate. *41st Annual Review Of Progress In Quantitative Nondestructive Evaluation, Vol 34, 1650*, 686–694. <http://doi.org/10.1063/1.4914669>
- Kemppainen, M., & Virkkunen, I. (2011). Crack characteristics and their importance to NDE. *Journal of Nondestructive Evaluation*, 30(3), 143–157. <http://doi.org/10.1007/s10921-011-0102-z>
- Khatak, H. S., & Raj, B. (2002). *Corrosion of Austenitic Stainless Steels*. <http://doi.org/10.1533/9780857094018>
- Ki, J., & Lai, L. (2012). Stainless Steels: An Introduction and Their Recent Developments Edited By, 3–7.
- Kijanka, P., Manohar, a., Lanza di Scalea, F., & Staszewski, W. J. (2015). Damage location by ultrasonic Lamb waves and piezoelectric rosettes. *Journal of Intelligent Material Systems and Structures*, 26(12), 1477–1490. <http://doi.org/10.1177/1045389X14544140>
- Kumar, K., Madhusoodanan, K., & Rupani, B. B. (2006). Miniature specimen technique as an NDT tool for estimation of service life of operating pressure equipment. *Int Conf on Pressure Vessel and Piping, OPE-2006-CHENNAI*, (285), 92–102.
- Lempriere, B. (2002). *Ultrasonic and Elastic Waves: Frequently Asked Questions*.
- Lippold, J., & Kotecki, D. (2005). Welding Metallurgy and Weldability of Stainless Steels. ... *Metallurgy and Weldability of Stainless* <http://doi.org/10.1002/9781118960332>
- Malpally, D. R. (2014). Uncertainty Analysis of Mechanical Properties From Miniature Tensile Testing of High Strength Steels, 32–40. Retrieved from <http://digitalcommons.usu.edu/cgi/viewcontent.cgi?article=5040&context=etd>
- Moysan, J., Apfel, A., Corneloup, G., & Chassignole, B. (2003). Modelling the grain orientation of austenitic stainless steel multipass welds to improve ultrasonic assessment of structural integrity. *International Journal of Pressure Vessels and Piping*, 80(2), 77–85. [http://doi.org/10.1016/S0308-0161\(03\)00024-3](http://doi.org/10.1016/S0308-0161(03)00024-3)
- Moysan, J., & Ploix, M. (2009). Advances in ultrasonic testing of austenitic stainless steel welds. Towards a 3D description of the material including attenuation and optimisation by inversion. *Ultrasonic Wave*, 128, 15–24. Retrieved from http://apps.isiknowledge.com/full_record.do?product=WOS&search_mode=CombineSearches&qid=11&SID=X2mjd7mFac722iOeccA&page=1&doc=1\http://www.springerlink.com/index/N362217R132822P8.pdf
- Nath, S. K., Balasubramaniam, K., Krishnamurthy, C. V., & Narayana, B. H. (2009). Detection and Sizing of Defects in Complex Geometry Weld by Manual Ultrasonic Time of Flight Diffraction Inspection. *Journal of Pressure Vessel Technology*, 131(5), 51501. <http://doi.org/10.1115/1.3141436>
- Ngon, D. T., & Toan, P. Van. (2015). Research and proposal on welding technique for longitudinal crack defect welding, 3, 29–34. <http://doi.org/10.11648/j.ijmea.s.2015030103.15>
- Palanichamy, P., Joseph, a, Jayakumar, T., & Raj, B. (1995). Ultrasonic velocity measurements for estimation of grain size in austenitic stainless steel. *NDT E International*, 28(3), 179–185. [http://doi.org/10.1016/0963-8695\(95\)00011-L](http://doi.org/10.1016/0963-8695(95)00011-L)
- PODDAR, B., & GIURGIUTIU, V. (2015). Detection and Characterization of Cracks

- Using Lamb Wave Propagation. *Structural Health Monitoring* 2015. <http://doi.org/10.12783/SHM2015/75>
- Praveen, A., Vijayarekha, K., Abraham, S. T., & Venkatraman, B. (2013). Signal quality enhancement using higher order wavelets for ultrasonic TOFD signals from austenitic stainless steel welds. *Ultrasonics*, 53(7), 1288–1292. <http://doi.org/10.1016/j.ultras.2013.03.013>
- Pudovikov, S. (2008). Ultrasonic inspectability of austenitic stainless steel and dissimilar metal weld joints, 34. *MPA-Seminar Werkstoff- ...*, 1–13. Retrieved from http://ideal-technologies.com/files/pdf/03_Ultrasonic_inspectability_of_austenitic_stainless_steel_and_dissimilar_metal_weld_joints.pdf
- Qin, J., Feng, J., Li, Y., Mo, K., & Lu, S. (2011). *Ultrasonic-assisted liquid-liquid extraction and HILIC-ELSD analysis of ginsenoside Rb1, astragaloside IV and dulcitol in sugar-free “Fufangfufangteng Heji.” Journal of Pharmaceutical and Biomedical Analysis* (Vol. 56). <http://doi.org/10.1016/j.jpba.2011.07.033>
- Rabenberg, E. M. (2012). Small Specimen Test Techniques for Evaluating Radiation-Induced Changes in Mechanical Properties., (December), 1–68.
- ROBERTW. MESSLER, J. (1999). *Principles of Welding. Reservoir Engineering Handbook*. <http://doi.org/10.1002/9783527617487>
- Rodríguez, C., García Cabezas, J., Cárdenas, E., Belzunce, F. J., & Betegón, C. (2009). Mechanical properties characterization of heat-affected zone using the small punch test. *Welding Journal (Miami, Fla)*, 88(9), 188s–192s. Retrieved from <http://www.scopus.com/inward/record.url?eid=2-s2.0-70349446383&partnerID=40&md5=61c83bc5932eddaaa242faa6b225a2d4>
- Rose, J. L. (2014). *Ultrasonic Waves in Solid Media*. <http://doi.org/10.1017/CBO9781107273610>
- Shen, Y. (2014). Structural Health Monitoring Using Linear and Nonlinear Ultrasonic Guided Waves.
- Srivastava, S. P., Karn, K. N., Sahu, G. P., Pandarkar, S. P., & Jawale, S. B. (n.d.). Fabrication of Defect Samples for NDT Certification Courses.
- Srivastava, S. P., Karn, K. N., Sahu, G. P., Pandarkar, S. P., & Jawale, S. B. (2013). Fabrication of Defect Samples for NDT Certification Courses.
- STRUCTURAL HEALTH MONITORING WITH PIEZOELECTRIC WAFER ACTIVE SENSOR (2 by Victor Giurgiutiu PhD Professor of Mechanical Engineering, University of South Carolina. (n.d.), 1–9.
- Tseng, K. H., & Hsu, C. Y. (2011). Performance of activated TIG process in austenitic stainless steel welds. *Journal of Materials Processing Technology*, 211(3), 503–512. <http://doi.org/10.1016/j.jmatprotec.2010.11.003>
- Virkkunen, I., Kempainen, M., Ostermeyer, H., Paussu, R., & Dunhill, T. (2009). Grown cracks for NDT development and qualification. *Insight: Non-Destructive Testing and Condition Monitoring*, 51(5), 271–275. <http://doi.org/10.1784/insi.2009.51.5.271>
- Yan, J., Gao, M., & Zeng, X. (2010). Study on microstructure and mechanical properties of 304 stainless steel joints by TIG, laser and laser-TIG hybrid welding. *Optics and Lasers in Engineering*, 48(4), 512–517. <http://doi.org/10.1016/j.optlaseng.2009.08.009>
- Yu, L., Bottai-Santoni, G., & Giurgiutiu, V. (2010). Shear lag solution for tuning

ultrasonic piezoelectric wafer active sensors with applications to Lamb wave array imaging. *International Journal of Engineering Science*, 48(10), 848–861. <http://doi.org/10.1016/j.ijengsci.2010.05.007>

Yu, L., & Giurgiutiu, V. (n.d.). Damage Detection Using Guided Waves and Piezoelectric Wafer Active Sensor Arrays.

Yu, L., & Giurgiutiu, V. (2007). In-situ optimized PWAS phased arrays for Lamb wave structural health monitoring. *Journal of Mechanics of Materials and Structures*, 2(3), 459–487. <http://doi.org/10.2140/jomms.2007.2.459>

Yu, L., & Giurgiutiu, V. (2008). In situ 2-D piezoelectric wafer active sensors arrays for guided wave damage detection. *Ultrasonics*, 48(2), 117–134. <http://doi.org/10.1016/j.ultras.2007.10.008>

Zagrai, A. N. (2002). Piezoelectric Wafer Active Sensor Electro-Mechanical Impedance Structural Health Monitoring, 40–52. Retrieved from <http://onlinelibrary.wiley.com/doi/10.1002/cbdv.200490137/abstract>